

2015

Using speckle statistics to improve attenuation estimates for cervical assessment

Viksit Kumar
Iowa State University

Follow this and additional works at: <https://lib.dr.iastate.edu/etd>

 Part of the [Biomedical Commons](#)

Recommended Citation

Kumar, Viksit, "Using speckle statistics to improve attenuation estimates for cervical assessment" (2015). *Graduate Theses and Dissertations*. 14362.
<https://lib.dr.iastate.edu/etd/14362>

This Dissertation is brought to you for free and open access by the Iowa State University Capstones, Theses and Dissertations at Iowa State University Digital Repository. It has been accepted for inclusion in Graduate Theses and Dissertations by an authorized administrator of Iowa State University Digital Repository. For more information, please contact digirep@iastate.edu.

Using speckle statistics to improve attenuation estimates for cervical assessment

by

Viksit Kumar

A dissertation submitted to the graduate faculty
in partial fulfillment of the requirements for the degree of

DOCTOR OF PHILOSOPHY

Major: Mechanical Engineering

Program of Study Committee:
Timothy Bigelow, Major Professor
Eliot Winer
Meng Lu
Aleksandar Dogandzic
Ronald Roberts

Iowa State University

Ames, Iowa

2015

Copyright © Viksit Kumar, 2015. All rights reserved.

DEDICATION

I would like to dedicate this work to my parents Anoop and Alka Nigam for their constant love, advice and encouragement. I would also like to specially thank my brother Amit Nigam for being my support system and helping me with every aspect of this work.

TABLE OF CONTENTS

	Page
NOMENCLATURE	v
ACKNOWLEDGMENTS	vi
ABSTRACT	vii
CHAPTER 1 INTRODUCTION	1
CHAPTER 2 ALGORITHM COMPARISON BY VARYING REGION OF INTEREST SIZE	6
Introduction	6
Materials and Methods.....	8
Results.....	15
Discussion.....	23
CHAPTER 3 GAMMA MIXTURE MODEL: PHANTOM AND SIMULATION	26
Introduction	26
Gamma mixture model and EM algorithm	29
Implementation of Gamma mixture model.....	31
Simulation	35
Three layered phantoms.....	38
Conclusion	43
CHAPTER 4 APPLICATION OF GAMMA MIXTURE MODEL ON CERVICAL DATA.....	45
Introduction	45
Materials and method.....	49
Results.....	53
Conclusion.....	59
CHAPTER 5 SUMMARY AND CONCLUSIONS	60
Conclusion	60
REFERENCES	62
APPENDIX A SUPPLEMENTARY PLOTS FOR CHAPTER 2	68

APPENDIX B	SUPPLEMENTARY PLOTS FOR CHAPTER 4	106
APPENDIX C	COMPARISON ON PER PATIENT BASIS	119

NOMENCLATURE

ROI	Region of Interest
RF	Radio frequency
IQ	In-phase quadrature
QUS	Quantitative ultrasound
GMM	Gamma mixture model
EM	Expectation Maximization
ROC	Receiver operating characteristic

ACKNOWLEDGMENTS

I would like to thank my committee chair, Dr. Timothy Bigelow for his continuance guidance, patience and support throughout the course of this research. This work would not have been possible without his mentoring and enthusiasm for research.

I would also like to thank my committee members for their direction and valuable advice for the project. Also our collaborator Dr. Barbara McFarlin for collecting the Human cervix data and providing assistance with the biological aspects of the study.

In addition, I would also like to thank my friends for understanding and being there for me. I would also like to thank Sophiya Das for spending innumerable hours proof reading the thesis work.

ABSTRACT

Preterm birth is a major contributor to infant mortality worldwide. Cervical length and previous history of preterm birth are the only two indicators which can help in identifying preterm birth but have a low positive identifying rate. Quantitative ultrasound parameters like attenuation can provide additional details about the tissue microstructure besides the diagnostic image. Attenuation can be used to detect preterm cases as the attenuation decreases with the increasing gestation age and this decrease can be seen earlier in cases of preterm birth. The algorithm and the size of the region of interest (ROI) play a vital role in calculating valid estimates of attenuation. In this paper, we compared the ability of the Spectral log difference algorithm and the Spectral difference algorithm to detect changes in the cervix leading to delivery for both full term and preterm births under varying ROI sizes. Spectral log difference yields a more consistent decrease in the attenuation as we approach delivery for both the preterm and full term patients. ROI size doesn't significantly alter the observed trends for this study. For preterm birth a maximum decreases of 0.35dB/cm-MHz was observed. The bias in attenuation algorithms can be removed by selecting homogenous regions inside the cervix, but the cervix is a heterogeneous tissue. Gamma mixture model is used to segment the cervix into different tissue types and attenuation algorithm are then applied to individual tissue type to get an estimate of attenuation. The area under the receiver operating characteristic curve increases from 56% to 80% when gamma mixture model is used for segmentation.

CHAPTER 1

INTRODUCTION

Ultrasonic imaging has been used for decades to anatomically visualize the soft tissue. Diagnostic ultrasound is an integral part of medical hospital and is used in plethora of clinical applications. The longitudinal waves emitted from an ultrasound transducer can be used to detect the changes in the mechanical properties of the tissue. Diagnostic ultrasound is considered one of the safest imaging modality specially in contrast to imagining modality with ionizing radiation like X-ray and magnetic resonance imaging. Since diagnostic ultrasound machines are portable and affordable compared to other imaging modalities, they have found their way into all aspects of human and animal healthcare.

Ultrasonic diagnostic scans provide a good anatomical visualization of the soft tissue. A conventional ultrasonic transducer would either operate in pulse echo mode or continuous mode for Doppler applications. The transducer is excited with a nominal center frequency ranging from 1 to 20 MHz depending on the type of tissue being imaged. A B-mode image is then obtained from the envelope of the radio frequency (RF) signal and displayed for the clinician's to infer. However, the B-mode images do not provide any quantitative information about the tissue microstructure. The frequency dependent information of the back scattered RF data can also be used to give additional information about the underlying tissue. As the ultrasound wave travels into the medium and is reflected by different tissue types having different scattering properties, the back scattered wave is dependent on the properties of the scatterer it was reflected from. An interest to obtain quantitative information about the tissue microstructure has persisted in the scientific community for the last few decades. These tissue structures are usually in the order or

smaller than the wavelength (based on the center frequency) of the transducer. The RF data gathered from these ultrasound scans can be used to calculate quantitative ultrasound parameters (QUS) like backscatter, scatter size, and acoustic concentration [1-5]. Backscatter is the reflected echo obtained by the transducer after a pulse has been released into the medium being imaged. Scatter size and acoustic concentration refer to the acoustic scatterer's present in the tissue medium. Since these QUS properties are intrinsic to the tissue being imaged they can provide lot of information about the tissue microstructure. The property of these scatterer's are discussed in more detail in chapter 3.

Ultrasonic attenuation is another QUS parameter which is defined as the loss of energy when ultrasound wave propagates in the medium. This loss can be due to both absorption of the wave in to the medium and scattering of the wave in the medium. The viscosity of the medium is the determining factor behind the amount of energy absorbed by the medium. More viscous mediums have higher absorption, hence higher attenuation. The softer the tissue the lower is the attenuation value. A compilation of attenuation coefficients for different human tissues is given by Dunn [6]. The human cervix is a good example of a tissue whose softness changes as the cervix prepares for delivery. The cervix softens drastically from first trimester to second trimester as measure by Badir et al[7]. But between the second and third trimester the cervix softens but not as much. The first trimester does not play an important role in determining the time of delivery. Studies have shown that as the delivery time approaches, the collagen rich cervix is filled with water and enzymes which results in a lower attenuation value and a softening of the cervix. Our earlier work showed that attenuation of the cervix decreased as the cervix prepared for delivery [8-12]. The softening of the cervix can also be quantified using shear wave elastography [13-15]. In this method a stress is created and then the strain in the tissue is

observed from that stress. Static shear wave elastography uses an external source for introducing stress into the tissue medium, like tapping the body. This method can have user bias and the results are often irreproducible. Dynamic shear wave elastography overcomes this problem by introducing a shear wave which itself causes stress inside the tissue and this can be repeated over and over giving the same results. The stress and strain are used to give a stiffness map of the cervix. One of the purposes of identifying the softness of the cervix is to determine if the birth is a case of preterm birth. Preterm birth is defined as the birth of a baby before 37 completed weeks of pregnancy. Preterm birth is the leading cause of infant mortality worldwide [16] and the second main contributor in the United States [17]. According to Center for Disease Control and Prevention, 35% of infant deaths in the United States were related to preterm birth in 2010. Out of 13 million preterm births globally, more than 1 million babies die annually contributing to 27% of neonatal deaths [18]. Preterm birth can be further classified into two sub categories: spontaneous and medically induced. In either case, the cervix undergoes a process of remodeling in which the collagen rich cervix loses its collagen concentration as more space is created between the fibrils. This space is filled by water and enzymes which causes the collagen fibrils to change their alignment becoming more disorganized leading to softening of cervix as it prepares for delivery [19]. Presently cervical length is used as a parameter to identify women at risk for preterm birth, but it has a low positive predictive value as many women with a short cervix will still deliver full-term [20, 21]. Hence there is a need to develop additional techniques to detect preterm birth.

The research work in this thesis has been divided into three main parts. In the first part we conduct a longitudinal study in which pregnant human patients are used. Ultrasonic attenuation estimates are obtained at 5 different time points between the second and third

trimester. Two different algorithms (viz. spectral difference and spectral log difference) are compared by varying their region of interest (ROI) size. The purpose of this part is to understand how the different ROI sizes effect attenuation and determining the optimal ROI size for both the algorithms. The results of this part show that the ROI does not play a big role in attenuation values due to the heterogeneity of the cervix. Since the cervix is heterogeneous the attenuation values have high variance as the attenuation algorithms assume that the tissue medium is homogenous. From this study it is also observed that preterm birth and full term birth attenuation value do decrease as they approach the time to delivery.

The second part of the thesis tries to understand the reason behind the heterogeneity of the cervix and the importance of selecting regions with homogenous tissue. Different models for estimating the speckle pattern are presented and finally gamma mixture model is selected. Gamma mixture model does not provide physical information about the tissue but gives empirical the best fit for real ultrasound data. We use computer simulations to understand the dependence of gamma parameters on the different scattering properties like scattering size and scattering number density. In addition B-mode images are simulated having regions of varying scattering properties, then gamma mixture model is used to differentiate these different regions. The success of simulations encourages us to try phantom experiments. Two custom manufactured 3 layered phantoms are used, having regions of varying scattering. Gamma mixture model is then used to identify the different regions. Attenuation maps are also generated for both simulations and phantoms. The attenuation estimates at the boundary of different scatterer's are invalid. Since gamma mixture model can identify these boundary the attenuation estimates which are invalid can be rejected.

The third part of thesis applies the above developed gamma mixture model for human patient data. The data from study in chapter 2 is reprocessed. Different techniques are considered for using the gamma mixture model. A multi parameter approach is suggested in which the gamma parameters are used as a restrictive criteria for selecting valid attenuation estimates. This is important as the gamma parameters correspond to the speckle pattern. Points which vary too much from the ideal values of the gamma parameter might be due to edge effects or speckle pattern. The use of gamma mixture model is not only restricted for ultrasonic attenuation but can be used in plethora of applications as it can differentiate between regions of different back scatter. The traditional approach of calculating back scatter coefficient does not work in this case as it requires the attenuation of the medium to be known. Using an approximate value of attenuation biases the estimation of back scatter coefficient. Thus affecting the ability to use these back scatter coefficients for differentiating different tissue types.

CHAPTER 2

ALGORITHM COMPARISON BY VARYING REGION OF INTEREST SIZE

2.1 Introduction

Preterm birth is the birth of baby before 37 completed weeks of pregnancy. Preterm birth is the leading cause of infant mortality worldwide [16] and the second main contributor in the United States [17]. 35% of infant deaths in the United States in 2010 were related to preterm birth according to Center for Disease control and Prevention. Meanwhile, globally 13 million preterm babies are born each year with more than 1 million dying annually contributing to 27% of neonatal deaths [18]. While preterm birth cases may be reduced by providing better education to both the provider and patient [22], better assessments for the risk of preterm birth are still needed. In preparation for delivery, the cervix undergoes a process of remodeling in which the collagen rich cervix loses its collagen concentration as more space is created between the fibrils. This space is filled by water and enzymes which causes the collagen fibrils to change their alignment becoming more disorganized and softening the cervix as it prepares for delivery [19]. Presently cervical length is used as a parameter to identify women at risk for preterm birth, but it has a low positive predictive value as many women with a short cervix will still deliver full-term [20, 21]. Hence there is a need to develop additional techniques to detect preterm birth.

Ultrasonic diagnostic scans give a good anatomical visualization of the soft tissue but give no quantitative information about the tissue microstructure. The radio frequency (RF) data gathered from these ultrasound scans can be used to calculate quantitative ultrasound parameters (QUS) like attenuation, backscatter, scatter size, and acoustic concentration [1-5]. Ultrasonic

attenuation is defined as the loss of energy of the ultrasound wave as it propagates in the medium. Studies have shown that as the delivery time approaches the collagen rich cervix is filled with water and enzymes which results in a lower attenuation value and a softening of the cervix as it prepares for delivery [23-25]. Our earlier work showed that attenuation of the cervix decreased as the cervix prepared for delivery [8-12] while the softening of the cervix can also be quantified using shear wave elastography [13-15].

Over the years many algorithms have been developed for calculating ultrasonic attenuation. They can be classified as time domain algorithms and frequency domain algorithms. Time domain algorithms [26, 27] are computationally faster and easier to implement than frequency domain algorithms. However, it is difficult to compensate for diffraction effects and hence are not preferred over frequency domain algorithms when using array transducers.

Frequency domain algorithms can be further sub classified into the spectral shift, spectral difference, spectral log difference, and hybrid method. Spectral shift algorithm calculates the downshift of the center frequency of the power spectrum at different depths [28, 29]. Spectral shift algorithms are very sensitive to local spectral noise artifacts and also correcting for focusing in spectral shift algorithm is difficult [30]. Hence they are not commonly used with array transducers. Whereas spectral difference algorithms calculate the amplitude decay of the power spectra with respect to depth [31]. Spectral difference algorithms fail at tissue boundaries with varying backscatter. The spectral difference algorithm is a reference phantom technique and hence uses a calibrated reference phantom (known QUS parameters) to reduce the effect of system and transducer dependency as well as diffraction effects [32, 33]. The spectral log difference algorithm is also reference phantom technique but has a weaker dependence on backscatter changes [3, 34, 35]. A hybrid algorithm was proposed which combines the spectral

difference and spectral shift algorithms to reduce the impact of diffraction, system dependent parameters, and variations in backscatter at boundaries[36]. Labyed et al. (2011) simulated a comparison between spectral difference, spectral log and hybrid method to conclude that there was not a significant difference in performance between hybrid and spectral log difference in terms of dependence on changing scattering properties and ROI size [37]. For the purpose of this study, only spectral difference and spectral log difference algorithms were studied. Spectral log difference algorithm is less sensitive to changes in scattering but requires larger ROI size, whereas spectral difference algorithm works well for smaller ROI sizes but is highly sensitive to inhomogeneity of the backscattering tissues. ROI is defined as the amount of RF cervical data required to calculate one estimate of attenuation which would be overlaid on the attenuation map. The lateral dimensions are in terms of the number of independent echoes while the axial dimensions are given in terms of the number of pulse lengths used to calculate the changes in the backscattered power spectrum with depth. The aims of this study was to determine which algorithm will perform better for the cervix and to identify the optimal ROI size for spectral difference and Spectral log difference algorithm for the cervix, since the optimum ROI size for cervix has not been identified before.

2.2 Materials and Methods

A study was conducted on sixty three pregnant African-American women, since they have a high rate of preterm birth [38]. The study was approved by the Human Subjects Review Board of the University of Illinois at Chicago. Subjects were inducted into the study only if they met the following criteria's: older than 18 years of age; able to read, write and comprehend English; no immune disorder; not on steroids; don't have diabetes. Women with anomalous fetus or too ill to give consent were omitted from the study. The subjects were expected to undergo

five transvaginal ultrasound examinations between planned intervals of 17-39 weeks of gestational age. Some subjects could not attend all the 5 planned exams, hence fewer scans for those subjects were taken.

Ultrasonic data were acquired with an E9-4 endovaginal transducer from z.one Zonare ultrasound system (ZONARE Medical Systems, Mountain View, CA). The transducer has a center frequency of 6.8 MHz and a bandwidth of 2.4 MHz, with a penetration depth of 11.5cm. A preset was used on the ultrasound machine to remove operator bias and to ensure that the machine settings didn't change from one scan to another. The sonographer had the flexibility of choosing the depth of the scan but the depth was to be kept same throughout the scan. The sonographer scanned the subject at three different center frequencies of 4, 5 and 8 MHz, immediately after each cervical scan the sonographer scanned a tissue mimicking phantom using the same preset settings. A custom built Gammex (Gammex Inc., Middleton, WI) tissue mimicking phantom (series 0.5LE) was used as the reference phantom and had a known attenuation of 0.5 dB/cm-MHz as given by the manufacturer and independently verified in our laboratory. The phantom had no occlusions and had a uniform backscatter. The phantom had scattering targets of average scatter diameter of 35 μ m with a number density of 160mm⁻³. A calibrated reference phantom is required to calculate the attenuation of the cervix so as to cancel the effects of diffraction term and machine transmit/receive characteristics [39]. The date of delivery was also noted for each subject by following up with the patient after the completion of the scans. In addition, the cervical length was measured from the ultrasound images acquired from each scan.

Ultrasonic IQ (in-phase quadrature) data was obtained from the z.one Zonare ultrasound system (ZONARE Medical Systems, Mountain View, CA). The IQ data was stripped of all

personal data and was sent for calculation of attenuation values. Figure 1 summarizes the process of calculating attenuation value for the cervix from the IQ data. The engineer processing the attenuation value was unaware of the gestation age of the scan. The IQ data was imported into MATLAB (MathWorks Inc., Natick, MA. USA) and was converted to RF (radio frequency) data. The RF data for the whole image was decomposed into multiple ROI to calculate the attenuation value of each ROI. The ROIs were further windowed using a rectangular windowing function with windows overlapping by 50% in the axial direction. The Fourier transform of each windowed data is calculated and the spectrogram is plotted to determine the noise level for the particular scan and frequency. An average value of -17 dB bandwidth was used which was at least 5dB above the noise floor. The usable frequency range is also calculated from the spectra (average bandwidth of 3.4-7.1 MHz). Since 3 frequencies were available, the spectral values from the 3 frequencies lying in the usable frequency range were averaged as shown in figure 2. The -20 dB cutoff used in the example figure 2 is for each frequency and not for the combined spectrum as each frequency has a different maximum, hence the combined spectrum doesn't exactly terminate at -20 dB. The reference scan was processed in a similar manner. The average spectral value of all the windows in the usable frequency range is divided by the average reference spectral value to cancel the diffraction term. An attenuation map of the cervix was then generated by using either the spectral difference algorithm or the spectral log-difference algorithm.

Spectral difference is more sensitive to changes in backscatter resulting from tissue heterogeneity [39]. Whereas the spectral log difference algorithm is less sensitive to changes in

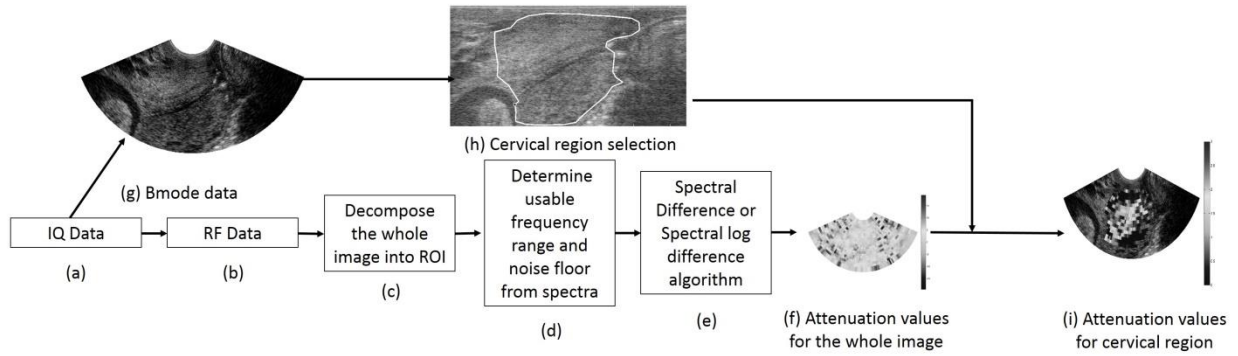


Figure 1. Summary of the process for calculating attenuation estimate. (a) IQ data is converted to (b) RF data. (c) The whole image is decomposed into ROI. (d) Spectra is plotted and usable frequency range and noise floor are detected. (e) Windowed ROI are processed for attenuation using spectral difference or spectral log difference algorithm. (f) Attenuation map is overlaid on the B mode image. (g) B mode data is taken and (h) cervical region is selected from it. (i) The selected region is segmented from the attenuation map.

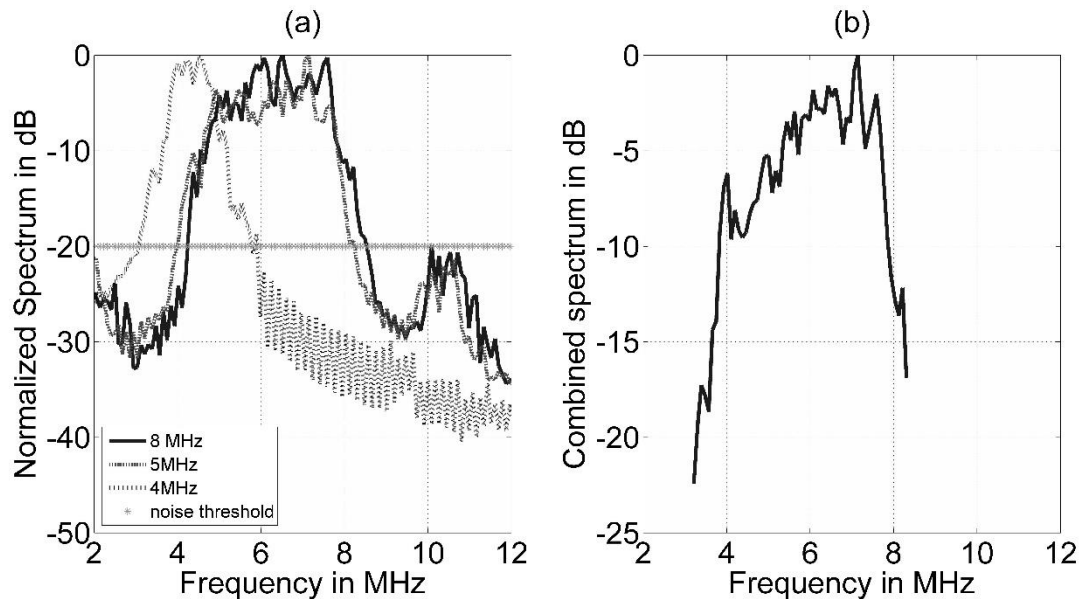


Fig. 2: Selection of usable bandwidth by averaging the three spectrums and thresholding the noise. (a) Spectrum of the three frequencies along with the noise threshold. (b) Thresholded spectrum averaged over the three frequencies.

backscatter, but it requires computing the changes in the backscattered power spectrum over a larger region for the same variance in the attenuation estimate (poorer attenuation-map resolution). We hypothesized that the smaller ROI sizes allowed with the spectral difference algorithm might compensate for its increased sensitivity to backscatter changes from tissue heterogeneity as tissue heterogeneity may be less pronounced over smaller scattering regions. Therefore, both the algorithms were used in this study. The two algorithms for calculating attenuation are summarized below.

To calculate the attenuation using spectral difference algorithm the power spectrum of a windowed region is written as

$$S_s(f, z) = P(f)D_s(f, z)A_s(f, z_0)B_s(f, z)e^{-4\alpha_s(f)(z-z_0)} \quad (2.1)$$

where subscript s represents the sample, f is the frequency, z is the distance from surface of the transducer to the center of time gated window within the ROI, z_0 is the start of the ROI, P is the electro-acoustic and acousto-electric transfer functions, D is the diffraction term, A is the cumulative attenuation along the path of propagation, B is the backscatter term, α is the attenuation coefficient of the ROI. Similarly the power spectrum for the reference phantom can be written as S_r . The diffraction terms can be removed from the above equations by assuming that the speed of sound is approximately the same in the tissue and tissue mimicking phantom. If the tissue within an ROI is assumed to be homogenous and isotropic then the scattering term does not depend on the depth. Dividing the two spectra and taking natural logarithm gives us equation (2.2)

$$\ln \left[\frac{S_s(f, z)}{S_r(f, z)} \right] = R(f, z) = 4(z - z_0)(\alpha_r(f) - \alpha_s(f)) + \ln \left[\frac{A_s(f, z_0)B_s(f)}{A_r(f, z_0)B_r(f)} \right] \quad (2.2)$$

The attenuation can be assumed to increase linearly with frequency and can be expressed as $\alpha = \beta f$ [40]. The attenuation coefficient can then be calculated by finding the slope of a

straight line that fits the log ratio of the two spectra for each frequency. Replacing the value of alpha and differentiating equation (2.2) with respect to depth we get.

$$\frac{dR(f,z)}{dz} = 4(\alpha_r(f) - \beta_s f) \quad (2.3)$$

Equation (2.3) can be rearranged as

$$\beta_s f = \alpha_r(f) - \frac{1}{4} \frac{dR(f,z)}{dz} \quad (2.4)$$

The attenuation coefficient β_s can be found by dividing equation (2.4) by the frequency at each Fourier component and computing the average.

Spectral log difference algorithm only uses the proximal and distal window of the ROI. The proximal and distal windows would be the window closest to the transducer (proximal) and furthest from the transducer (distal) associated with a specific ROI. We can rewrite equation (2.2) for the proximal and distal window with respect to the phantom separately. Now subtract the proximal and distal window power spectrum ratios, this gives us equation (2.5)

$$SS(f) = \ln \left[\frac{S_s(f, z_p)}{S_r(f, z_p)} \right] - \ln \left[\frac{S_s(f, z_d)}{S_r(f, z_d)} \right] = 4(z_p - z_d)(\alpha_r(f) - \alpha_s(f)) + \ln \left[\frac{A_s(f, z_0) B_s(f, z_p)}{A_r(f, z_0) B_r(f, z_p)} \right] - \ln \left[\frac{A_s(f, z_0) B_s(f, z_d)}{A_r(f, z_0) B_r(f, z_d)} \right] \quad (2.5)$$

Since the phantom is homogenous and isotropic the back scattering term for the proximal and distal window for the reference is same. Also if the effective scatter size of the proximal and distal window is the same we can assume that backscatter of proximal and distal windows for the tissue are different only by a multiplicative constant. So now the equation becomes

$$SS(f) = 4(\alpha_r(f) - \alpha_s(f))(z_p - z_d) + constant \quad (2.6)$$

After replacing α and assuming that attenuation increases linearly with frequency. The slope of the line fitting the substituted equation (2.6) will give us attenuation estimate for the corresponding ROI as shown in equation (2.7).

$$\beta_s f = \alpha_r(f) - \frac{SS(f) - constant}{4(z_p - z_d)} \quad (2.7)$$

The size of the ROI was varied in both the axial and lateral direction. Our previous studies have shown that approximately 15 pulse lengths in the axial direction and 15 pulse lengths in the axial direction and 15 echoes in the lateral direction gave a standard deviation on the order of 25% in the attenuation estimates for simulations, phantom experiments, and in the rat cervix when using the spectral log difference algorithm, while the spectral difference algorithm had a standard deviation of less than 13% for the same ROI size [9, 37, 39]. The pulse length was calculated by taking the auto correlation coefficient of time samples from RF echo lines of the phantom data. Samples with absolute correlation coefficient greater than 0.2 were considered correlated and determined the time pulse length. The spatial pulse length or simply the pulse length can then be calculated by multiplying time pulse length with the speed of sound and dividing by 2. In the axial direction, the ROI is divided into time gated windows to calculate the Fourier transform at each depth. These time gated windows were overlapped 50% with each other and the size of each window was decided at 7 pulse length per window by plotting the -6dB bandwidth against the number of spatial pulse length and observing the number of pulse lengths at which the -6dB bandwidth becomes constant. The size of the ROI was then varied by varying the number of windows in the ROI. We picked ROI size so that 2, 3 and 4 windows can fit into the ROI which corresponds to 10.5, 14, 17.5 pulse length in axial direction (6.468, 8.624, 10.780 mm). In the lateral direction, the ROI was varied between 5, 10, 15 and 20 independent echoes (6.32, 12.65, 18.98, 25.31mm), where every third echo was determined to be independent. All possible combination of the above mentioned pulse length and echo sizes were

used for the size of the ROI. The algorithms and ROI sizes were then compared in terms of their diagnostic potential via receiver operator characteristic (ROC) curves.

2.3 Results

Some of the subjects missed the planned scan intervals or were late by a few week due to missed appointments or preterm birth. Subjects with medically induced preterm birth were excluded from the analysis. Hence the number of scans per subject varied from one to five. The patient data was grouped so that a scan taken at a Gestational age of 16-22 weeks was treated as scan 1, 23-26 weeks as scan 2, 27-30 weeks as scan 3, 31-34 weeks as scan 4 and 35 weeks onwards as scan 5. If a subject was imaged more than once in these defined periods due to variability in scheduling, the attenuation estimate from the different images was averaged to yield one value for each patient for each scan interval. Out of the 63 subjects, 53 had full term birth whereas 10 had preterm birth. In total 221 ultrasound scans were obtained, the scans were processed for attenuation values using the two different algorithms. The ROI size was varied during the processing thus there were cases in which the ROI size was larger than the cervical region hence an estimate for attenuation could not be calculated. This scenario was specifically significant for ROI size of 17.5 pulse length and 20 echoes also for scan 5 when the cervix size is smaller. Table 1 shows the number of scans with valid attenuation estimate for the various pulse length and echoes.

Table 1: Number of valid attenuation estimates for different ROI sizes

	Scan 1	Scan 2	Scan 3	Scan 4	Scan 5
5 Echoes	49	51	48	40	32
10 Echoes	49	51	48	40	32
15 Echoes	49	51	48	40	32
20 Echoes	49	51	49/48*	40	32

* 49 for pulse length of 10.5, whereas 48 for pulse length of 14 and 17.5.

Figure 3,4,5,6 show the normalized attenuation versus gestational age in weeks. Both the Spectral difference and spectral log difference algorithm are presented. The average attenuation value of the first three scans is treated as the normalizing value for each algorithm. The normalization was done as the spectral difference algorithm consistently resulted in lower attenuation values compared to the spectral log difference algorithm. The number of echoes remains constant in each figure as the ROI pulse length varies. The normalized attenuation values (vertical axis) are plotted versus the average gestational age (horizontal axis) for each of the five scan groups. The normalized attenuation of spectral difference for full term remains approximately constant for all five scans, but decreases after the third scan for preterm cases. For the spectral log difference the full term cases are approximately constant for the first four scan and decreases for the fifth scan whereas for the preterm cases the attenuation starts decreasing after the third scan. We would expect the attenuation of the cervix to decrease as we approach delivery due to the biological changes necessary for cervical softening.

Figure 18 to 29 in appendix B show all the figures for attenuation vs gestation age with respect to varying ROI size for Spectral log difference algorithm. Figure 30 to 41 in appendix B show all the figures for attenuation vs gestation age with respect to varying ROI size for Spectral difference algorithm. Figure 42 to 53 in appendix B show all the figures for change in attenuation vs time to delivery with respect to varying ROI size for Spectral log difference algorithm. Figure 54 to 65 in appendix B show all the figures for change in attenuation vs time to delivery with respect to varying ROI size for Spectral difference algorithm.

Table 2 shows the attenuation mean and standard error of mean values for spectral log difference algorithm. Since the attenuation value did not change significantly ($p>0.6$) over the

first three scans, the attenuation value of the first three scans has been averaged into one. The attenuation value for the full term stays constant for the first four scans, whereas it decreases for

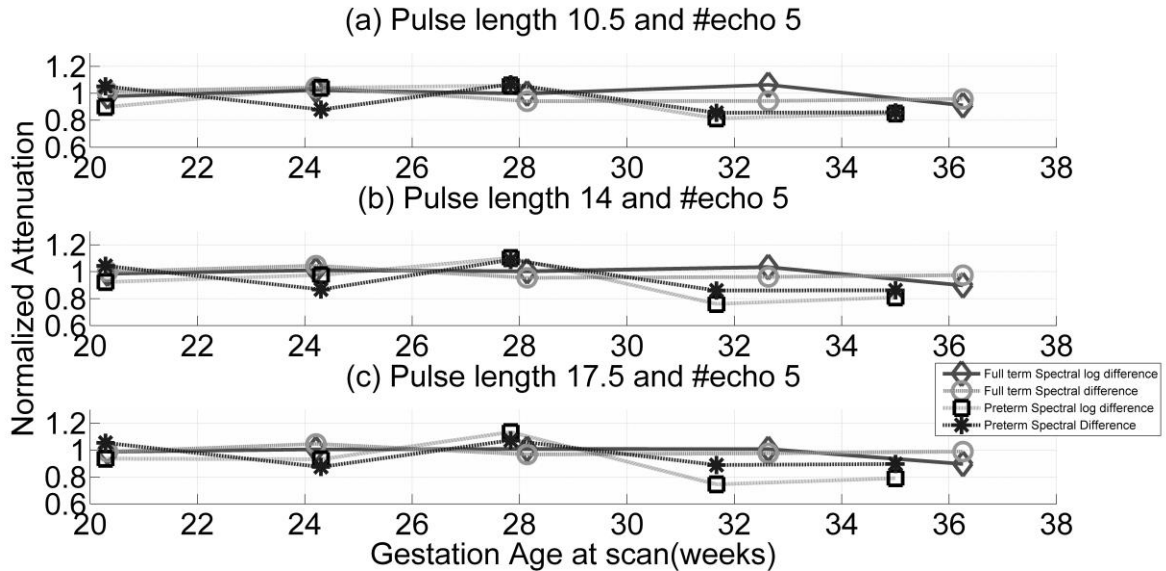


Fig. 3: Comparison of normalized attenuation estimate versus gestation age for full term and preterm spectral log difference and spectral difference algorithm for varying ROI size (a) pulse length 10.5 and 5 echoes, (b) pulse length 14 and 5 echoes, (c) pulse length 17.5 and 5 echoes.

the fifth scan ($p < 0.05$ for ROI size 10.5 pulse length and 5 echoes, change for other pixel sizes not statistically significant). In case of spectral log difference preterm birth, a decreasing trend can be seen around scan 4 and it follows into scan 5. Similarly Table 3 shows the values of attenuation and standard error of mean for spectral difference algorithm. Spectral difference attenuation values for full term appear to increase from the fourth scan to fifth scan, but the change is not statistically significant for our sample sizes. The Spectral difference preterm birth attenuation values do decrease from scan 3 to scan 4 and follows the same trend into scan 5. The attenuation estimate for each algorithm doesn't change significantly with the changing ROI size and hence the ROI size doesn't have a huge impact on estimation of attenuation.

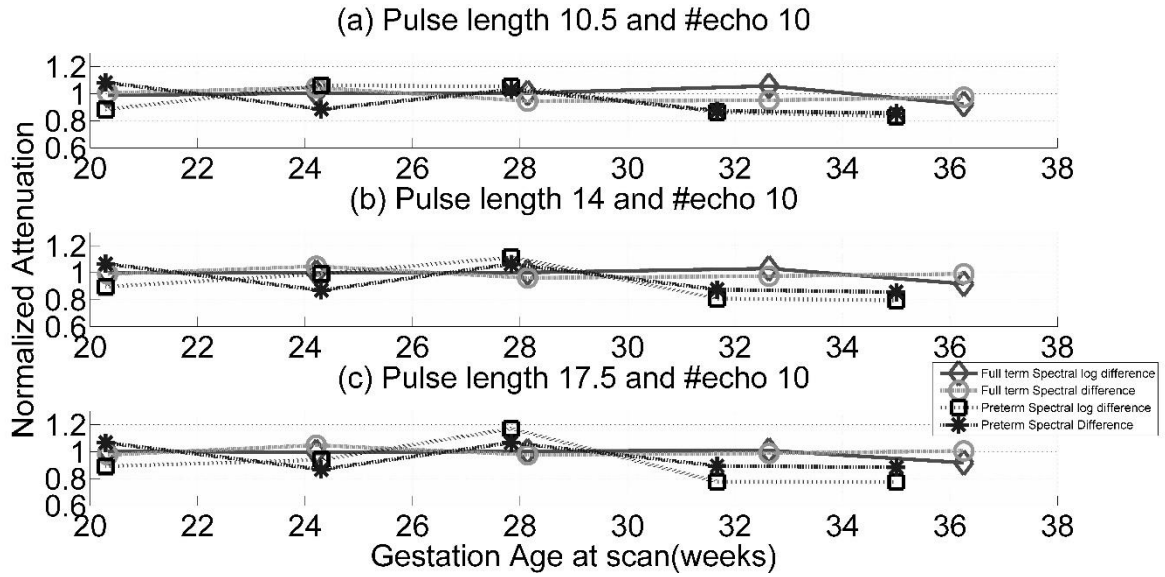


Fig. 4: Comparison of normalized attenuation estimate versus gestation age for full term and preterm spectral log difference and spectral difference algorithm for varying ROI size (a) pulse length 10.5 and 10 echoes, (b) pulse length 14 and 10 echoes, (c) pulse length 17.5 and 10 echoes.

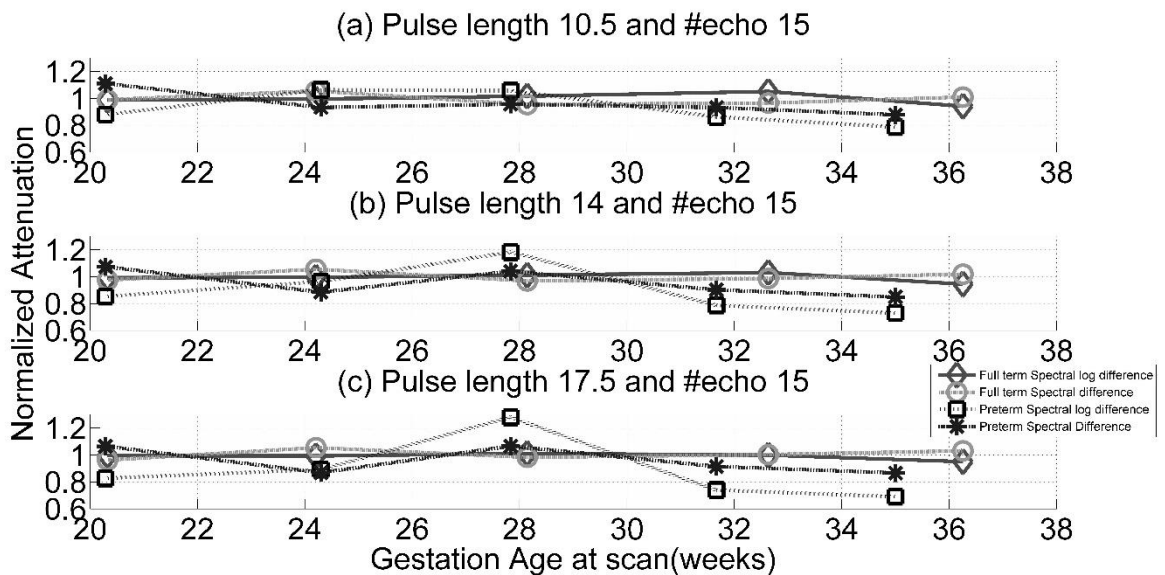


Fig. 5: Comparison of normalized attenuation estimate versus gestation age for full term and preterm spectral log difference and spectral difference algorithm for varying ROI size (a) pulse length 10.5 and 15 echoes, (b) pulse length 14 and 15 echoes, (c) pulse length 17.5 and 15 echoes.

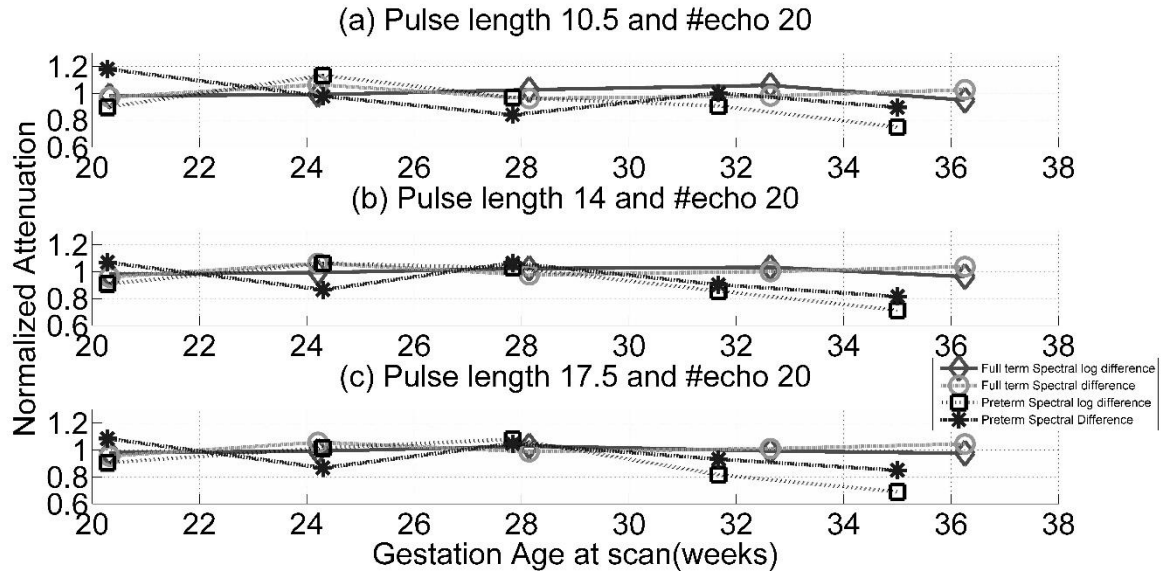


Fig. 6: Comparison of normalized attenuation estimate versus gestation age for full term and preterm spectral log difference and spectral difference algorithm for varying ROI size (a) pulse length 10.5 and 20 echoes, (b) pulse length 14 and 20 echoes, (c) pulse length 17.5 and 20 echoes.

Table 2: Attenuation mean and standard error of mean values for spectral log difference algorithm (a) full term case

(pulse length, echo)	Spectral log difference full term attenuation value mean±sem(std)		
	Average of first 3 scans	4 th scan	5 th scan
(10.5,5)	1.36±0.06(0.40)	1.45±0.09(0.48)	1.24±0.06(0.33)
(10.5,10)	1.35±0.06(0.38)	1.43±0.08(0.48)	1.25±0.06(0.34)
(10.5,15)	1.35±0.06(0.38)	1.41±0.09(0.50)	1.27±0.07(0.36)
(10.5,20)	1.33±0.06(0.39)	1.41±0.09(0.53)	1.26±0.07(0.38)
(14,5)	1.36±0.06(0.40)	1.41±0.08(0.47)	1.22±0.06(0.36)
(14,10)	1.35±0.06(0.38)	1.39±0.08(0.47)	1.24±0.06(0.36)
(14,15)	1.33±0.06(0.39)	1.37±0.09(0.49)	1.26±0.07(0.37)
(14,20)	1.31±0.06(0.40)	1.35±0.09(0.49)	1.26±0.07(0.39)
(17.5,5)	1.35±0.07(0.42)	1.36±0.08(0.46)	1.21±0.06(0.35)
(17.5,10)	1.34±0.06(0.40)	1.35±0.08(0.47)	1.23±0.06(0.35)
(17.5,15)	1.32±0.07(0.41)	1.32±0.08(0.46)	1.26±0.07(0.37)
(17.5,20)	1.30±0.07(0.44)	1.29±0.08(0.48)	1.27±0.07(0.39)

Table 2: Attenuation mean and standard error of mean values for spectral log difference algorithm (b) preterm case

(pulse length, echo)	Spectral log difference preterm birth attenuation value mean±sem(std)		
	Average of first 3 scans	4 th scan	5 th scan
(10.5,5)	1.26±0.16(0.35)	1.05±0.09(0.15)	1.10±NA(NA)
(10.5,10)	1.23±0.15(0.34)	1.08±0.05(0.08)	1.04± NA(NA)
(10.5,15)	1.22±0.15(0.34)	1.08±0.03(0.06)	0.98± NA(NA)
(10.5,20)	1.18±0.16(0.35)	1.08±0.04(0.07)	0.89± NA(NA)
(14,5)	1.28±0.16(0.36)	1.00±0.10(0.17)	1.06± NA(NA)
(14,10)	1.25±0.15(0.33)	1.04±0.08(0.14)	1.02± NA(NA)
(14,15)	1.27±0.16(0.36)	1.04±0.08(0.14)	0.97± NA(NA)
(14,20)	1.20±0.16(0.34)	1.05±0.10(0.17)	0.87± NA(NA)
(17.5,5)	1.26±0.16(0.36)	0.96±0.10(0.17)	1.02± NA(NA)
(17.5,10)	1.24±0.15(0.34)	1.00±0.11(0.18)	1.00± NA(NA)
(17.5,15)	1.28±0.18(0.41)	1.01±0.12(0.21)	0.94± NA(NA)
(17.5,20)	1.19±0.16(0.35)	1.00±0.14(0.25)	0.85± NA(NA)

Table 3: Attenuation mean and standard error of mean values for spectral difference algorithm (a) full term case

(pulse length, echo)	Spectral difference full term attenuation value mean±sem(std)		
	Average of first 3 scans	4 th scan	5 th scan
(10.5,5)	0.79±0.03(0.21)	0.74±0.05(0.26)	0.76±0.03(0.16)
(10.5,10)	0.78±0.04(0.22)	0.75±0.05(0.26)	0.77±0.03(0.17)
(10.5,15)	0.78±0.04(0.24)	0.75±0.05(0.27)	0.79±0.03(0.18)
(10.5,20)	0.78±0.04(0.25)	0.77±0.05(0.28)	0.80±0.04(0.20)
(14,5)	0.79±0.03(0.21)	0.76±0.05(0.26)	0.77±0.03(0.15)
(14,10)	0.78±0.04(0.23)	0.76±0.05(0.26)	0.77±0.03(0.15)
(14,15)	0.78±0.04(0.24)	0.77±0.05(0.28)	0.79±0.03(0.16)
(14,20)	0.78±0.04(0.25)	0.78±0.05(0.27)	0.81±0.03(0.17)
(17.5,5)	0.78±0.03(0.22)	0.76±0.05(0.26)	0.77±0.03(0.15)
(17.5,10)	0.78±0.04(0.23)	0.77±0.05(0.26)	0.78±0.03(0.15)
(17.5,15)	0.77±0.04(0.25)	0.77±0.05(0.27)	0.79±0.03(0.15)
(17.5,20)	0.78±0.04(0.26)	0.79±0.05(0.27)	0.81±0.03(0.16)

Table 3: Attenuation mean and standard error of mean values for spectral difference algorithm
(b) preterm case

(pulse length, echo)	Spectral difference preterm birth attenuation value mean±sem(std)		
	Average of first 3 scans	4 th scan	5 th scan
(10.5,5)	0.78±0.07(0.15)	0.67±0.05(0.08)	0.67± NA(NA)
(10.5,10)	0.77±0.07(0.16)	0.67±0.04(0.07)	0.65± NA(NA)
(10.5,15)	0.75±0.08(0.19)	0.68±0.04(0.06)	0.64± NA(NA)
(10.5,20)	0.73±0.11(0.24)	0.70±0.04(0.06)	0.62± NA(NA)
(14,5)	0.78±0.07(0.15)	0.67±0.06(0.10)	0.68± NA(NA)
(14,10)	0.77±0.07(0.16)	0.67±0.05(0.08)	0.66± NA(NA)
(14,15)	0.77±0.07(0.16)	0.69±0.05(0.08)	0.65± NA(NA)
(14,20)	0.77±0.08(0.18)	0.70±0.04(0.08)	0.63± NA(NA)
(17.5,5)	0.77±0.07(0.16)	0.68±0.06(0.10)	0.69± NA(NA)
(17.5,10)	0.76±0.07(0.16)	0.68±0.05(0.09)	0.68± NA(NA)
(17.5,15)	0.76±0.07(0.16)	0.70±0.05(0.08)	0.66± NA(NA)
(17.5,20)	0.76±0.08(0.17)	0.71±0.04(0.08)	0.65± NA(NA)

There is a difference in attenuation values calculated from the two algorithm. The spectral difference algorithm always gives lower value of attenuation as compared to the spectral log difference algorithm for the same cervical region. Since the actual attenuation of the cervix is unknown it's difficult to say how much bias is present in each algorithm. The cervix softens by 76mbar between the first trimester and the second trimester, whereas the change between second trimester and third trimester is just 24mbar as calculated by the aspiration technique [7]. This study wanted to capture and confirm the softening of the cervix using ultrasonic attenuation from second trimester to third trimester thus helping in predicting the time of birth. Studies have shown that a softer cervix corresponds to lower attenuation [23-25]. Since full term spectral difference algorithm does not follow this trend and spectral difference algorithm is known to be very sensitive to heterogeneity of the ROI data, it can be assumed that spectral difference

algorithm is the one malfunctioning. A sanity check was performed on both the algorithms using the Gammex tissue mimicking phantom. Spectral difference algorithm gave us a mean attenuation value of 0.5037 ± 0.0459 and spectral log difference algorithm gave us a mean attenuation value of 0.5120 ± 0.3304 when using an ROI size of 17.5 pulse lengths and 15 echoes. Which indicates both attenuation algorithms give the same attenuation value when the imaged region is homogeneous.

Among the two algorithms spectral log difference is in congruence with the biologically anticipated changes occurring in the cervix as it prepares for delivery, whereas spectral difference results are biased due to the presence of heterogeneous tissue and are incongruent with the biologically anticipated changes. To compare the diagnostic potential of the two algorithms and better understand the potential impact of the observed trends, receiver operating characteristic (ROC) curves were plotted. The area under the ROC curve gives us the true positive rate for estimation of preterm birth by cervical attenuation measurement. The ROC curves are calculated for the fourth scan to check if it can detect a case of preterm birth or not. Table 4 and 5 summarize the area under the receiver operating characteristic (ROC) curve for spectral log difference and spectral difference algorithm. Figure 66 to 77 in appendix B show all ROC plots for varying ROI size for Spectral log difference algorithm. Figure 78 to 89 in appendix B show all ROC plots for varying ROI size for Spectral difference algorithm. Spectral log difference has higher ROC values and might be considered a better predictor of preterm birth as compared to Spectral difference algorithm. The highest area under the ROC curve was 0.75 which may not be sufficient for diagnostic purposes. However attenuation could potentially be combined with other QUS parameters to improve the efficacy. Other methods to improve

efficacy could involve additional signal processing to further reduce the impact of tissue heterogeneity.

Table 4: ROC values for spectral log difference algorithm

ROC LD	5 echoes	10 echoes	15 echoes	20 echoes
10.5 pulse lengths	0.75	0.73	0.74	0.67
14 pulse lengths	0.75	0.68	0.72	0.67
17.5 pulse lengths	0.74	0.72	0.67	0.65

Table 5: ROC values for spectral difference algorithm

ROC SD	5 echoes	10 echoes	15 echoes	20 echoes
10.5 pulse lengths	0.59	0.61	0.59	0.59
14 pulse lengths	0.61	0.64	0.61	0.59
17.5 pulse lengths	0.64	0.64	0.61	0.58

2.4 Discussion

Selection of ROI size and proper attenuation estimation algorithm plays a vital role in calculation of attenuation for tissue characterization. Our previous studies simulated the role of ROI size in calculation of attenuation and found that the Spectral Log difference algorithm is less dependent on the homogeneity assumption for the tissue compared to the Spectral difference algorithm, but the Spectral Difference algorithm was more precise when the tissue was homogeneous [39]. In addition, our simulations showed that if the ROI size is small, the attenuation estimates obtained will have higher variance [39]. However, the homogeneity assumption might be better approximated by smaller ROI sizes. In our study of ultrasound attenuation assessment of human cervix tissue, ROI size was varied from 10.5 pulse length to

17.5 pulse length in axial direction and 5 echoes to 20 echoes in lateral direction. But it was observed that the ROI size did not have any impact on the attenuation estimate. The variance did not decrease as the ROI size was increased. Hence, the inherent heterogeneity of the cervix is dominating the variance in the attenuation estimate.

The cervix is mainly composed of collagen with relatively few smooth muscle bundles. The alignment of collagen varies from one layer to another with inner and outer layer having collagen arranged longitudinally, however middle layer has circumferentially aligned collagen [15, 41, 42]. As the cervix remodels for birth the cervix softens before the cervical length decreases (after 30 weeks of gestation age) which happens along with change of collagen concentration [43]. The different alignment and concentration of collagen causes the cervix to behave like a heterogeneous medium.

The impact of the heterogeneity of the cervix is also evident in the superior performance of the Spectral Log Difference algorithm over the Spectral Difference Algorithm. The Spectral Log Difference algorithm showed a clear trend of decreasing attenuation with increasing gestational age. In addition, the largest area under the ROC curve when using the Spectral Log Difference algorithm was 0.75 whereas it was only 0.64 for the Spectral Difference algorithm. Therefore, the Spectral Log Difference algorithm should be used in the future when characterizing the cervix. In addition, methods to further reduce the impact of the tissue heterogeneity should be explored.

Despite the impact of the heterogeneity, the trend established by our earlier studies is confirmed in this study. The cervix remodels as it prepares to deliver and these changes can be monitored non-invasively using diagnostic ultrasound. The major change is observed in the last 5 weeks as the attenuation value decreases in accordance with the softening of the cervix as it

prepares for birth. The changes in attenuation value for preterm birth start occurring before the corresponding changes in full term birth, which can help in identifying preterm birth. Presently cervical length is used as an estimator of preterm birth and has a positive predictive value of 25-52% [20]. Most of the studies using cervical length try to identify preterm birth before 30 weeks of gestation age. Cervical length was also measured for our study. Scan 3, which corresponds to 27-30 weeks of gestation age, has a sensitivity of 33.3%, specificity of 93%, PPV of 20%, NPV of 95.1% for a cutoff of 25mm which is comparable to other studies [20]. Since attenuation doesn't change till scan 4 which falls in 31-34 weeks of gestation age, comparing the cervical length with attenuation is not feasible at this stage. Therefore, for the purpose of comparison, the ROC plot for cervical length for scan 4 was studied with the same 25 mm cutoff. Scan 4 had a sensitivity of 33.3%, specificity of 92.1%, PPV of 25%, NPV of 94.6% (Figure 90 Appendix B). A simple metric to improve the ROC statistics is to multiply the cervical length and normalized attenuation value for Scan 4. The attenuation was normalized by dividing the attenuation value by the mean attenuation value of the first three scans on a patient specific basis. Since both the cervical length and attenuation value decrease as delivery approached their combined metric gave us a better statistical results with a sensitivity of 66.7%, specificity of 90.6%, PPV of 40%, NPV of 96.7% for a cutoff of 25mm (Figure 91 Appendix B). Therefore, ultrasonic attenuation when coupled with cervical length gives a better estimate of preterm birth prediction. However, our study should be confirmed using a larger patient population of women with preterm birth.

CHAPTER 3

GAMMA MIXTURE MODEL: PHANTOM AND SIMULATION

3.1 Introduction

In chapter 2, we concurred that ROI size does not influence the estimation of attenuation. We also observed that the standard deviation for both the algorithms was exceptionally high which can be attributed to the fact that these algorithms are developed with the basic assumption that the tissue region is homogenous. Since in the real case the cervix is a very heterogeneous tissue these assumptions fail. Spectral difference algorithm is more sensitive to homogeneity of the tissue and performs worse than spectral log difference algorithm. In order to get valid estimates of attenuation, the ROI should be homogenous. So in chapter 3 an attempt is made to segment regions of different scatterings. To understand the echo heterogeneity we need to look into the scattering parameters of the tissue.

Ultrasound images have a characteristic granular pattern called speckle. Speckle occurs due to the scattered wavelength interfering constructively or destructively within a resolution cell having many scatterer's. Speckle degrades the quality of the diagnostic image but provides relevant data about the underlying tissue microstructure. Speckle is a multiplicative noise which depends upon the scatterer size and the number of scatterer's per resolution cell.

Speckle statistics can give insight into tissue microstructure and be used as a tissue histological descriptors[44]. Scatter number density and scatter size strongly influence the speckle statistics. Speckle noise can be either fully developed or partially developed depending upon the nature of the reflected signal (diffused or specular). Speckle can also be classified as fully resolved (spacing between scatterer's greater than 2λ) or partially resolved. First order

statistics of the echo envelope can be modeled using different distributions. If the number density of scatterer's is high and the speckle is fully developed, it is modeled by Rayleigh probability density function. The echo signal from multiple random reflections in a sample volume can be modeled as:

$$s(t) = x(t) \cos(\omega_0 t) - y(t) \sin(\omega_0 t) \quad (3.1)$$

where ω_0 is the center frequency and the quadrature components $x(t)$ and $y(t)$ are independent and zero-mean Gaussian. The envelope $r(t)$ can then be expressed as:

$$r(t) = \sqrt{x^2(t) + y^2(t)} \quad (3.2)$$

The Rayleigh probability density function can then be written as:

$$f_R(r) = \frac{r}{\sigma^2} e^{-\frac{r^2}{2\sigma^2}} u(r) \quad (3.3)$$

where σ is the standard deviation of the quadrature components and $u(\cdot)$ is the Heaviside step function defined as:

$$u(x) = \begin{cases} 0 & x < 0 \\ 1 & x \geq 0 \end{cases} \quad (3.4)$$

B-mode images formed using the envelope of RF data with no coherent component are perfect examples of Rayleigh statistics[45, 46]. However, deviations from Rayleigh statistics is quite common. Rice distribution is used when speckle is fully resolved with high number density but in the presence of deterministic component[47, 48]. Rayleigh distribution is a special case of rice distribution, when the coherent signal component is zero. Rice distribution is given by the following equation:

$$f_R(r) = \frac{r}{\sigma^2} I_0\left(\frac{rC}{\sigma^2}\right) e^{-\frac{(r^2+c^2)}{2\sigma^2}} u(r) \quad (3.5)$$

where $I_0(\cdot)$ is the modified Bessel function of first kind and C is the specular component.

Partially developed speckle with low number density and no deterministic component can be modeled using K distribution. The K distribution relates to physical parameters like density of random scatterer's. K distribution pdf is given by

$$f_R(r) = \frac{2}{b\Gamma(v+1)} \left(\frac{\sigma}{2b^2}\right)^{v+1} K_v\left(\frac{r}{b}\right) u(r) \quad (3.6)$$

where $K_v(\cdot)$ is the modified Bessel function of the second kind, b is the mean and v is the shape parameter. Partially resolved speckle with a low number density and existence of deterministic component is modeled by homodyned K distribution[49, 50]. Distributions with more than one parameters were also introduced like the Nakagami distribution and the three parameter distributions like the Rician inverse Gaussian distribution and generalized k-distribution.

Nakagami distribution is a two parameter generalization of the Rayleigh distribution. Nakagami distribution is commonly used for modeling fully developed speckle [51-53]. The Nakagami PDF is given by:

$$f_R(r) = \frac{2m^m r^{2m-1}}{\Gamma(m)(2\Omega)^m} e^{-\left(\frac{m}{2\Omega}\right)r^2} u(r) \quad (3.7)$$

where m is the shape parameter and Ω is the controlling spread. Nakagami distribution does not perfectly model the real life cases of ultrasound images. The failure to perfectly model real life images can be attributed to the acquisition process and the post-processing. The center frequency also effects the number density of the scatterer's resulting in deviations from Rayleigh and Nakagami statistics. Two parameter distributions like Gamma distributions have shown to give better empirical results when compared with Rayleigh distribution, K distribution, Nakagami distribution and the inverse Gaussian distribution[54]. Post processing techniques like log compression and filtering also effect the envelope of the RF data. Gamma distribution has shown promising results for fitting real ultrasonic data for fully developed speckle [54-56]. In the above

mentioned works log compression and filtering were considered but no explanation was provided for Gamma distribution being a better model. Nakagami distribution is related to gamma distribution (if $Y \sim \text{Gamma}(k, \theta)$ then $x \sim \text{Nakagami}(m, \Omega)$ can be obtained by setting $k = m$, $\theta =$

$$\Omega/m \text{ and taking square root of } y; X(m, \Omega) = \sqrt{Y(m, \frac{\Omega}{m})}$$

A heterogeneous cervix will have scatterer's of varying scatter size and number density. Modeling heterogeneous tissue with one distribution only doesn't give a perfect distribution as the varying scatter size and number density will result in multiple distributions. So heterogeneous tissue needs to be modeled using a mixture model. We propose to use Gamma mixture model (GMM) for our study as it is shown to perform better than Rayleigh mixture model and Nakagami mixture model [57]. Unlike most distributions discussed till now gamma distribution does not correspond to any physical parameters related to scattering properties of the tissue.

This study wants to see if GMM can be used to identify regions of differing backscatter. The changes in backscatter are directly related to attenuation estimation, hence calculating attenuation estimates for a region with similar backscatter will give a more accurate estimate of attenuation.

3.2 Gamma mixture model and EM algorithm

The different echogenicity from the heterogeneous cervix should be modeled by a mixture of distribution hence a Gamma mixture model is proposed to differentiate between scatterer's of different size and number density. Let $\mathbf{X} = \{x_i\}, 1 \leq i \leq N$ be the pixel intensities of the IQ data obtained from an ultrasound scan. Assuming that these samples are independent and identically distributed (IID) random variable. If the pixel intensities are not IID

it can be achieved by down sampling the image after determining the auto correlation between the echo lines. The Gamma PDF can be defined for a set of pixel intensities X as:

$$f_x(x|\alpha, \beta) = \frac{x^{\alpha-1}}{\beta^\alpha \Gamma(\alpha)} e^{-\frac{x}{\beta}}, x \geq 0 \quad \alpha, \beta > 0 \quad (3.8)$$

where $\Gamma(\alpha)$ is Euler gamma function defined as $\Gamma(x) = \int_0^\infty t^{x-1} e^{-t} dt, x > 0$, α is the shape parameter, β is the scale parameter. If the GMM has a contributions of J different distributions, the PDF of the GMM can be written as:

$$p(x_i|\Theta) = \sum_{j=1}^J \pi_j f_x(x_i|\Theta_j) \quad (3.9)$$

where Θ is a vector consisting of all GMM parameters $(\pi_1, \alpha_1, \beta_1, \pi_2, \alpha_2, \beta_2, \dots, \pi_j, \alpha_j, \beta_j)$. Equation (2) is a valid PDF if and only if $\sum_{j=1}^J \pi_j = 1$. The joint distribution of the IID samples is given by:

$$p(X|\Theta) = \prod_{i=1}^N p(x_i|\Theta) \quad (3.10)$$

The Expectation Maximization (EM) algorithm is used as a maximum likelihood estimator for the GMM. EM algorithm maximizes the log likelihood function by introducing some hidden discrete random variables $Z = \{Z_i\}$. If sample x_i belongs to distribution y then $Z_i = y$, where $y \in \mathbb{Z}, 1 \leq y \leq j$. Let $\theta^{(n)}$ be the estimates of the parameters of the GMM for the n^{th} iteration. The first step of EM algorithm calculates the expectation of the log-likelihood $\mathcal{L}(\theta|X, Z)$ as:

$$Q(\theta|\theta^{(n)}, X) = E_{Z|\theta^{(n)}, X} \{\mathcal{L}(\theta|X, Z)\} \quad (3.11)$$

The second step of EM algorithm maximizes the expectation of the likelihood function $\theta^{n+1} = \arg \max_{\theta} (Q)$. The two steps are repeated until the norm of the current and the previous iteration is less than the pre-established threshold or the maximum number of iteration has passed without

the solution converging. The following inequalities give the estimates of GMM parameters for each iteration [51, 58].

$$\hat{\Pi}_j = \frac{1}{N} \sum_{i=1}^N \gamma_{i,j} = \frac{1}{N} \sum_{i=1}^N p(Z_i = j | x_i, \theta^{(n)}) \quad (3.12)$$

where $\gamma_{i,j}$ can be derived by Bayes theorem as

$$\gamma_{i,j} = p(Z_i = j | x_i, \theta^{(n)}) = \frac{p(x_i | \theta_j^{(n)}) p(z_i=j | \theta^{(n)})}{p(x_i | \theta^{(n)})} \quad (3.13)$$

$$\log(\hat{\alpha}_j) - \psi(\hat{\alpha}_j) = \log\left(\frac{\sum_i^N \gamma_{i,j} x_i}{\sum_i^N \gamma_{i,j}}\right) - \frac{\sum_i^N \gamma_{i,j} \log x_i}{\sum_i^N \gamma_{i,j}} \quad (3.14)$$

where $\psi(x)$ is the Digamma function which us defined as $\psi(x) = \frac{\Gamma'(x)}{\Gamma(x)}$

$$\hat{\beta}_j = \frac{1}{\hat{\alpha}_j} \frac{\sum_i^N \gamma_{i,j} x_i}{\sum_i^N \gamma_{i,j}} \quad (3.15)$$

3.3 Implementation of Gamma mixture model

The GMM using EM algorithm was implemented in the following steps:

- 1) Gather IQ data or pixel intensity data.
- 2) Band pass through a Butterworth filter with cut off frequencies of 1MHz and 12MHz.
- 3) Form envelope using Hilbert transform.
- 4) If needed down sample the image to ensure that the intensity values are IID
- 5) First estimate of parameters $\theta^{(0)}$ is obtained by initialization the value of different parameters based on data from fitting one Gamma distribution only. Equal weightage is given to each distribution.
- 6) Increase the iteration number

- 7) Calculate $\gamma_{i,j}$ using equation (6), Calculate $\hat{\alpha}_j$ using equation (7), Calculate $\hat{\beta}_j$ using equation (8), calculate $\hat{\Pi}_j$ using equation (5)
- 8) Continue steps 6 and 7 until $\| \theta^{(n)} - \theta^{(n-1)} \| < \text{threshold limit}$
- 9) Goodness-to-fit of the GMM was also measured by means of Kullback-Leibler divergence (KL) and Kolmogorov-Smirnov statistics (KS).

Gamma distribution parameters are not related to any physical quantity. To study the effect of changing backscatter on the gamma distribution. Simulations were generated to study the effect of alpha and beta. The mean of gamma distribution is given as α/β , whereas the variance is given as $\alpha\beta^2$. The SNR of the Gamma distribution is given as $\sqrt{\alpha}$, but this holds only for one gamma distribution.

Computer simulations were used to obtain sets of RF data with vary scatter size and number density. The simulation parameters try to replicate a clinical transvaginal array transducer used in our previous studies. A Gaussian focused beam with 4 cm focal length, 0.74 mm beam width, 5MHz center frequency, F# 2 and 25% -3dB band width on transmit was used. Attenuation was kept constant at 0.5 dB/cm-MHz but the form factor was changed between spherical shell and Gaussian spherical. The scatter size was varied as 12.5, 25, 50, 75 μm . The scattering number density was varied from 9, 44, 440 mm^{-3} , approximately corresponding to 2, 10, 100 scatterer's per resolution cell respectively.

Gamma distribution was fit to find the corresponding α and β values. The shape parameter α directly relates with the signal to noise ratio (SNR) as $\alpha = \text{SNR}^2$, since β is the scale parameter it should be related to the backscatter intensity levels. To see if the β parameters depends on backscatter intensity levels, the whole simulated data set was normalized with the maximum value and the Gamma parameters calculated. Table 6 shows the SNR and β values for

Spherical shell form factors with varying scatter size and number density .Table 7 shows the SNR and β values for Gaussian spherical form factors with varying scatter size and number density

Table 6: SNR and β values for Spherical shell form factors with varying scatter size and number density

Number of scatterer's per resolution cell (Number density in mm^{-3})			
Size(μm)	2 (9)	10 (44)	100 (440)
12.5	1.47, 1.03E-05	1.6, 6.36E-05	1.59, 6.34E-05
25	1.47, 7.13E-05	1.56, 1.44E-04	1.58, 6.06E-04
50	1.49, 2.88E-04	1.57, 5.86E-04	1.60, 2.38E-03
75	1.53, 1.64E-04	1.57,3.46E-04	1.60,2.43E-03

Table 7: SNR and β values for Gaussian spherical form factors with varying scatter size and number density

Number of scatterer's per resolution cell (Number density in mm^{-3})			
Size(μm)	2 (9)	10 (44)	100 (440)
12.5	1.48, 6.05E-07	1.57, 1.22E-06	1.58, 3.79E-06
25	1.46, 4.58E-06	1.58, 8.80E-06	1.57, 2.84E-05
50	1.48, 2.57E-05	1.57, 5.21E-05	1.60, 1.59E-04
75	1.49, 5.07E-05	1.57, 1.02E-04	1.58, 3.19E-04

For both the tables 6 and 7 the SNR increases with increasing number density but stagnates when the speckle becomes fully developed, α is seen to be independent of scatter size.

When the RF data is normalized with respect to the maximum as seen in Table 8 and table 9. The SNR parameter takes the same values but the value of β parameter increases after normalization.

Hence β is dependent on the pixel intensity of the RF data.

Table 8: SNR and β values for normalized Spherical shell form factors with varying scatter size and number density

Number of scatterer's per resolution cell (Number density in mm^{-3})			
Size(μm)	2 (9)	10 (44)	100 (440)
12.5	1.47, 9.19E-02	1.59, 6.86E-02	1.58, 8.95E-02
25	1.47, 9.01E-02	1.56, 8.01E-02	1.58, 9.37E-02
50	1.49, 7.55E-02	1.57, 8.96E-02	1.60, 8.49E-02
75	1.53, 8.92E-02	1.57, 9.22E-02	1.60, 9.25E-02

Table 9: SNR and β values for normalized Gaussian spherical form factors with varying scatter size and number density

Number of scatterer's per resolution cell (Number density in mm^{-3})			
Size(μm)	2 (9)	10 (44)	100 (440)
12.5	1.48, 9.09E-02	1.56, 8.46E-02	1.58, 9.88E-02
25	1.46, 9.36E-02	1.57, 9.93E-02	1.57, 1.04E-01
50	1.48, 9.61E-02	1.57, 7.76E-02	1.60, 8.42E-02
75	1.49, 8.48E-02	1.57, 8.83E-02	1.59, 8.26E-02

The parameters SNR and β are not specific to back scattering properties like scatter size and number density but can be used to highlight differences in changing backscatter. We wanted to test the hypothesis that if GMM can be used to differentiate between regions of different back

scatterer's hence help in identifying regions of similar back scatter so as to get better estimates of attenuation in cervix.

3.4 Simulation

Two computer simulated three layered images were constructed with varying scatter size and number density. A Gaussian focused beam with 0.74 mm beam width, 5MHz center frequency and 25% -3dB band width on transmit was used. Table 10 summarizes the parameters for the first simulated three layered image. Table 11 summarizes the parameters for the second simulated three layered image.

Table 10: Parameters for 1st simulated layered images

Parameters	Simulated Image 1		
	layer 1	layer 2	layer 3
Size (um)	25	75	12.5
Attenuation (dB/cm-MHz)	0.5	1	0.5
Number density (mm-3)	44	44	44
Focal length (cm)	4	5.6	7.2
F#	2	2	2
Relative Impedance	1	1	1

Table 11: Parameters for 2nd simulated layered images

Parameters	Simulated Image 2		
	layer 1	layer 2	layer 3
Size (um)	25	25	25
Attenuation (dB/cm-MHz)	0.5	1	0.5
Number density (mm-3)	220	220	220
Focal length (cm)	4	5.6	7.2
F#	4	4	4
Relative Impedance	1	10	5

A B-mode image of the first simulated layer is shown in figure 7(a) along with the gamma probability maps in figure 7(b), 7(c), 7(d). The three maps show the probability of each pixel belonging to a particular distribution. The first distribution contains the layer 2. The second distribution mainly contains layer 1 along with some noise from layer 2 and the third distribution contains the layer 3. The SNR values of the three layer are 1.64, 1.60, and 1.25 respectively. The B-mode image for the second simulated layer is shown in figure 8(a) along with the gamma probability maps in figure 8(b), 8(c), 8(d). The three maps show the probability of each pixel belonging to a particular distribution. The first distribution contains the layer 1 along with noise from layer 2. The second distribution mainly contains layer 2 along with some noise from layer 1 and the third distribution contains the layer 3. The SNR values of the three layer are 1.63, 1.62 and 1.27 respectively.

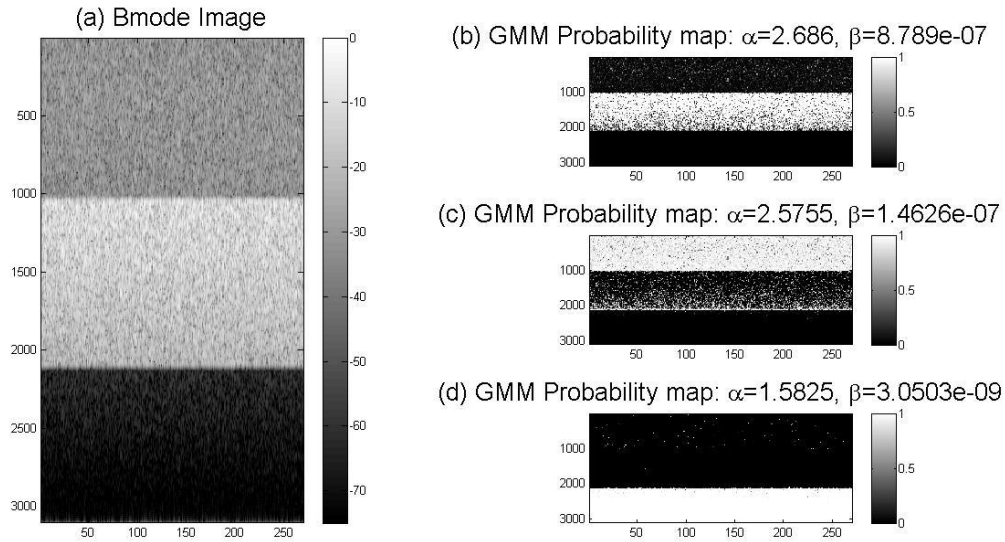


Figure 7: (a) B-mode image of simulated phantom (b) Gamma probability map for 2nd layer (c) Gamma probability map for 1st layer (d) Gamma probability map for 3rd layer

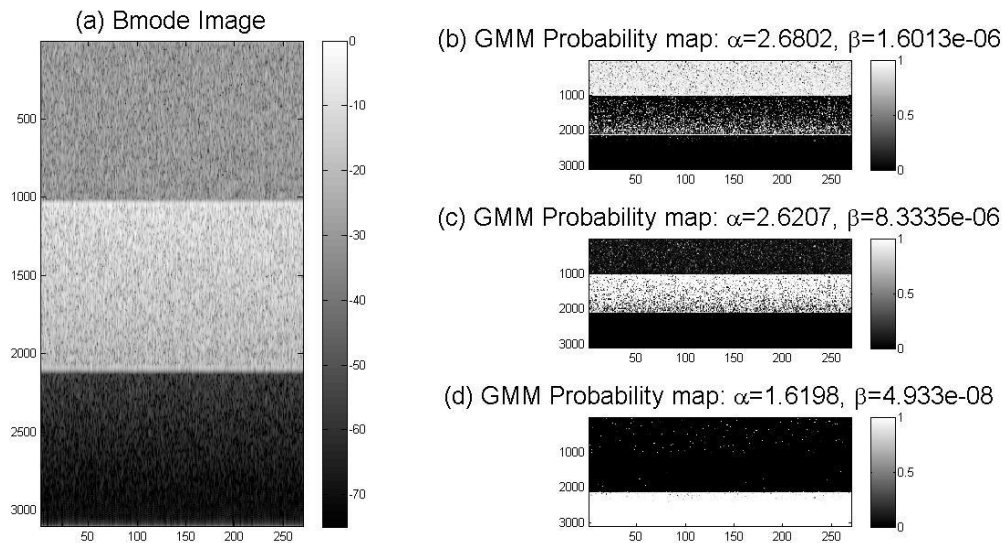


Figure 8: (a) B-mode image of simulated phantom (b) Gamma probability map for 1st layer (c) Gamma probability map for 2nd layer (d) Gamma probability map for 3rd layer

From the above figures it can be concluded that GMM can identify region of varying scattering properties (both scatter size and number density) for simulated images.

3.5 Three layered phantoms

To extend the results from theoretical simulations to real life ultrasound images, two three layered phantom were used [59]. Phantom 1 has constant attenuation whereas phantom 2 has constant backscatter. The size of the scatterer's varies from 5 to 43 μ m. Table 12 summarizes the properties of the phantom 1 (details about phantom construction[59]). Whereas, table 13 summarizes the property of phantom 2.

Table 12: Properties of phantom 1

Constant Attenuation	Phantom 1		
	layer 1	layer 2	layer 3
Layer dist. from transducer(cm)	0-1.5	1.5-3	3-7
Attenuation (dB/cm-MHz)	0.52	0.54	0.52
BSC (1/cm sr.)	0.000091	0.00365	0.00091
Scatterer Conc. (g/l)	2	8	2

GMM was used to differentiate the three layers. In case of phantom 1, GMM was able to differentiate the regions of different backscatter as seen in figure 9. For phantom 2, GMM just gives 1 type of distribution which is correct since there is no change in back scatter as seen in figure 10. To validate the effect of changing back scatter on attenuation, attenuation map for the phantom were generated with GMM and without GMM.

Table 13: Properties of phantom 2

Constant Backscatter	Phantom 2		
	layer 1	layer 2	layer 3
Layer dist. from transducer(cm)	0-1.5	1.5-3	3-7
Attenuation (dB/cm-MHz)	0.48	0.73	0.47
BSC (1/cm sr.)	0.00182	0.00182	0.00182
Scatterer Conc. (g/l)	4	4	4

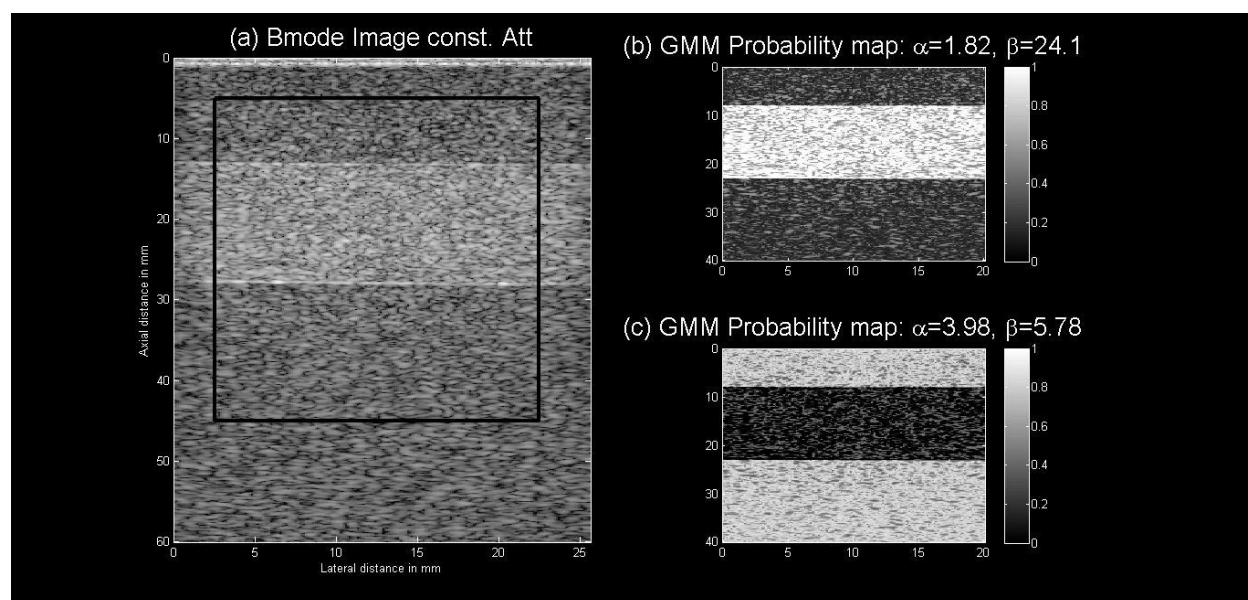


Figure 9: (a) B-mode image of phantom 1 (b) Gamma probability map for 2nd layer (c) Gamma probability map for 1st and 3rd layer

Both Spectral difference and Spectral log difference algorithm were used. 14 pulse length (8.624mm) in the axial direction and 15 echoes (18.98mm) in the lateral direction were chosen as the ROI size. Time gated windows overlapped by 50% and size of the window was 7 pulse

length per window. Threshold value of 0.7 was used for probability. For spectral difference algorithm if the mean value of the probability inside the windowed region was less than the threshold value then the attenuation estimate corresponding to that region was discarded. Whereas for Spectral log difference algorithm if the mean value of probability inside the proximal and distal window was less than the threshold value then the attenuation estimate corresponding to that region was discarded. Figure 11 shows the attenuation map for phantom with constant attenuation using both the algorithms.

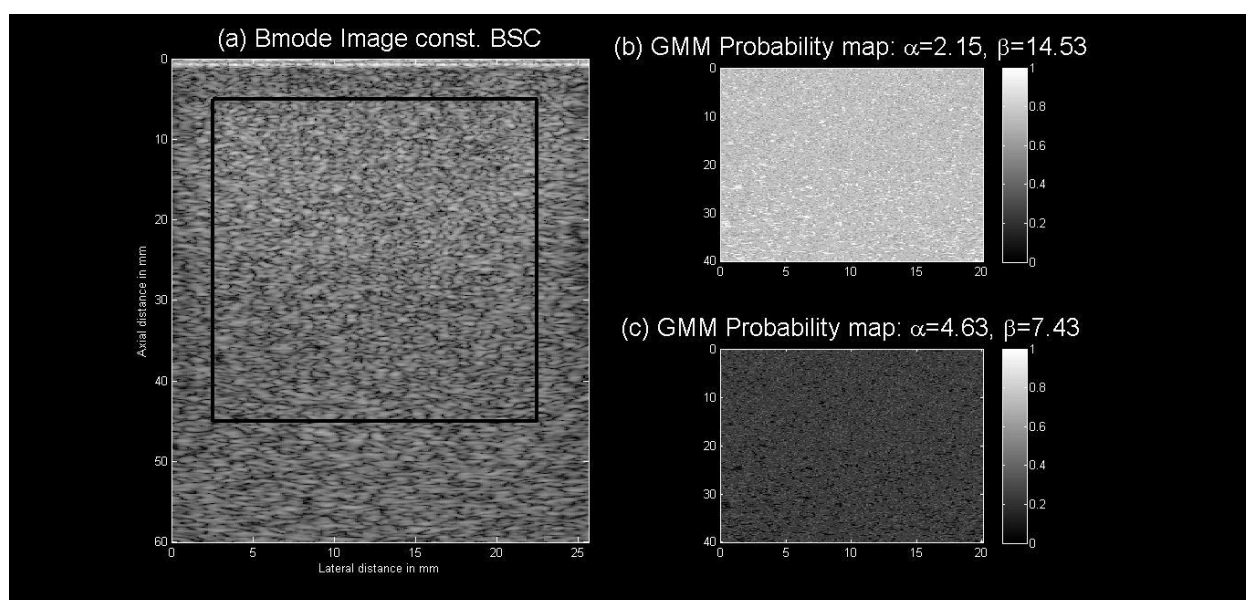


Figure 10: (a) B-mode image of phantom 2 (b) Gamma probability map for all layers (c) noise

For Spectral difference algorithm it can be clearly seen that there is a layer of negative attenuation as we go from layer 1 to layer 2. Similarly there is a layer of very high attenuation as we go from layer 2 to layer 3. Spectral log difference has higher variance in its estimate as compared to Spectral difference but both the algorithms give a mean

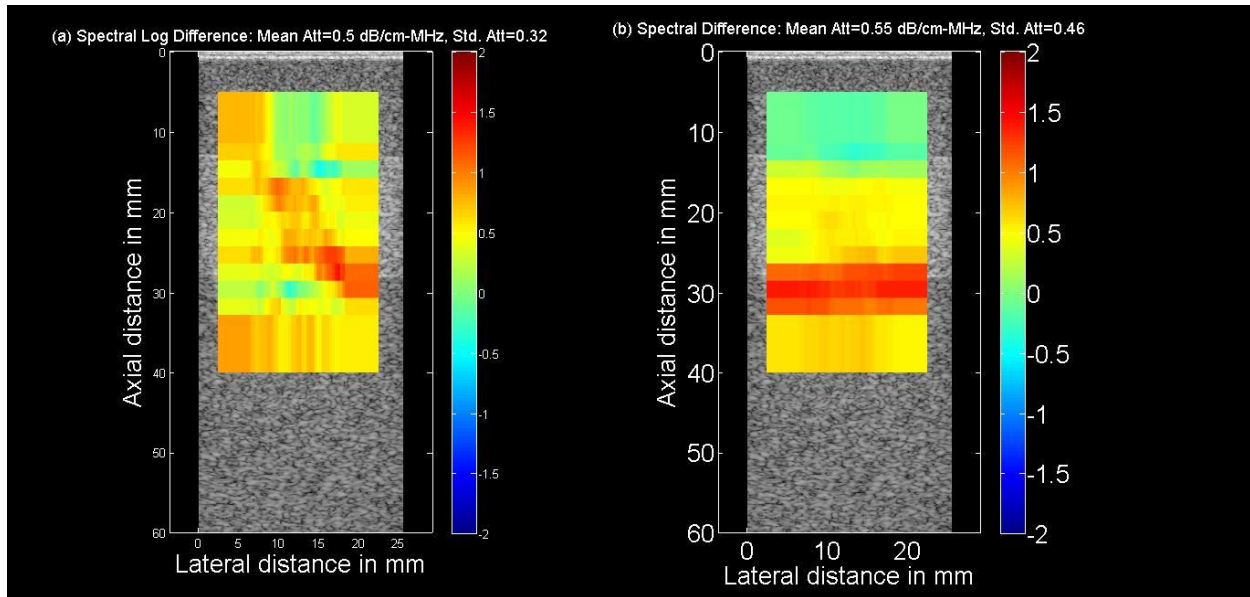


Figure 11: Attenuation map for phantom 1 (a) using Spectral log difference algorithm (b) using Spectral difference algorithm

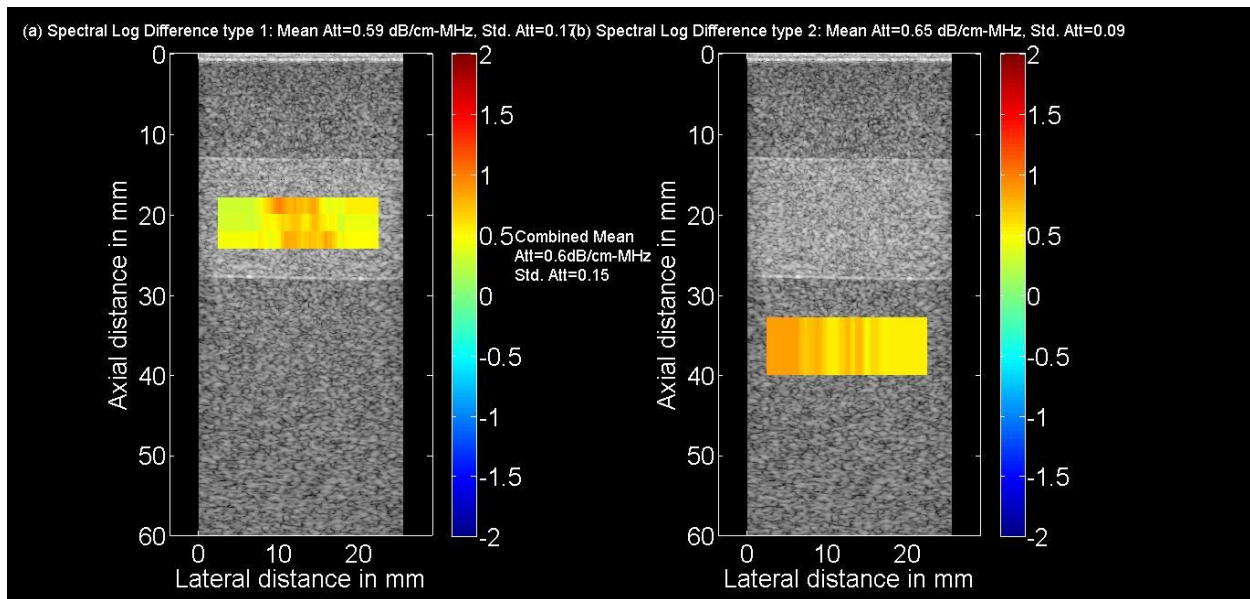


Figure 12: Attenuation map for phantom 1 using GMM and spectral log difference algorithm for (a) middle layer (b) Attenuation map using GMM for top and bottom layer.

value of attenuation close to the actual attenuation value of the phantom. Figure 12 (a), (b) shows the attenuation map for different layers using Spectral Log difference algorithm. Similarly Figure

13(a), (b) show the attenuation map for the two different layers using spectral difference algorithm. The top layers has no estimates because no ROI had a valid attenuation estimate in the top layer due to the thresholding by GMM. It is observed that the mean attenuation estimate for spectral difference algorithm remains constant whereas for Spectral Log difference algorithm the estimate increases. The variance decreases drastically for Spectral difference algorithm but not a major change in variance for Spectral Log Difference algorithm is observed.

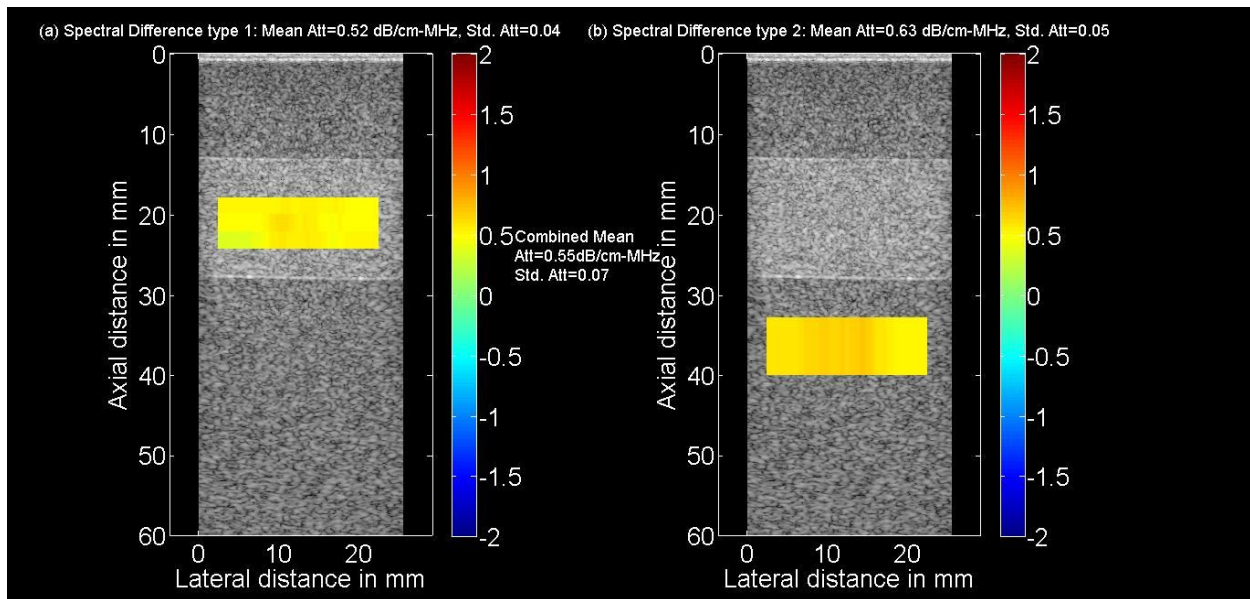


Figure 13: Attenuation map for phantom 1 using GMM and spectral difference algorithm for (a) middle layer (b) Attenuation map using GMM for top and bottom layer.

For phantom 2 there is no change in backscatter, hence only two probability maps are obtained with majority of the data in the first map. Figure 14 shows the attenuation map for the dominant gamma distribution using both the attenuation estimation algorithm.

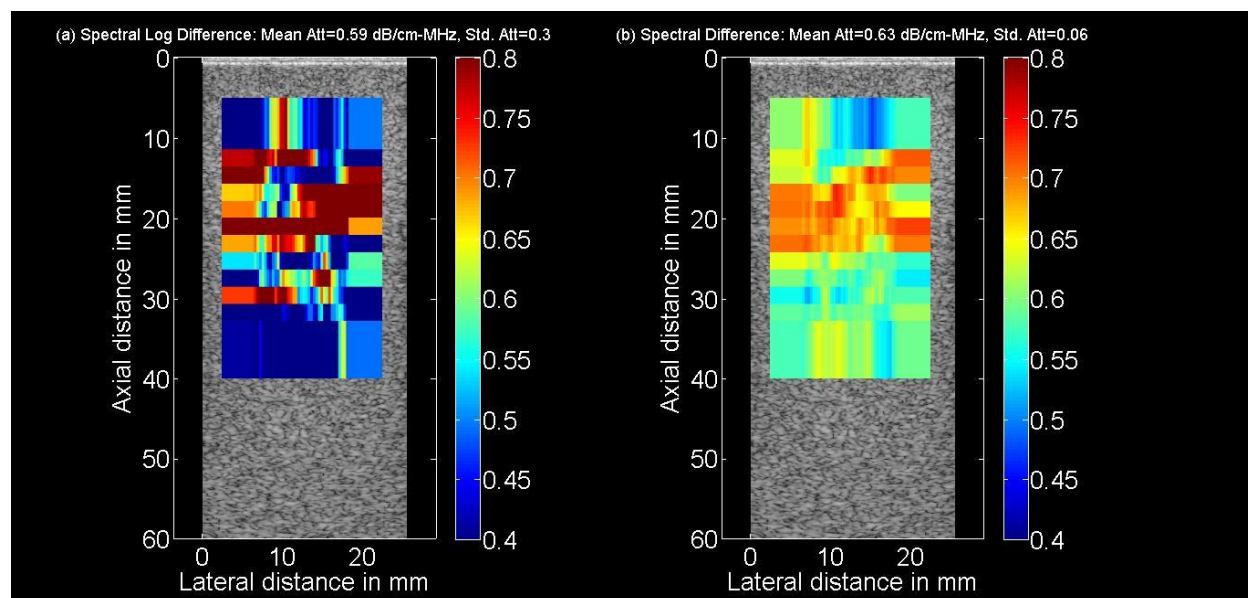


Figure 14: Attenuation map for phantom 2 (a) using Spectral log difference algorithm (b) using Spectral difference algorithm

3.6 Conclusion

From the above study we conclude that the gamma variables are dependent on the B-mode image. The alpha value seems to relate with the signal to noise ratio of the distribution, whereas the beta value corresponds to the image intensity. The SNR value drops whenever there is more noise in the GMM probability map. The gamma PDF gives us an estimate of the SNR and beta values to expect for the different scattering properties. The knowledge of these SNR and beta values can be helpful in initializing the EM algorithm. We also saw that for simulated images, GMM can clearly distinguish between the different scatter size and varying number density. The results were also replicated in real ultrasound images when phantoms are used and we see the effect on attenuation estimate as the scattering properties behind them change. Since the scattering properties in real cases is always changing the attenuation estimates are always

thrown off. Hence Gamma mixture model will prove very essential in finding regions which are homogenous in nature so that the homogeneity assumption behind attenuation estimation algorithms is not violated.

CHAPTER 4

APPLICATION OF GAMMA MIXTURE MODEL ON CERVICAL DATA

4.1 Introduction

Normal pregnancy length varies from 38 to 42 weeks of gestation with any birth prior to 37 weeks considered as preterm. Complications due to preterm related birth are the leading cause of infant mortality worldwide [16] and the second leading cause in the United States [17]. According to Center for Disease control and prevention, 35% of infant death in the United States in 2010 were related to preterm birth. On a global scale 13 million infants are born each year with preterm complications. Out of these 13 million infants, 1 million die each year contributing to 27% of neonatal deaths [18]. Preterm birth can be spontaneous or medically induced due to medical complications involved during the birth. As the human cervix prepares for giving birth it undergoes a process of remodeling in which the collagen present in the three layers of the cervix realigns and more space is created between the collagen fibrils which is then filled with water and enzymes. This realignment of collagen softens the cervix and prepares it for delivery [19]. Currently the most prevalent technique to identify preterm birth is to measure the cervical length, but it has a low positive predictive value as many women with a short cervix still deliver full term [20, 21]. Hence additional non-invasive techniques with better prediction capabilities should be developed to aid in the assessment of preterm birth.

Traditional ultrasound imaging is a noninvasive technique which is used thorough out the pregnancy and provides anatomical visualization of the soft tissue but does not allow changes in the tissue microstructure to be assessed. However, the time domain IQ data available from ultrasound scans can be converted into RF data for estimating quantitative ultrasound parameters

like attenuation, backscatter, scatter size, and acoustic concentration [1-5] which give's insight into the microstructure of the tissue.

For assessing the risk of premature birth, detecting the softening of the cervix as the time of delivery approaches may have the best diagnostic potential as the cervix must soften before dilation. Therefore, measurements of the quantitative ultrasound parameters linked to the softening may enable clinicians to more reliably predict premature delivery. Premature softening of the cervix would place a patient at higher risk for premature delivery especially for a short cervix. Ultrasonic attenuation is a quantitative ultrasound parameter which can also be used to study the changes in the cervix and is sensitive to cervical softening [8, 10] due to its potential sensitivity to cervical softening. Ultrasonic attenuation is defined as the loss of energy as the ultrasonic wave propagates in the tissue medium. Different tissues attenuate the ultrasonic wave to a different extent which can be used to detect changes in the tissue microstructure. As the cervix softens, the collagen concentration decreases and the water content increases [19]. Both of these changes should result in a lower ultrasound attenuation as has been shown in our earlier work. [8-12].

However, in chapter 2 we concluded that cervical length is seen to perform better than attenuation when the area under the receiver operating characteristics (ROC) was calculated. It was also observed that the attenuation values had a very high variance which reduces the diagnostic potential of ultrasound attenuation in the application. This high variance may result from violation of the assumptions of the algorithms used to calculate the attenuation. Specifically, the algorithms assume that the tissue is homogeneous whereas the cervix is a heterogeneous region and the backscatter changes as the ultrasonic wave goes from one tissue type to another. The changes in tissue type would appear as very high and very low attenuation

values relative to the mean depending on how the backscatter changed within a region (i.e., large variances in attenuation estimates). Therefore, to get less variance in the attenuation estimates, the underlying region should have the same backscatter. Thus identifying regions of similar backscatter becomes vital for obtaining valid estimates of attenuation. We hypothesize speckle characteristics could play a crucial role in identifying homogenous regions of tissue.

Speckle is a multiplicative noise which is a very characteristic of ultrasound images. It's a granular pattern observed due to the constructive or destructive interference of scattered ultrasound waves from one resolution cell assuming multiple scatterer's in each cell. Speckle can also provide information of the underlying tissue as it depends on the scattering properties of the tissue. Speckle statistics depends on the size, acoustic concentration and arrangement of the scatterer's. Speckle statistics has been used previously as tissue histological descriptors[44]. Speckle statistics can be broadly classified into four categories. A speckle is called fully developed when the reflected signal is diffused. If the reflected signal is specular in nature, the speckle pattern would be partially developed. A speckle pattern is called fully resolved when the spacing between the scatterer's is greater than 2λ , whereas if the spacing between scatterer's is less than 2λ the speckle pattern is called partially resolved.

Over the decades, different distributions have been proposed to model the first order statistics of the echo envelop. In the ideal case when the speckle is fully developed, the number density of the scatterer's is high and no coherent component is present allowing the Rayleigh distribution to model the echo envelope perfectly[45, 46]. If the coherent component deviates from the Rayleigh distribution and changes to a deterministic component, then Rice distribution is used [47, 48]. Partially developed speckle with low number density of scatterer's and no deterministic component is modeled using K distribution[60]. The parameters of K distribution

relate to physical properties of the scattering medium like the density of scatterer's. Partially resolved speckle with low scatter number density and in the presence of deterministic component is modeled using Homodyned K distribution[49, 50]. Some other important multi parameter distributions are Nakagami distribution (2 parameters) and three parameter distributions like the Rician inverse Gaussian distribution and generalized k- distribution [51-53].

All of the above mentioned distribution work well in theory but fail to different degrees for real life cases of ultrasound images. The acquisition process and the post processing techniques like log compression change the envelope of the RF data and contribute to the failure of these models. The center frequency is also affected by the number density of the scatterer's resulting in deviations from Rayleigh statistics. To resolve these problems, additional distributions have been proposed which give empirically better result but have no relation with the physical properties of the scattering medium. Gamma distribution is a two parameter distribution which gives better empirical results when compared with Rayleigh distribution, K distribution, Nakagami distribution and the inverse Gaussian distribution[54]. Gamma distribution has shown promising results for modeling real ultrasonic data when the speckle is fully developed [54-56]. In the above mentioned work, log compression and filtering were done but no explanation was provided for Gamma distribution being a better model than other available models. A tissue with homogenous scattering properties can be modeled by the distributions mentioned above but when the tissue has heterogeneous scattering properties it's not fair to model it with only one distribution. The varying scattering properties will result in multiple probability distribution functions for the echo envelope. Hence tissues with varying scattering properties should be modeled with mixture models with Gamma mixture model (GMM) having been shown to perform better than the Rayleigh mixture model and the

Nakagami mixture model [57]. Also, in a previous study, we showed that GMM can be used to identify regions of varying scattering properties in simulated images as well as phantoms.

The attenuation estimate is dependent on the scattering property remaining constant throughout the region of interest (ROI). This assumption is often violated by the heterogeneous cervix tissue. In order to obtain better estimates for attenuation we propose to repeat our earlier study (chapter 2) by implementing GMM in the cervix to calculate attenuation for regions having similar backscatter. We hypothesize a better value of area under the ROC curve using the GMM as the impact of tissue heterogeneity will be reduced.

4.2 Materials and method

A study was conducted on sixty three pregnant African-American women, since they have a high rate of preterm birth[38]. The study was approved by the Human Subjects Review Board of the University of Illinois at Chicago. Subjects were inducted into the study only if they met the following criteria's: older than 18 years of age; able to read, write and comprehend English; no immune disorder; not on steroids; don't have diabetes. Women with anomalous fetus or too ill to give consent were omitted from the study. The subjects were expected to undergo five transvaginal ultrasound examinations between planned intervals of 17-39 weeks of gestational age. Some subjects could not attend all the 5 planned exams, hence fewer scans for those subjects were taken. Subjects' data was also not included in the analysis if the birth was medically induced.

Ultrasonic IQ (in-phase quadrature) data was acquired with an E9-4 endovaginal transducer from z.one Zonare ultrasound system (ZONARE Medical Systems, Mountain View, CA). The transducer has a center frequency of 6.8 MHz and a bandwidth of 2.4 MHz, with a

penetration depth of 11.5cm. A preset was used on the ultrasound machine to remove operator bias and to ensure that the machine settings didn't change from one scan to another. The sonographer had the flexibility of choosing the depth of the scan but the depth was to be kept same throughout the scan. The sonographer first scanned the subject with a center frequency of 5 MHz and then immediately scanned a well characterized tissue mimicking phantom using the same preset settings. A custom built Gammex (Gammex Inc., Middleton, WI) tissue mimicking phantom (series 0.5LE) was used as the reference phantom and had a known attenuation of 0.5 dB/cm-MHz as given by the manufacturer and independently verified in our laboratory. The phantom had no occlusions and had a uniform backscatter. The phantom had scattering targets of average scatter diameter of $35\mu\text{m}$ with a number density of 160mm^{-3} . A calibrated reference phantom is required to calculate the attenuation of the cervix so as to cancel the effects of diffraction term and machine transmit/receive characteristics[39]. The date of delivery was also noted for each subject by following up with the patient after the completion of the scans. In addition, the cervical length was measured from the ultrasound images acquired from each scan.

After scanning, the IQ data was stripped of all personal data and was sent to Iowa State University for calculation of attenuation values. The engineer processing the attenuation value was unaware of the gestation age of the scan. For processing, the IQ data was imported into MATLAB (MathWorks Inc., Natick, MA. USA) and was converted to RF (radio frequency) data. The RF data for the whole image was decomposed into multiple regions and the attenuation was calculated for each region resulting in an attenuation image which could be overlaid on the B-mode image. The regions were generated by first applying a series of rectangular windows with 50% overlap in the axial direction so that the changes in the spectrum could be calculated as a function of depth. The size of each window was set at 7 pulse length per window by plotting

the -6dB bandwidth against the number of spatial pulse length and observing the number of pulse lengths at which the -6dB bandwidth becomes constant. The pulse length was calculated by taking the auto correlation coefficient of time samples from RF echo lines of the phantom data. Samples with absolute correlation coefficient greater than 0.2 were considered correlated and determined the time pulse length. The spatial pulse length or simply the pulse length can then be calculated by multiplying time pulse length with the speed of sound and dividing by 2. Our prior studies have shown that expressing resolution in pulse length and number of independent echoes is a relatively independent method for comparing the results from different ultrasound systems and scans [61, 62].

The Fourier transform of each windowed data was then calculated and the spectrogram was plotted to determine the noise level for the particular scan and frequency. An average value of -17 dB bandwidth was used which was at least 5dB above the noise floor. The reference scan was processed in a similar manner. The average spectral value of all the windows in the usable frequency range was then divided by the average reference spectral value to cancel the diffraction term and system effects. An attenuation map of the cervix was then generated by using either the spectral difference algorithm or the spectral log-difference algorithm.

The size of the regions (resolution of the attenuation images) was varied in both the axial and lateral direction by varying the number of time gated windows (axially) and number of independent echoes (laterally). We picked region sizes of 2, 3 and 4 windows axially which corresponded to 10.5, 14, 17.5 pulse length in axial direction (6.468, 8.624, 10.780 mm). In the lateral direction, the regions were varied as 5, 10, 15 and 20 independent echoes (6.32, 12.65, 18.98, 25.31mm), where every third echo was determined to be independent for our ultrasound images. Our previous studies had shown that approximately 15 pulse lengths in the axial

direction and 15 echoes in the lateral direction gave a standard deviation on the order of 25% in the attenuation estimates when the tissue was homogeneous. Therefore, we varied our region sizes about these values for our study [11, 37, 39].

For our study, the attenuation was calculated using the spectral-log difference algorithm as this algorithm has been shown to be less sensitive to tissue heterogeneity than other reference phantom methods. The Spectral log difference algorithm only uses the proximal and distal window of the ROI. The proximal and distal windows would be the window closest to the transducer (proximal) and furthest from the transducer (distal) associated with a specific region. To calculate the attenuation using spectral difference algorithm the power spectrum of a windowed region can be written as

$$S_s(f, z) = P(f)D_s(f, z)A_s(f, z_0)B_s(f, z)e^{-4\alpha_s(f)(z-z_0)} \quad (4.1)$$

where subscript s represents the sample, f is the frequency, z is the distance from surface of the transducer to the center of time gated window within the ROI, z_0 is the start of the ROI, P is the electro-acoustic and acousto-electric transfer functions, D is the diffraction term, A is the cumulative attenuation along the path of propagation, B is the backscatter term, α is the attenuation coefficient of the ROI. Similarly the power spectrum for the reference phantom can be written as S_r . The diffraction terms can be removed from the above equations by assuming that the speed of sound is approximately the same in the tissue and tissue mimicking phantom. If the tissue within an ROI is assumed to be homogenous and isotropic then the scattering term does not depend on the depth. Dividing the two spectra and taking natural logarithm gives us equation (4.2)

$$\ln \left[\frac{S_s(f, z)}{S_r(f, z)} \right] = R(f, z) = 4(z - z_0)(\alpha_r(f) - \alpha_s(f)) + \ln \left[\frac{A_s(f, z_0)B_s(f)}{A_r(f, z_0)B_r(f)} \right] \quad (4.2)$$

We can rewrite equation (4.2) for the proximal and distal window with respect to the phantom separately. Now subtract the proximal and distal window power spectrum ratios, this gives us equation (4.3)

$$SS(f) = \ln \left[\frac{S_s(f, z_p)}{S_r(f, z_p)} \right] - \ln \left[\frac{S_s(f, z_d)}{S_r(f, z_d)} \right] = 4(z_p - z_d)(\alpha_r(f) - \alpha_s(f)) + \ln \left[\frac{A_s(f, z_0)B_s(f, z_p)}{A_r(f, z_0)B_r(f, z_p)} \right] - \ln \left[\frac{A_s(f, z_0)B_s(f, z_d)}{A_r(f, z_0)B_r(f, z_d)} \right] \quad (4.3)$$

Since the phantom is homogenous and isotropic the back scattering term for the proximal and distal window for the reference is same. Also, if the effective scatter size of the proximal and distal window is the same we can assume that backscatter of proximal and distal windows for the tissue are different only by a multiplicative constant. So now the equation becomes

$$SS(f) = 4(\alpha_r(f) - \alpha_s(f))(z_p - z_d) + constant \quad (4.4)$$

After replacing α and assuming that attenuation increases linearly with frequency. The slope of the line fitting the substituted equation (4.4) will give us attenuation estimate for the corresponding region as shown in equation (4.5).

$$\beta_s f = \alpha_r(f) - \frac{SS(f) - constant}{4(z_p - z_d)} \quad (4.5)$$

4.3 Results

In addition to calculating the attenuation values, the cervical region was manually extracted and passed through a GMM to obtain probability maps corresponding to the different tissue types. When using the GMM to classify tissue regions, having the correct number of mixtures is critical. Ideally, the number of mixtures would be known a priori, but this is not the case for the heterogeneous cervix. Therefore, the log likelihood was calculated for different

number of mixtures [63]. Figure 15 shows the log likelihood for two different scans as the number of mixtures is increased. The log likelihood does not increase much after the number of components reaches four. Hence four was considered the ideal number of gamma distributions required to model the cervix. The GMM was then implemented using the EM algorithm as described in Chapter 3.

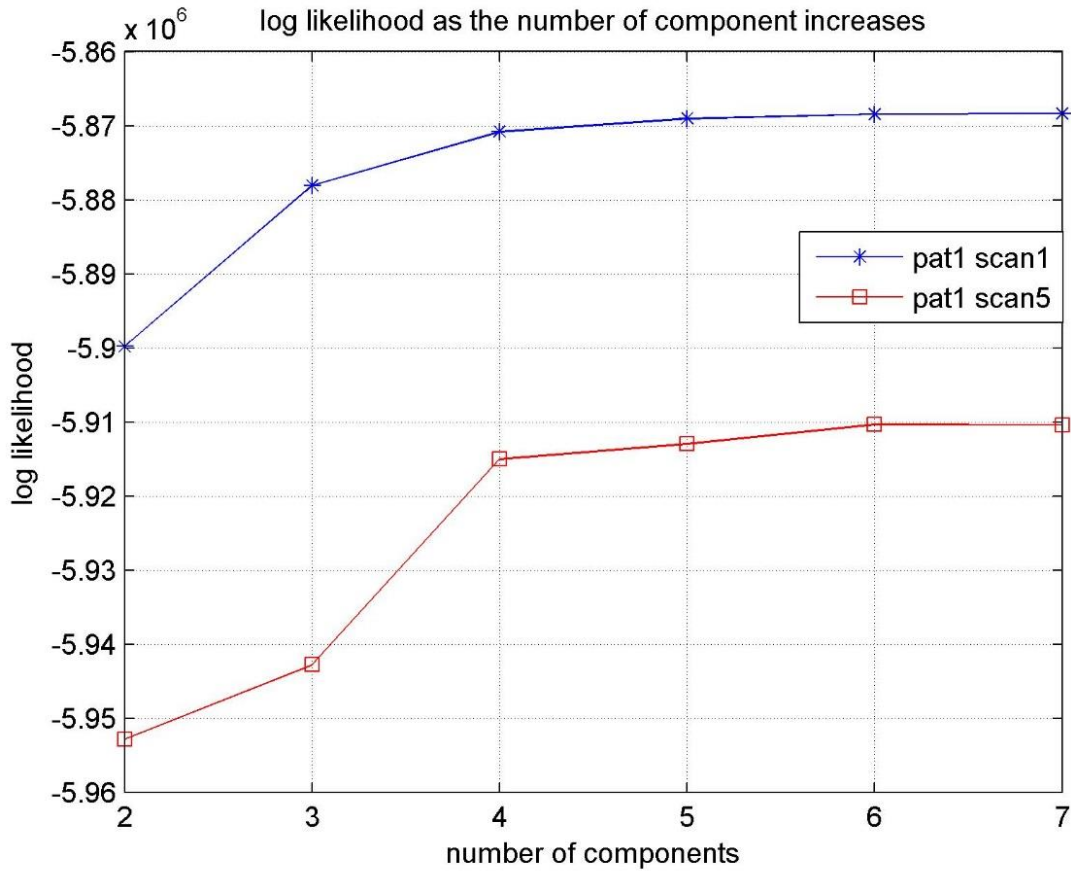


Figure 15: Log likelihood versus number of components for the whole image

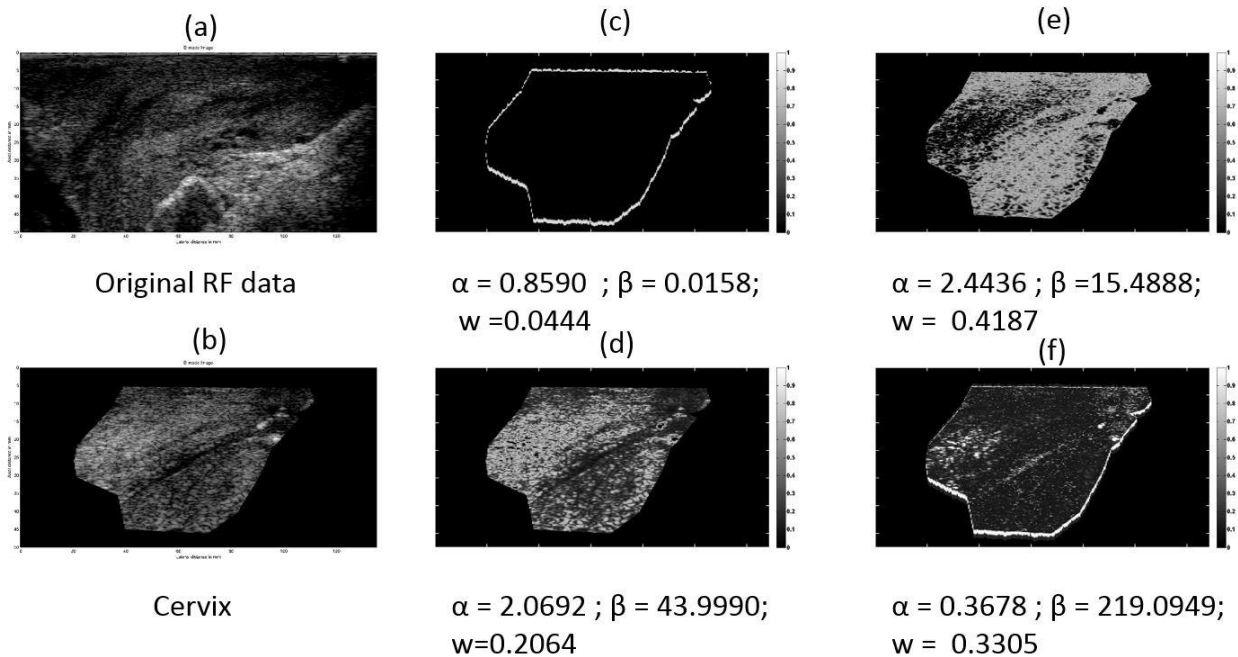


Figure 16: (a) Original RF data (b) segmented cervical region (c) first probability maps with edge effect dominating (d) second probability map with one of the major scattering type (e) third probability map with another important scattering type (f) fourth probability map with edge effects and noise.

Figure 16 (a) shows the original RF data of the ultrasound scan. Figure 16 (b) shows the cervical region after being segmented out of the RF data. Figure 16(c), (d), (e), (f) shows the four probability maps obtained from GMM. Each pixel in these maps represents the probability of that pixel belonging to the particular distribution. Most of the probability points are concentrated in just image 2 (figure 16(d)) and image 3 (figure 16(e)). Image 1 (figure 16(c)) is just an edge effect obtained due to the segmentation process, whereas image 4 (figure 16(f)) looks like a combination of edge effect and noise. The presence of edge effect can be explained by the fact that Hilbert transform was taken after manually segmenting out the cervix. Since Hilbert transform takes the envelope of the data, hence any abrupt changes in the envelope would be seen as an edge effect.

After calculating the attenuation estimates for the cervix, the probability maps were used to eliminate erroneous attenuation estimates from each cervical image. Specifically, if the average probability value for the proximal and distal windows was greater than a threshold value of 0.7, then the windows were assumed to be from the same tissue type and the attenuation estimate was considered valid for that Gamma mixture. Otherwise, the attenuation estimate was discarded and not included in estimating an average attenuation for that patient scan for that mixture. The selected value of 0.7 was based on attempting to balance between being sufficiently restrictive while not eliminating most of the data. However, future studies should evaluate the impact of this threshold on the results in more detail.

Once the attenuation values for each scan and each mixture had been determined, the data was condensed into a single attenuation estimate for each patient scan. This was done by defining a valid range of SNR and beta parameters based on our previous simulation results. Figure 17 plots the data from all the probability maps obtained for each patient and scan. The scaling parameter β and the SNR are represented on the y and x axis respectively of the plot as these two parameters are the most essential in determining the nature of the scatterer. In chapter 3 we saw that the gamma shape parameter α was related with SNR of the distribution as $\alpha = \text{SNR}^2$. Whereas the scale parameter β was related with the pixel intensity of the RF image. The blue, green, red, and black markers represent the first, second, third and fourth image after being sorted in an increasing order of beta. Based on the changes in value of SNR in table 7 we decided to consider only those images who had a SNR value in the range of 1.25 to 1.65. The beta value was restricted from 10 to 100 based on the assumption that similar tissue type should have similar RF intensity values. If two probability maps for a single patient scan were collected using the above technique, a weighted estimate of the attenuation was calculated.

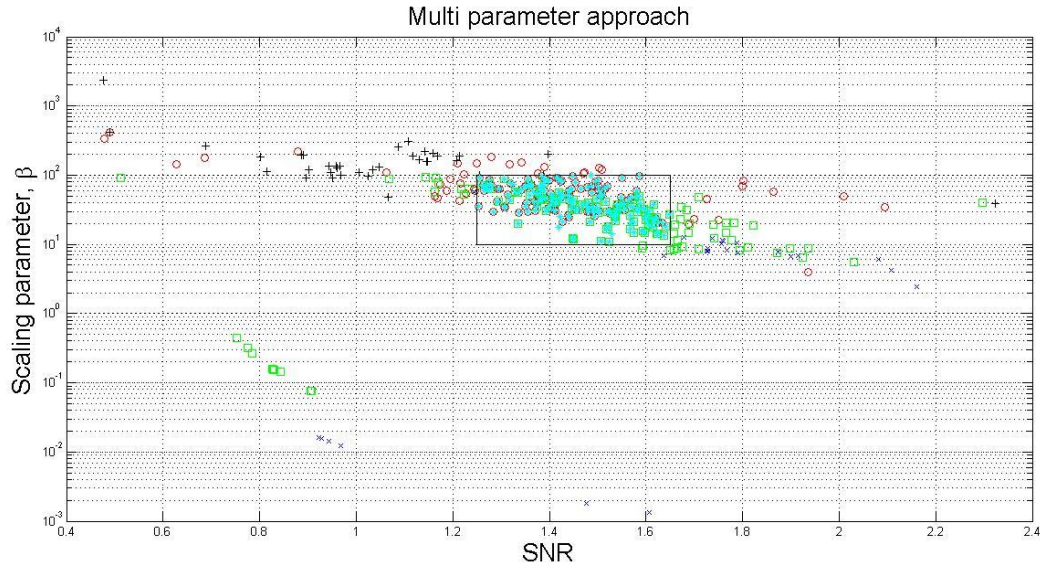


Figure 17: Multi parameter approach showing all the probability maps plotted against SNR on x axis and beta on y axis

Figures 92 to 103 in appendix B show the scatter plots for Attenuation vs Time to Delivery. The average values of attenuation are plotted after dividing the data into 3 groups: 0 to 5 weeks, 5 to 10 weeks and 10 to 15 weeks. The data is plotted at the midpoints of these regions. A best fit trend line for full term data is also added to better visualize the trends. An example is shown in figure 18.

At both 7.5 and 2.5 weeks, there is a decrease in attenuation as we approach closer to the time to delivery. To observe the data quantitatively the receiver operating characteristic were plotted again and their area observed. Figure 104 to 115 in appendix B shows the ROC curve for different pulse lengths and echoes. The maximum area under the ROC curve for multi parameter approach was found to be 0.80 for 10.5 pulse length and 10 echoes as seen in figure 19.

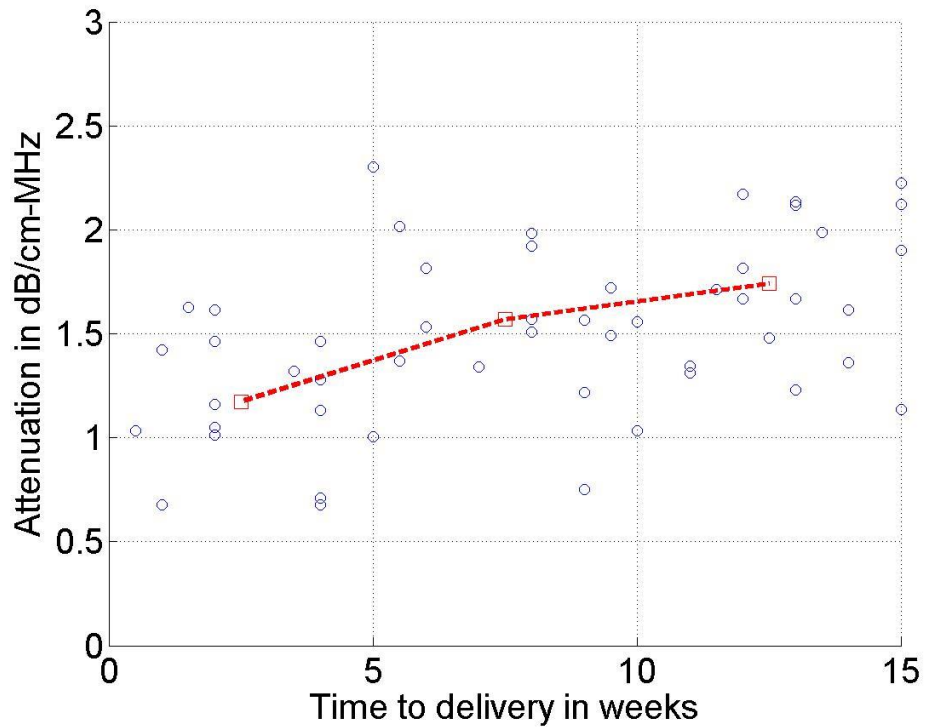


Figure 18: Attenuation vs time to delivery for pulse length of 10.5 and 10 independent echoes

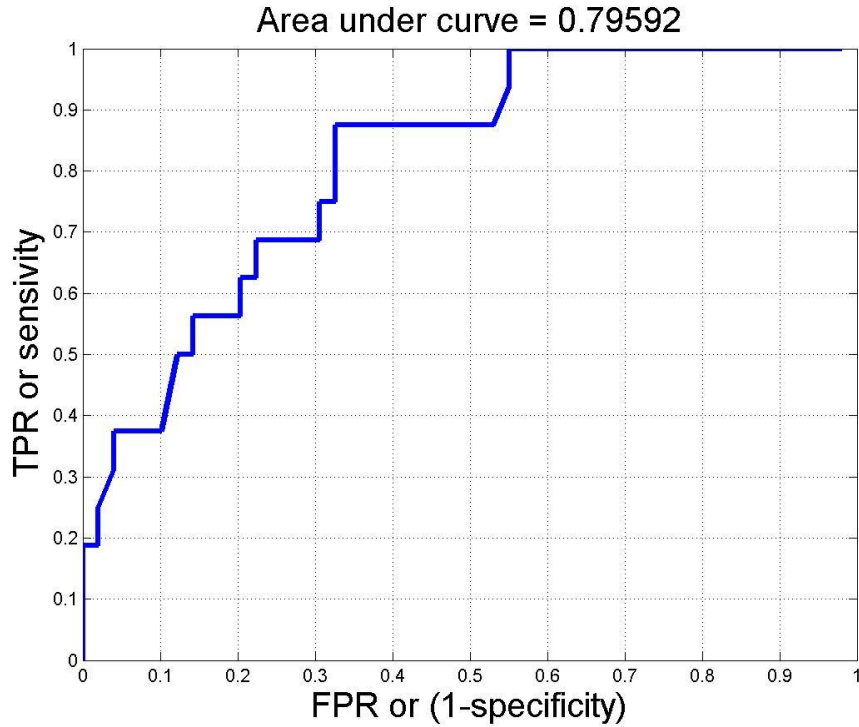


Figure 19: ROC curve for pulse length of 10.5 and 10 independent echoes

4.4 Conclusion

In this chapter, we discussed the ways in which gamma mixture model can be implemented for in human cervix. During our trial and error process we realized that segmenting the cervix from the whole image before calculating the GMM probability maps give us much higher predictive value than using the whole image. A threshold value of 0.8 can be very restrictive but 0.7 seems to be the optimal compromise between the number of points and yet being high enough for the tissue to be considered homogenous. The SNR and beta parameters of the gamma mixture model can be used to select the right probability maps obtained from the GMM. Compared to the original study done in chapter 2, the improvements using GMM are clearly visible with ROC area value increasing from 0.56 to 0.80 and becoming even higher than the value of the ROC for cervical length (0.71). We have also shown that spectral log difference is a better method to use as long as the assumption of tissue homogeneity is violated. In future lot of filters can be developed using gamma probability maps, thresholding is just one solution to the problems and some filters might work better than others. The ROI which gave the highest area under the ROC is 10.5 echoes and 10 pulse lengths and should be used in future to calculate attenuation estimates when using the Spectral log difference algorithm.

CHAPTER 5

SUMMARY AND CONCLUSION

5.1 Conclusion

Ultrasonic attenuation is a quantitative ultrasound parameter which can be used to detect the changes in the tissue microstructure. Softer tissue have lower attenuation compared to harder tissues. As the cervix prepares for delivery the collagen inside the cervix realigns filling the cervix with water and enzyme thus softening the cervix. The cervix softens mainly between first trimester and second trimester but some changes in the stiffness of the cervix also take place between second trimester and third trimester. In order to detect these changes in human's, cervical attenuation can be deployed as a bio predictor in parallel with cervical length. In Chapter 2 we introduced the original study conducted on humans. The variation of ROI size and the different attenuation estimating algorithms were studied. Spectral log difference algorithm seems to be the better choice as it followed the biological trend expected from attenuation, whereas spectral difference algorithm completely fails as it goes in the opposite direction. Both the attenuation estimation algorithms perform poorly and cannot match the performance of cervical length. But when combined with cervical length, their product give a higher predictive value. Thus the authors suggest that cervical length should be used in combination with cervical length for best results.

Since the attenuation algorithms have very high variance, the attenuation estimates from chapter 2 are not very conclusive in predicting time to delivery. The attenuation algorithms assume that the tissue region is homogenous and the violation of this assumption can throw off the

attenuation estimates. Thus a technique is required to find homogenous region inside the cervix. Different PDF's can be used to model ultrasonic data, but gamma PDF has the best empirical fit although it lacks physical significance. Gamma mixture model can be implemented using expectation maximization algorithm. Gamma mixture model parameters alpha and beta seem to correspond to the signal to noise ratio and intensity of the back scattered waves respectively. GMM can also be used to distinguish regions of different scatter size and scatter number density. Since attenuation estimation is dependent on the underlying back scattering, identifying regions of similar back scatter can help in improving the attenuation estimates.

In chapter 4 we optimize the process of calculating attenuation estimate using Gamma mixture model. A threshold value of 0.7 is found to be the most optimal and the ROI size of 10.5 pulse length and 10 echoes should be used as it corresponds to highest ROC curve area. The cervix should be segmented from the image before processing for probability maps. The SNR and beta values of Gamma mixture model can be used as a selection criteria for the probability maps. Using Gamma mixture model ultrasonic attenuation can get higher predictive value than cervical length. In the future different filters can be implemented using Gamma mixture model to get even higher predictive values. The identification of regions of different backscatter can also be used for tissue characterization. A computer could also be trained to use gamma mixture model classifiers, thus teaching it to identify regions of different backscattering.

An attempt to see the difference between attenuation estimates with and without GMM was done on a per patient basis. Due to the insufficient number of points for attenuation estimates with GMM the study was inconclusive. Figure 116 to 180 show the attenuation estimates with and without GMM on per patient basis.

REFERENCES

- [1] Z. Vered, G. Mohr, B. Barzilai, C. J. Gessler, S. A. Wickline, K. A. Wear, *et al.*, "Ultrasound integrated backscatter tissue characterization of remote myocardial infarction in human subjects," *Journal of the American College of Cardiology*, vol. 13, pp. 84-91, 1989.
- [2] K. A. Wear, T. A. Stiles, G. R. Frank, E. L. Madsen, F. Cheng, E. J. Feleppa, *et al.*, "Interlaboratory comparison of ultrasonic backscatter coefficient measurements from 2 to 9 MHz," *Journal of ultrasound in medicine*, vol. 24, pp. 1235-1250, 2005.
- [3] M. F. Insana, R. F. Wagner, D. G. Brown, and T. J. Hall, "Describing small-scale structure in random media using pulse-echo ultrasound," *The Journal of the Acoustical Society of America*, vol. 87, pp. 179-192, 1990.
- [4] T. J. Hall, M. F. Insana, L. A. Harrison, and G. G. Cox, "Ultrasonic measurement of glomerular diameters in normal adult humans," *Ultrasound in medicine & biology*, vol. 22, pp. 987-997, 1996.
- [5] W. Liu, J. Zagzebski, T. Varghese, A. Gerig, and T. Hall, "Spectral and scatterer-size correlation during angular compounding: Simulations and experimental studies," *Ultrasonic imaging*, vol. 28, pp. 230-244, 2006.
- [6] S. Goss, R. Johnston, and F. Dunn, "Comprehensive compilation of empirical ultrasonic properties of mammalian tissues," *The Journal of the Acoustical Society of America*, vol. 64, pp. 423-457, 1978.
- [7] S. Badir, E. Mazza, R. Zimmermann, and M. Bajka, "Cervical softening occurs early in pregnancy: characterization of cervical stiffness in 100 healthy women using the aspiration technique," *Prenatal diagnosis*, vol. 33, pp. 737-741, 2013.
- [8] B. L. McFarlin, W. D. O'Brien, M. L. Oelze, J. F. Zachary, and R. C. White-Traut, "Quantitative ultrasound assessment of the rat cervix," *Journal of ultrasound in medicine*, vol. 25, pp. 1031-1040, 2006.
- [9] T. A. Bigelow, B. L. McFarlin, W. D. O'Brien Jr, and M. L. Oelze, "In vivo ultrasonic attenuation slope estimates for detecting cervical ripening in rats: Preliminary results," *The Journal of the Acoustical Society of America*, vol. 123, pp. 1794-1800, 2008.
- [10] B. McFarlin, T. Bigelow, Y. Laybed, W. O'Brien, M. Oelze, and J. Abramowicz, "Ultrasonic attenuation estimation of the pregnant cervix: a preliminary report," *Ultrasound in Obstetrics & Gynecology*, vol. 36, pp. 218-225, 2010.
- [11] T. A. Bigelow, Y. Labyed, B. L. McFarlin, E. Sen-Gupta, and W. D. O'Brien, "Comparison of algorithms for estimating ultrasound attenuation when predicting cervical remodeling in a rat model," in *Biomedical Imaging: From Nano to Macro, 2011 IEEE International Symposium on*, 2011, pp. 883-886.

- [12] V. Kumar, T. Bigelow, and B. McFarlin, "Cervical attenuation as a measure of preterm delivery: Impact of different region of interest sizes," in *Engineering in Medicine and Biology Society (EMBC), 2014 36th Annual International Conference of the IEEE, 2014*, pp. 234-237.
- [13] L. C. Carlson, H. Feltovich, M. L. Palmeri, J. J. Dahl, A. Munoz Del Rio, and T. Hall, "Estimation of shear wave speed in the human uterine cervix," *Ultrasound in Obstetrics & Gynecology*, vol. 43, pp. 452-458, 2014.
- [14] L. C. Carlson, S. T. Romero, M. L. Palmeri, A. Muñoz del Rio, S. M. Esplin, V. M. Rotemberg, *et al.*, "Changes in Shear Wave Speed Pre and Post Induction of Labor: a Feasibility Study," *Ultrasound in Obstetrics & Gynecology*, 2014.
- [15] M. L. Palmeri, H. Feltovich, A. D. Homyk, L. C. Carlson, and T. J. Hall, "Evaluating the feasibility of acoustic radiation force impulse shear wave elasticity imaging of the uterine cervix with an intracavity array: a simulation study," *Ultrasonics, Ferroelectrics and Frequency Control, IEEE Transactions on*, vol. 60, 2013.
- [16] J. E. Lawn, M. G. Gravett, T. M. Nunes, C. E. Rubens, and C. Stanton, "Global report on preterm birth and stillbirth (1 of 7): definitions, description of the burden and opportunities to improve data," *BMC pregnancy and childbirth*, vol. 10, p. S1, 2010.
- [17] J. A. Martin, S. Kirmeyer, M. Osterman, and R. A. Shepherd, "Born a bit too early: recent trends in late preterm births," *NCHS data brief*, pp. 1-8, 2009.
- [18] L. Liu, H. L. Johnson, S. Cousens, J. Perin, S. Scott, J. E. Lawn, *et al.*, "Global, regional, and national causes of child mortality: an updated systematic analysis for 2010 with time trends since 2000," *The Lancet*, vol. 379, pp. 2151-2161, 2012.
- [19] P. C. Leppert, R. Kokenyesi, C. A. Klemenich, and J. Fisher, "Further evidence of a decorin-collagen interaction in the disruption of cervical collagen fibers during rat gestation," *American journal of obstetrics and gynecology*, vol. 182, pp. 805-812, 2000.
- [20] R. Romero, L. Yeo, J. Miranda, S. S. Hassan, A. Conde-Agudelo, and T. Chaiworapongsa, "A blueprint for the prevention of preterm birth: vaginal progesterone in women with a short cervix," *Journal of perinatal medicine*, vol. 41, pp. 27-44, 2013.
- [21] V. Berghella, J. K. Baxter, and N. W. Hendrix, "Cervical assessment by ultrasound for preventing preterm delivery," *Cochrane Database Syst Rev*, vol. 3, 2009.
- [22] J. D. Iams, "Prevention of Preterm Parturition," *New England Journal of Medicine*, vol. 370, pp. 254-261, 2014.
- [23] S. L. Baldwin, M. Yang, K. R. Marutyan, K. D. Wallace, M. R. Holland, and J. G. Miller, "Ultrasonic detection of the anisotropy of protein cross linking in myocardium at diagnostic frequencies," *Ultrasonics, Ferroelectrics and Frequency Control, IEEE Transactions on*, vol. 54, pp. 1360-1369, 2007.

- [24] C. S. Hall, C. T. Nguyen, M. J. Scott, G. M. Lanza, and S. A. Wickline, "Delineation of the extracellular determinants of ultrasonic scattering from elastic arteries," *Ultrasound in medicine & biology*, vol. 26, pp. 613-620, 2000.
- [25] J. Pohlhammer and W. O'Brien Jr, "Dependence of the ultrasonic scatter coefficient on collagen concentration in mammalian tissues," *The Journal of the Acoustical Society of America*, vol. 69, pp. 283-285, 1981.
- [26] P. He and J. Greenleaf, "Attenuation estimation on phantoms—A stability test," *Ultrasonic imaging*, vol. 8, pp. 1-10, 1986.
- [27] H. S. Jang, T. K. Song, and S. B. Park, "Ultrasound attenuation estimation in soft tissue using the entropy difference of pulsed echoes between two adjacent envelope segments," *Ultrasonic imaging*, vol. 10, pp. 248-264, 1988.
- [28] R. Kuc and H. Li, "Reduced-order autoregressive modeling for center-frequency estimation," *Ultrasonic imaging*, vol. 7, pp. 244-251, 1985.
- [29] M. Fink, F. Hottier, and J. Cardoso, "Ultrasonic signal processing for in vivo attenuation measurement: short time Fourier analysis," *Ultrasonic Imaging*, vol. 5, pp. 117-135, 1983.
- [30] T. A. Bigelow and W. D. O'Brien Jr, "Impact of local attenuation approximations when estimating correlation length from backscattered ultrasound echoes," *The Journal of the Acoustical Society of America*, vol. 120, pp. 546-553, 2006.
- [31] L. X. Yao, J. A. Zagzebski, and E. L. Madsen, "Backscatter coefficient measurements using a reference phantom to extract depth-dependent instrumentation factors," *Ultrasonic Imaging*, vol. 12, pp. 58-70, 1990.
- [32] K. J. Parker, R. M. Lerner, and R. C. Waag, "Comparison of techniques for in vivo attenuation measurements," *Biomedical Engineering, IEEE Transactions on*, vol. 35, pp. 1064-1068, 1988.
- [33] K. J. Parker and R. C. Waag, "Measurement of ultrasonic attenuation within regions selected from B-scan images," *Biomedical Engineering, IEEE Transactions on*, pp. 431-437, 1983.
- [34] R. Kuc, "Estimating acoustic attenuation from reflected ultrasound signals: comparison of spectral-shift and spectral-difference approaches," *Acoustics, Speech and Signal Processing, IEEE Transactions on*, vol. 32, pp. 1-6, 1984.
- [35] R. Kuc and M. Schwartz, "Estimating the acoustic attenuation coefficient slope for liver from reflected ultrasound signals," *Sonics and Ultrasonics, IEEE Transactions on*, vol. 26, pp. 353-361, 1979.
- [36] H. Kim and T. Varghese, "Hybrid Spectral Domain Method for Attenuation Slope Estimation," *Ultrasound in Medicine & Biology*, vol. 34, pp. 1808-1819, 2008.

- [37] Y. Labyed, T. A. Bigelow, and B. L. McFarlin, "Estimate of the attenuation coefficient using a clinical array transducer for the detection of cervical ripening in human pregnancy," *Ultrasonics*, vol. 51, pp. 34-39, 2011.
- [38] J. A. Martin, B. E. Hamilton, S. J. Ventura, M. J. Osterman, and T. Mathews, "Births: final data for 2011," *National Vital Statistics Report*, vol. 62, pp. 1-90, 2013.
- [39] Y. Labyed and T. A. Bigelow, "A theoretical comparison of attenuation measurement techniques from backscattered ultrasound echoes," *The Journal of the Acoustical Society of America*, vol. 129, pp. 2316-2324, 2011.
- [40] H. Jongen, J. Thijssen, M. Van den Aarssen, and W. Verhoef, "A general model for the absorption of ultrasound by biological tissues and experimental verification," *The Journal of the Acoustical Society of America*, vol. 79, pp. 535-540, 1986.
- [41] R. M. Aspden, "Collagen organisation in the cervix and its relation to mechanical function," *Collagen and related research*, vol. 8, pp. 103-112, 1988.
- [42] T. Lau, H. Sangha, E. Chien, B. McFarlin, A. Wagoner Johnson, and K. Toussaint, "Application of Fourier transform-second-harmonic generation imaging to the rat cervix," *Journal of microscopy*, vol. 251, pp. 77-83, 2013.
- [43] V. Berghella, "Novel developments on cervical length screening and progesterone for preventing preterm birth," *BJOG: An International Journal of Obstetrics & Gynaecology*, vol. 116, pp. 182-187, 2009.
- [44] J. M. Thijssen, "Ultrasonic speckle formation, analysis and processing applied to tissue characterization," *Pattern Recognition Letters*, vol. 24, pp. 659-675, 2003.
- [45] R. F. Wagner, S. W. Smith, J. M. Sandrik, and H. Lopez, "Statistics of speckle in ultrasound B-scans," *Sonics and Ultrasonics, IEEE Transactions on*, vol. 30, pp. 156-163, 1983.
- [46] C. B. Burckhardt, "Speckle in ultrasound B-mode scans," *Sonics and Ultrasonics, IEEE Transactions on*, vol. 25, pp. 1-6, 1978.
- [47] T. Tuthill, R. Sperry, and K. Parker, "Deviations from Rayleigh statistics in ultrasonic speckle," *Ultrasonic imaging*, vol. 10, pp. 81-89, 1988.
- [48] M. F. Insana, R. F. Wagner, B. S. Garra, D. G. Brown, and T. H. Shawker, "Analysis of ultrasound image texture via generalized Rician statistics," *Optical Engineering*, vol. 25, pp. 256743-256743, 1986.
- [49] V. Dutt and J. F. Greenleaf, "Ultrasound echo envelope analysis using a homodyned K distribution signal model," *Ultrasonic Imaging*, vol. 16, pp. 265-287, 1994.
- [50] E. Jakeman and R. Tough, "Generalized K distribution: a statistical model for weak scattering," *JOSA A*, vol. 4, pp. 1764-1772, 1987.

- [51] F. Destrempes, J. Meunier, M.-F. Giroux, G. Soulez, and G. Cloutier, "Segmentation of plaques in sequences of ultrasonic B-mode images of carotid arteries based on motion estimation and a Bayesian model," *Biomedical Engineering, IEEE Transactions on*, vol. 58, pp. 2202-2211, 2011.
- [52] P. Mohana Shankar, "A general statistical model for ultrasonic backscattering from tissues," *Ultrasonics, Ferroelectrics, and Frequency Control, IEEE Transactions on*, vol. 47, pp. 727-736, 2000.
- [53] F. Destrempes and G. Cloutier, "A critical review and uniformized representation of statistical distributions modeling the ultrasound echo envelope," *Ultrasound in medicine & biology*, vol. 36, pp. 1037-1051, 2010.
- [54] M. M. Nillesen, R. G. Lopata, I. H. Gerrits, L. Kapusta, J. M. Thijssen, and C. L. de Korte, "Modeling envelope statistics of blood and myocardium for segmentation of echocardiographic images," *Ultrasound in medicine & biology*, vol. 34, pp. 674-680, 2008.
- [55] T. Eltoft, "Modeling the amplitude statistics of ultrasonic images," *Medical Imaging, IEEE Transactions on*, vol. 25, pp. 229-240, 2006.
- [56] Z. Tao, H. D. Tagare, and J. D. Beaty, "Evaluation of four probability distribution models for speckle in clinical cardiac ultrasound images," *Medical Imaging, IEEE Transactions on*, vol. 25, pp. 1483-1491, 2006.
- [57] G. Vegas-Sanchez-Ferrero, J. Seabra, O. Rodriguez-Leor, A. Serrano-Vida, S. Aja-Fernandez, C. Palencia, *et al.*, "Gamma mixture classifier for plaque detection in intravascular ultrasonic images," *IEEE Trans Ultrason Ferroelectr Freq Control*, vol. 61, pp. 44-61, Jan 2014.
- [58] A. R. Webb, "Gamma mixture models for target recognition," *Pattern Recognition*, vol. 33, pp. 2045-2054, 2000.
- [59] K. Nam, I. M. Rosado-Mendez, L. A. Wirtzfeld, G. Ghoshal, A. D. Pawlicki, E. L. Madsen, *et al.*, "Comparison of ultrasound attenuation and backscatter estimates in layered tissue-mimicking phantoms among three clinical scanners," *Ultrasonic imaging*, vol. 34, pp. 209-221, 2012.
- [60] !!! INVALID CITATION !!! {Jakeman, 1980, On the statistics of K-distributed noise;Jakeman, 1984, Speckle statistics with a small number of scatterers;Shankar, 1993, Use of non-Rayleigh statistics for the identification of tumors in ultrasonic B-scans of the breast;Bigelow, 2001, Experimental evaluation on nonlinear indices for ultrasound transducer characterizations}.
- [61] L. A. Wirtzfeld, K. Nam, Y. Labyed, G. Ghoshal, A. Haak, E. Sen-Gupta, *et al.*, "Techniques and evaluation from a cross-platform imaging comparison of quantitative ultrasound parameters in an in vivo rodent fibroadenoma model," *Ultrasonics, Ferroelectrics and Frequency Control, IEEE Transactions on*, vol. 60, 2013.
- [62] K. Nam, I. M. Rosado-Mendez, L. A. Wirtzfeld, A. D. Pawlicki, V. Kumar, E. L. Madsen, *et al.*, "Ultrasonic attenuation and backscatter coefficient estimates of rodent-tumor-mimicking structures: comparison of results among clinical scanners," *Ultrasonic imaging*, vol. 33, pp. 233-250, 2011.

- [63] N. Vlassis and A. Likas, "A Greedy EM Algorithm for Gaussian Mixture Learning," *Neural Processing Letters*, vol. 15, pp. 77-87, 2002/02/01 2002.

APPENDIX A

SUPPLEMENTARY PLOTS FOR CHAPTER 2

Figures for Chapter 2 showing attenuation plotted against gestational age for the varying pulse lengths and number of echoes for Spectral log difference algorithm.

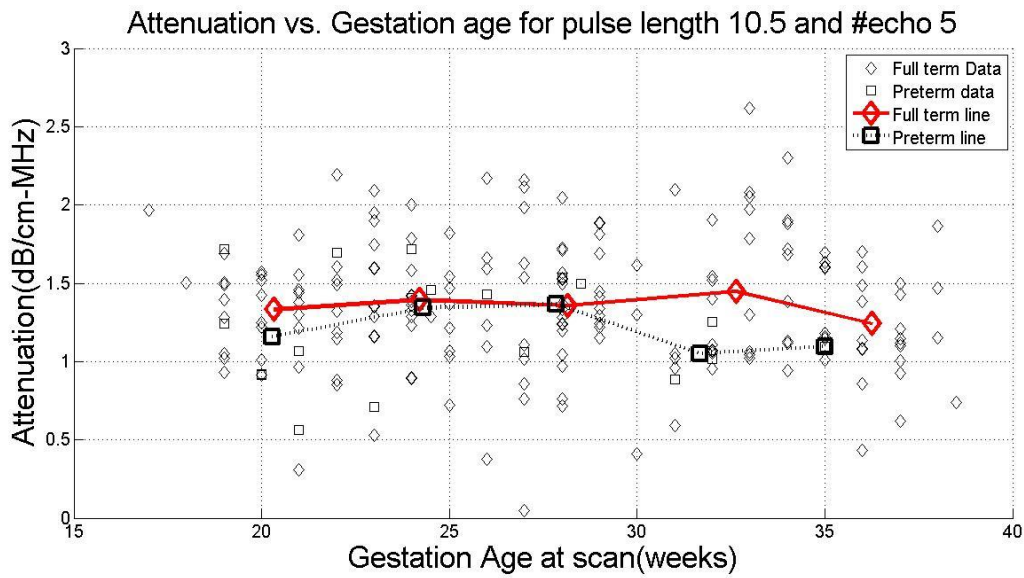


Figure 20: Attenuation vs gestation age for pulse length of 10.5 and 5 independent echoes

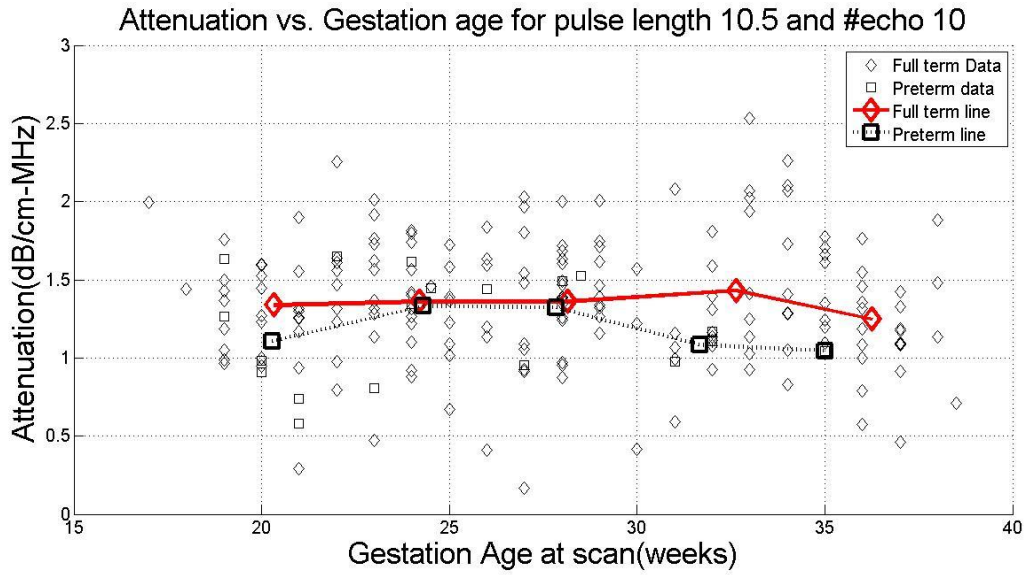


Figure 21: Attenuation vs gestation age for pulse length of 10.5 and 10 independent echoes

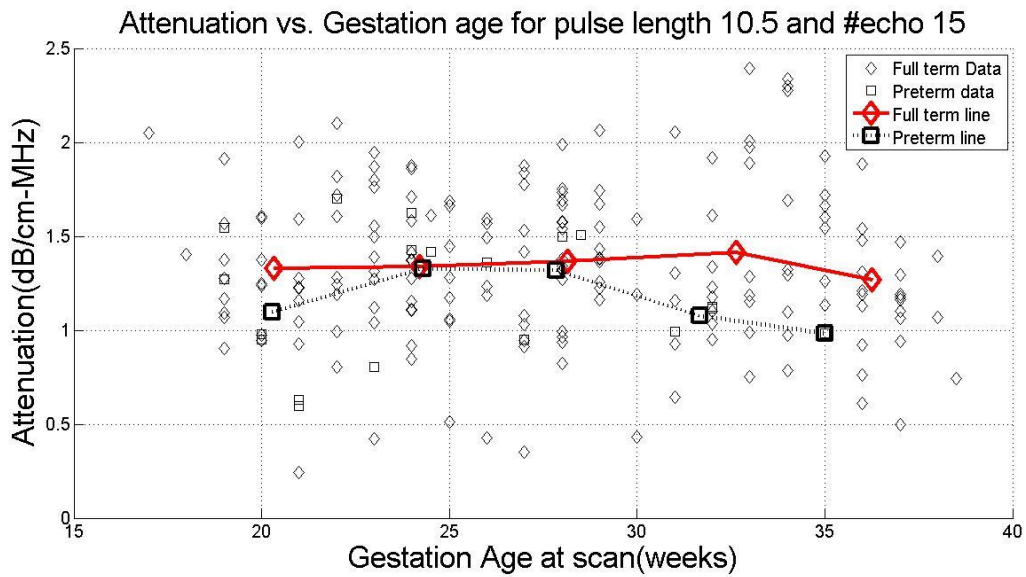


Figure 22: Attenuation vs gestation age for pulse length of 10.5 and 15 independent echoes

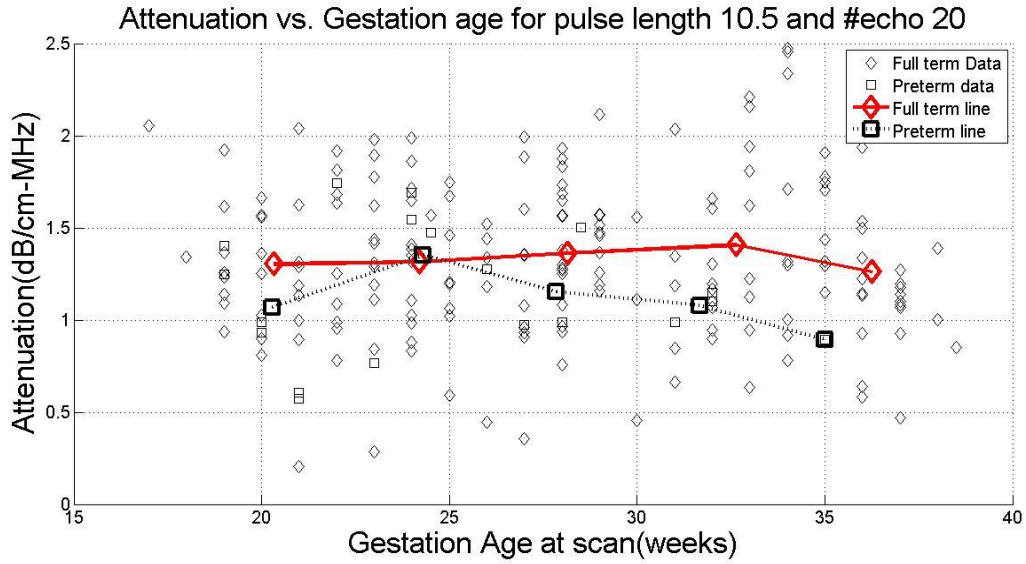


Figure 23: Attenuation vs gestation age for pulse length of 10.5 and 20 independent echoes

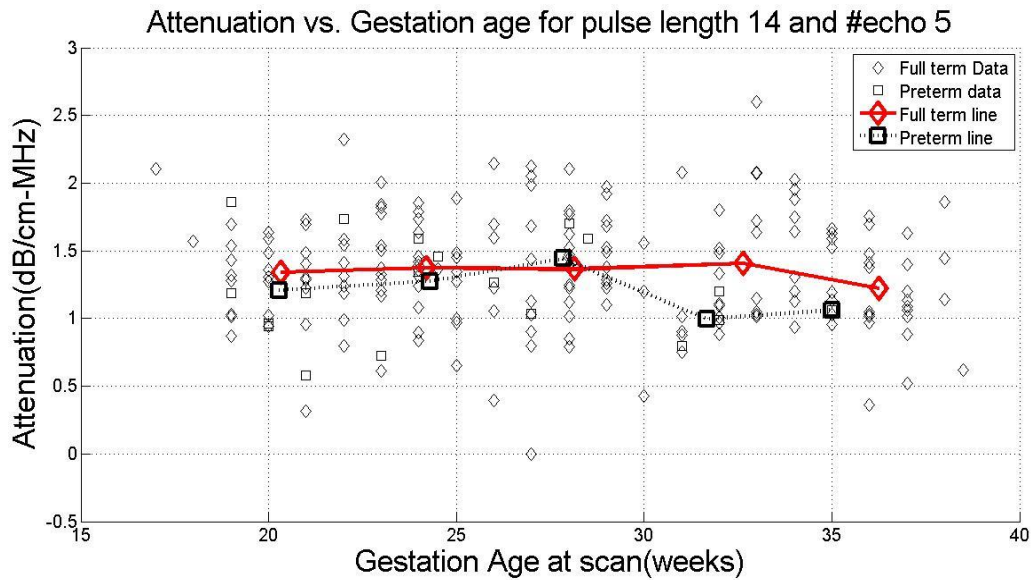


Figure 24: Attenuation vs gestation age for pulse length of 14 and 5 independent echoes

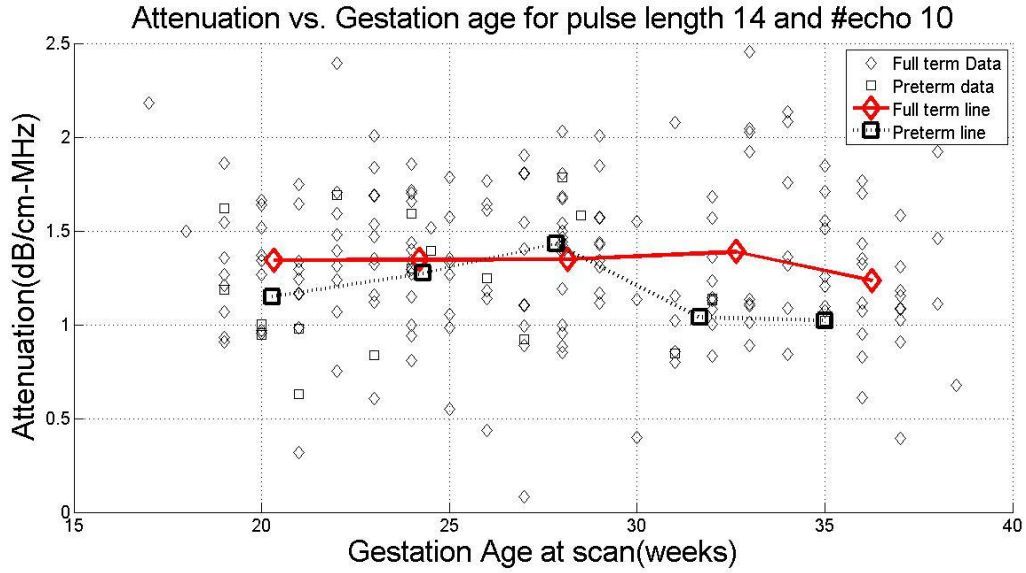


Figure 25: Attenuation vs gestation age for pulse length of 14 and 10 independent echoes

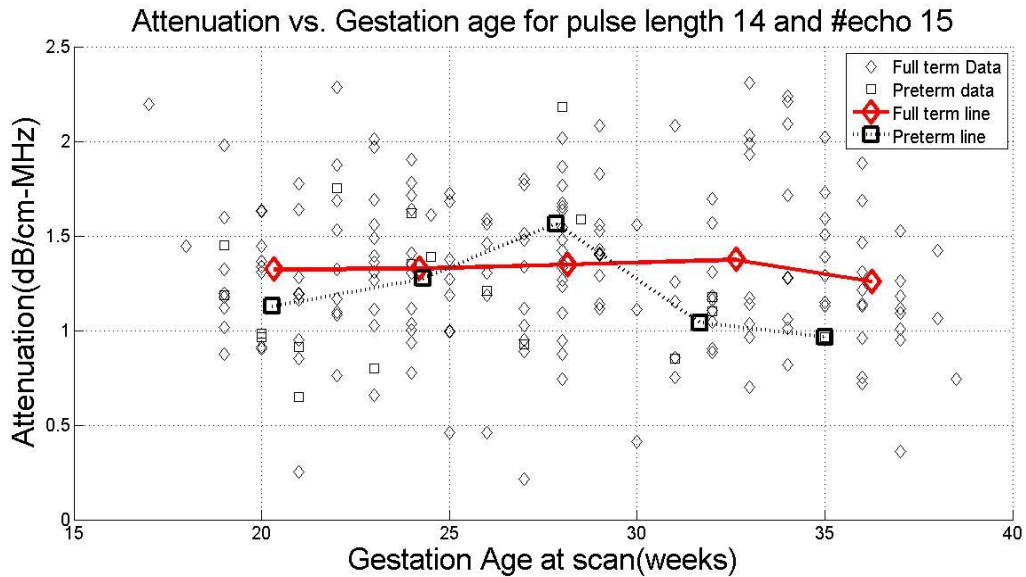


Figure 26: Attenuation vs gestation age for pulse length of 14 and 15 independent echoes

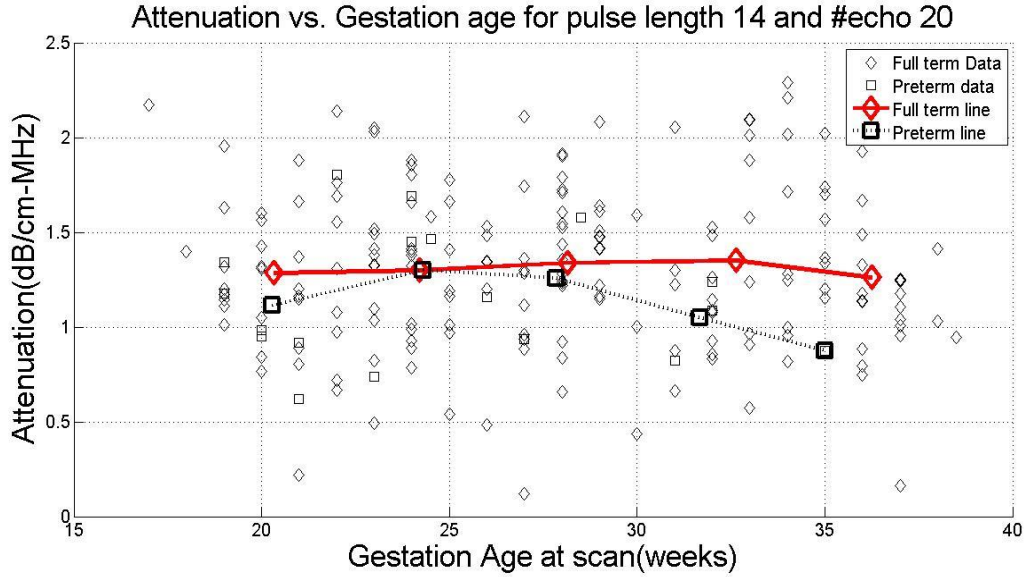


Figure 27: Attenuation vs gestation age for pulse length of 14 and 20 independent echoes

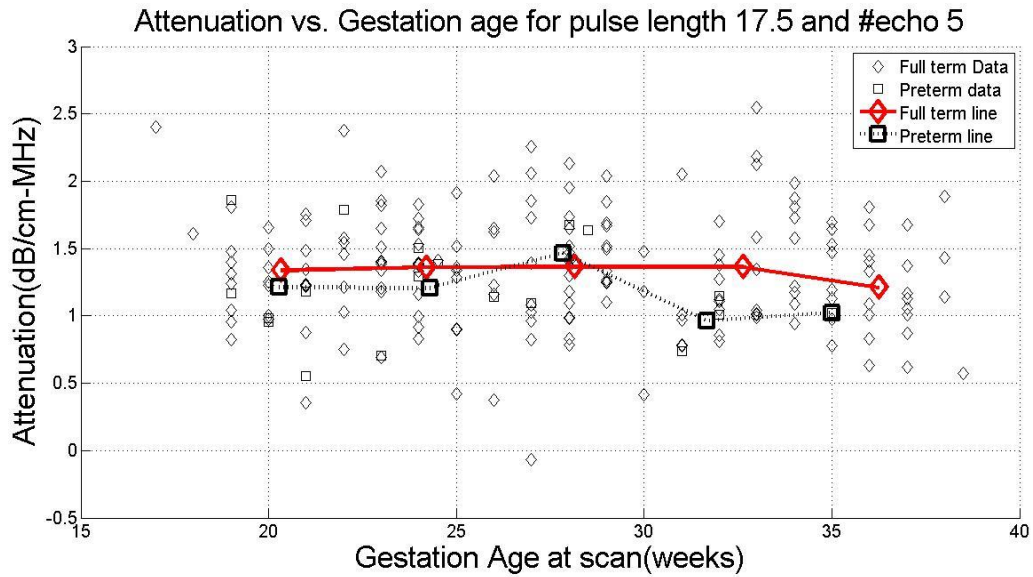


Figure 28: Attenuation vs gestation age for pulse length of 17.5 and 5 independent echoes

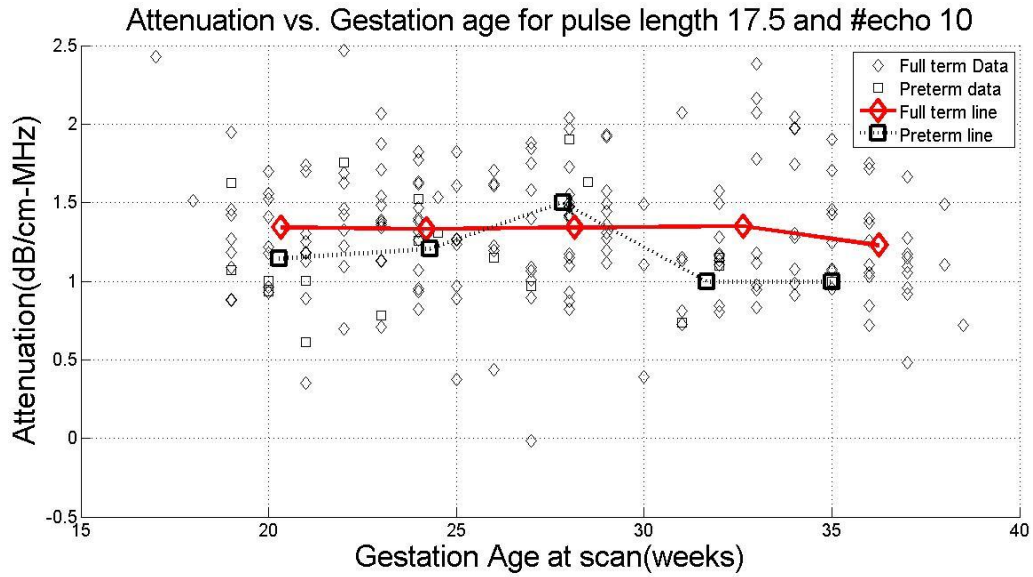


Figure 29: Attenuation vs gestation age for pulse length of 17.5 and 10 independent echoes

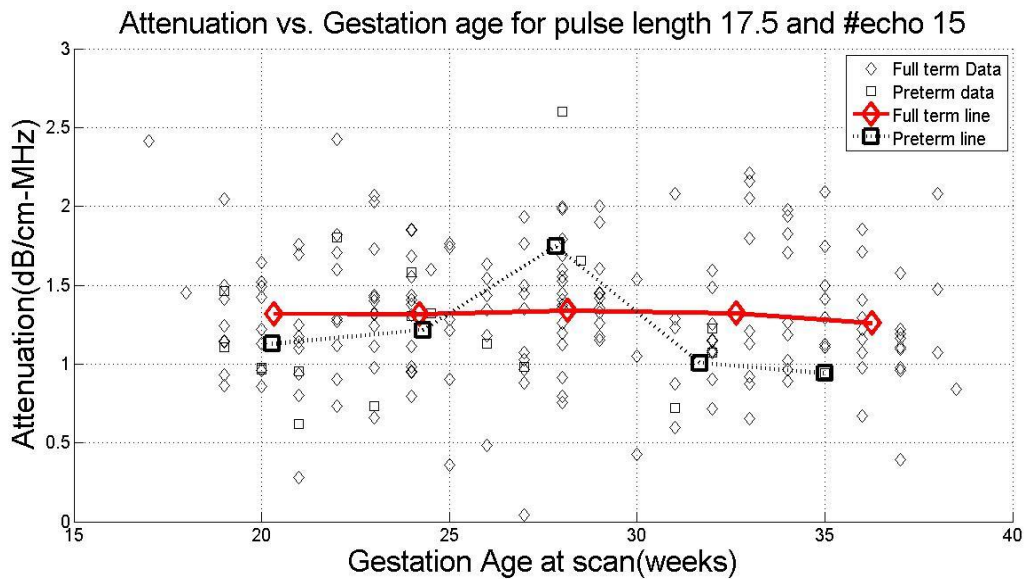


Figure 30: Attenuation vs gestation age for pulse length of 17.5 and 15 independent echoes

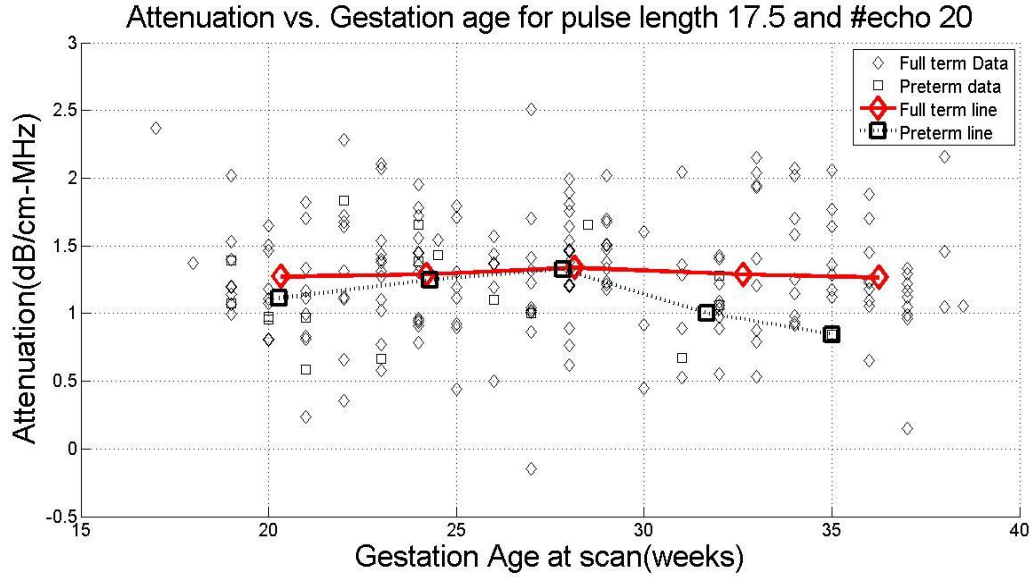


Figure 31: Attenuation vs gestation age for pulse length of 17.5 and 20 independent echoes

Figures for Chapter 2 showing attenuation plotted against gestational age for the varying pulse lengths and number of echoes for Spectral difference algorithm.

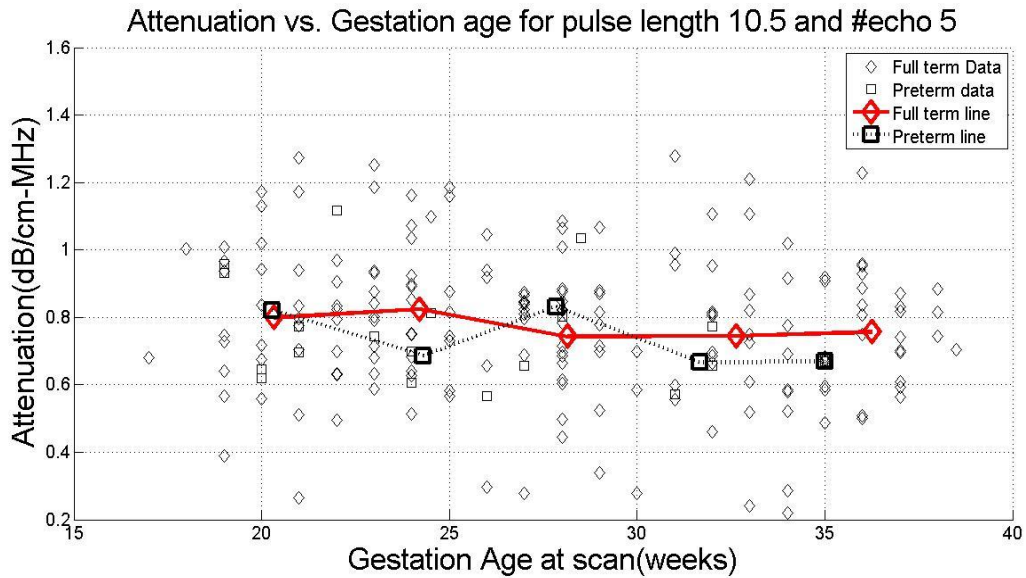


Figure 32: Attenuation vs gestation age for pulse length of 10.5 and 5 independent echoes

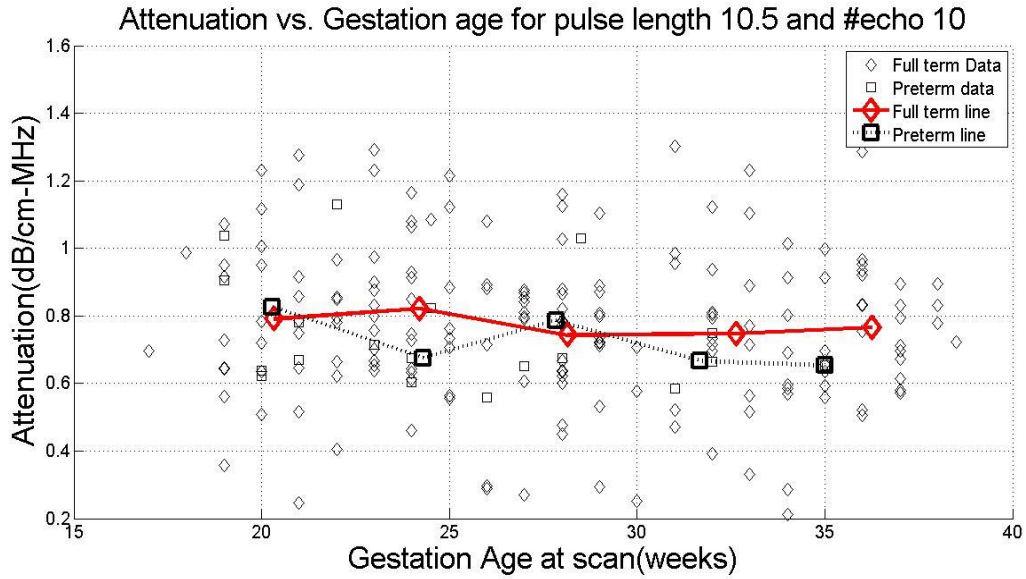


Figure 33: Attenuation vs gestation age for pulse length of 10.5 and 10 independent echoes

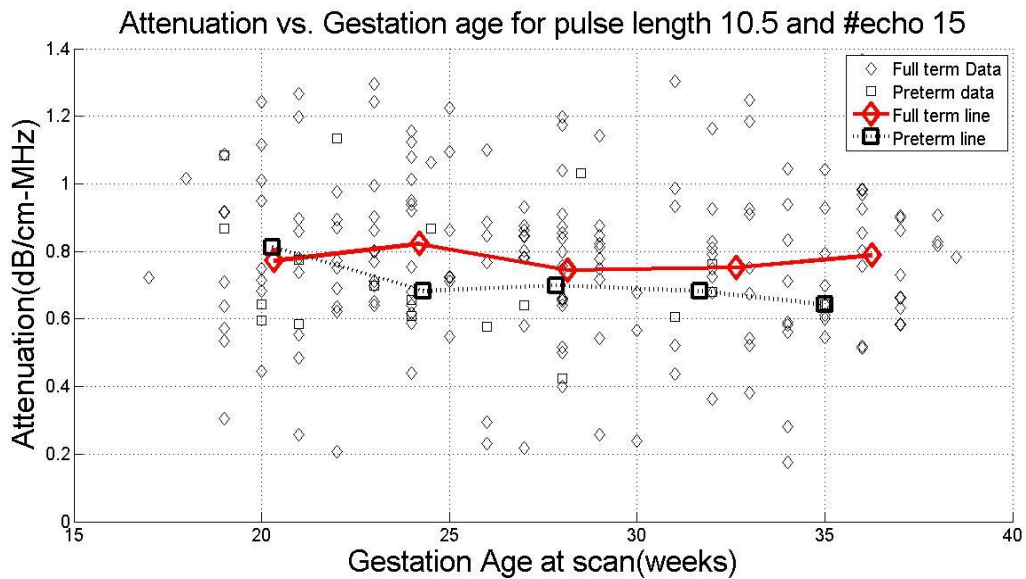


Figure 34: Attenuation vs gestation age for pulse length of 10.5 and 15 independent echoes

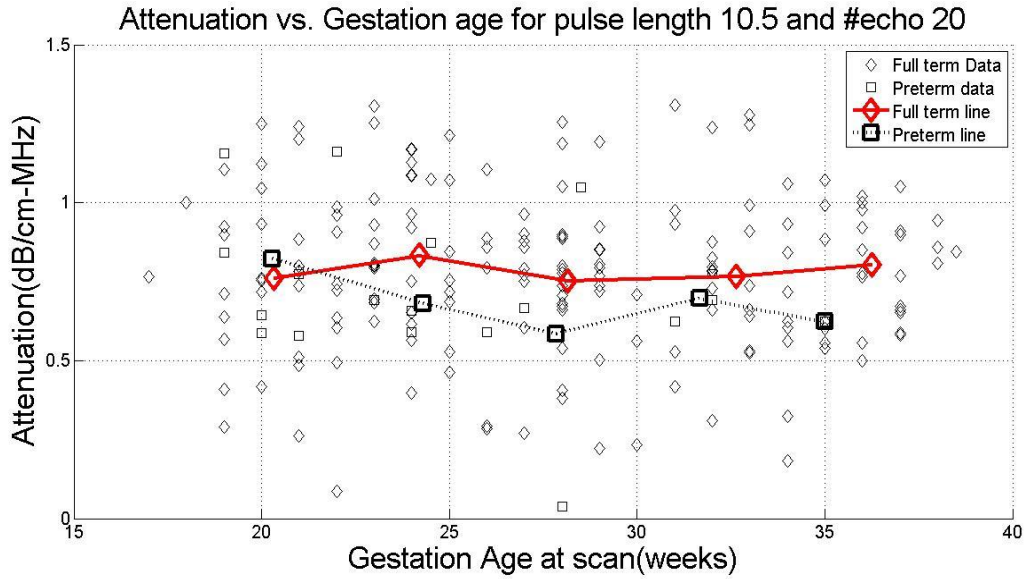


Figure 35: Attenuation vs gestation age for pulse length of 10.5 and 20 independent echoes

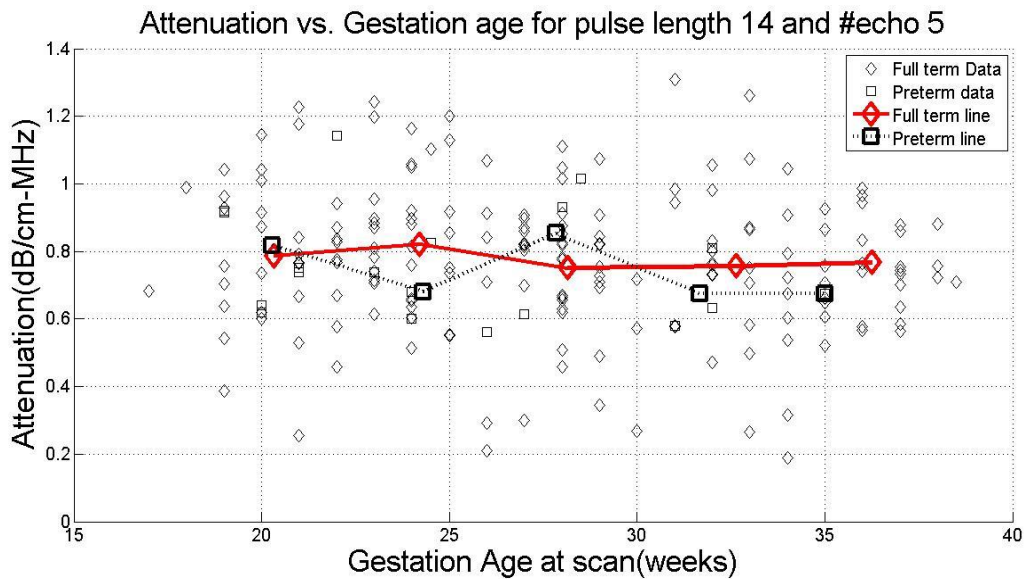


Figure 36: Attenuation vs gestation age for pulse length of 14 and 5 independent echoes

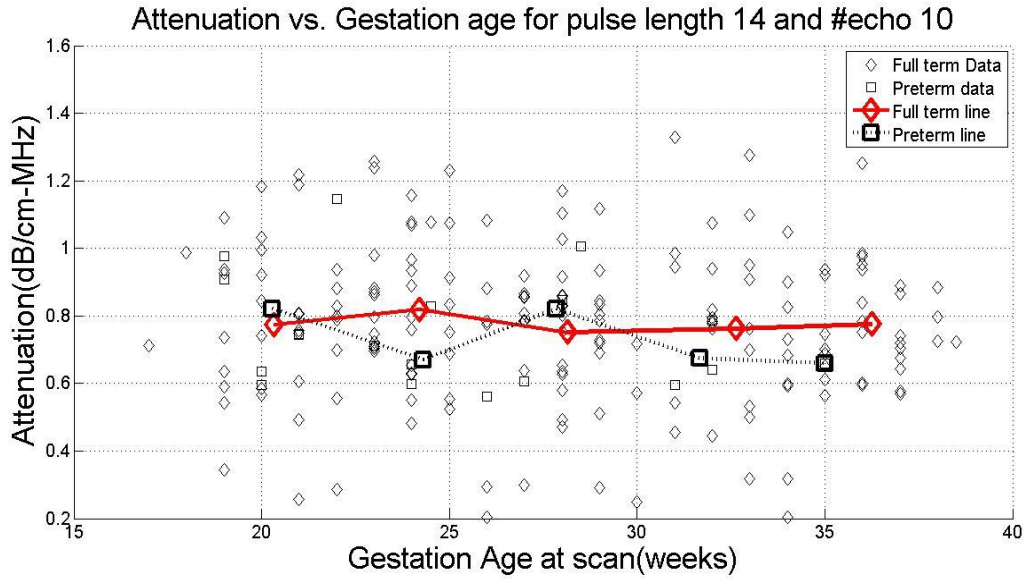


Figure 37: Attenuation vs gestation age for pulse length of 14 and 10 independent echoes

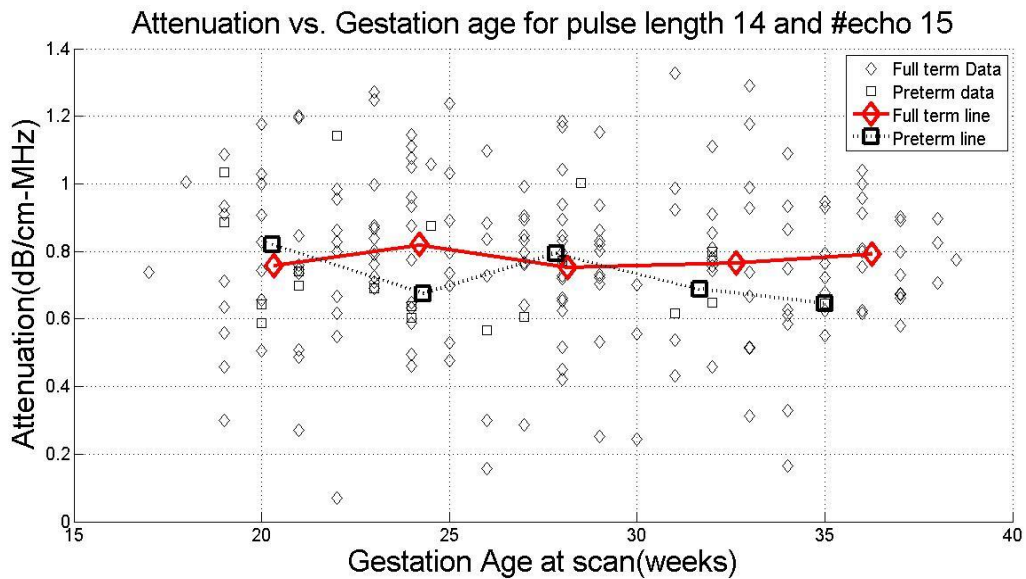


Figure 38: Attenuation vs gestation age for pulse length of 14 and 15 independent echoes

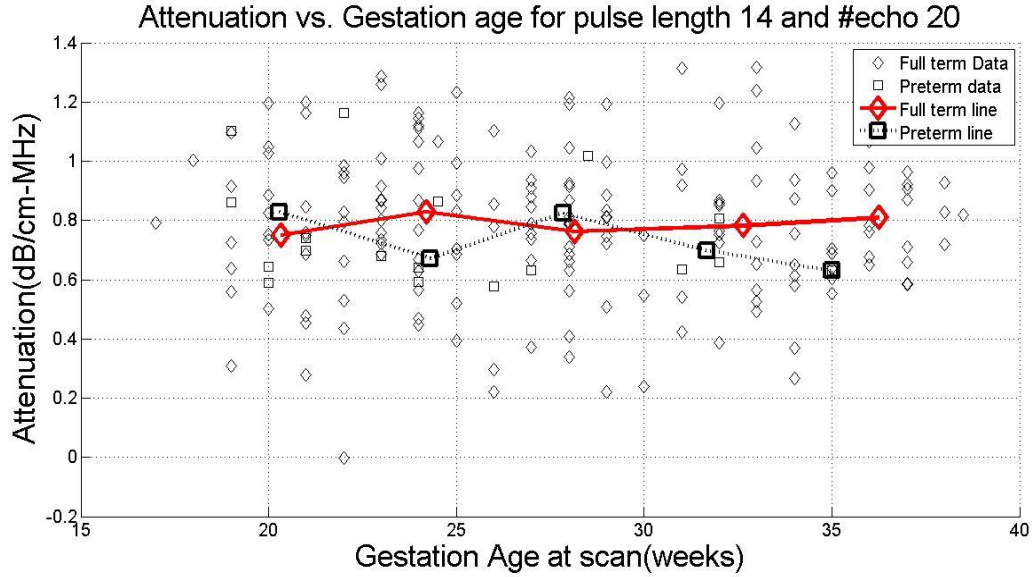


Figure 39: Attenuation vs gestation age for pulse length of 14 and 20 independent echoes

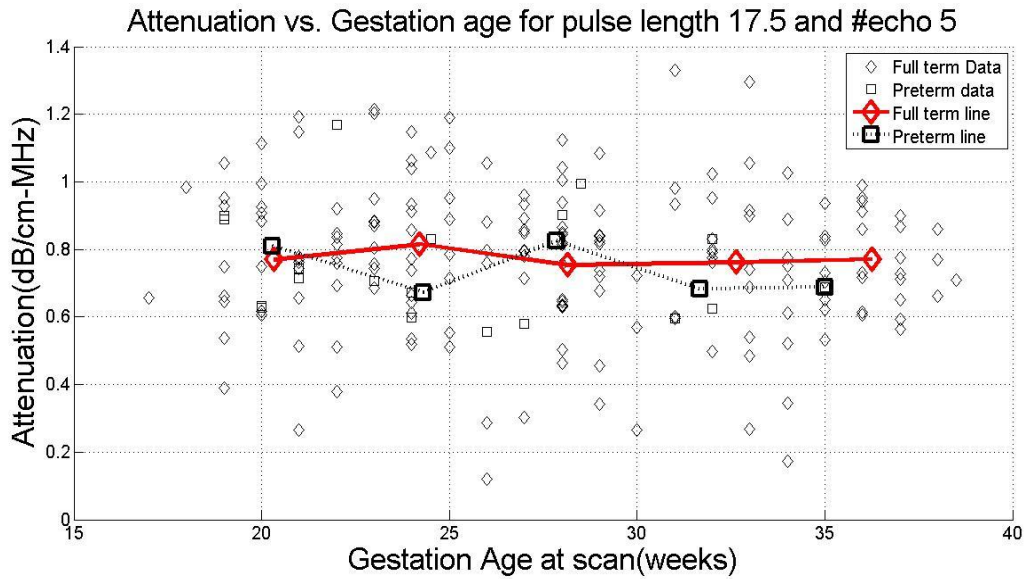


Figure 40: Attenuation vs gestation age for pulse length of 17.5 and 5 independent echoes

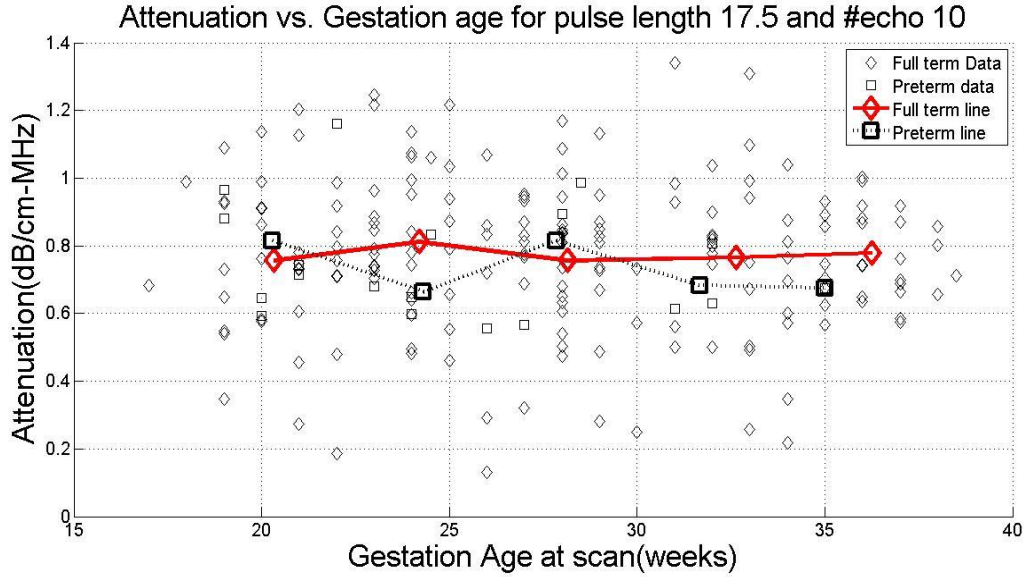


Figure 41: Attenuation vs gestation age for pulse length of 17.5 and 10 independent echoes

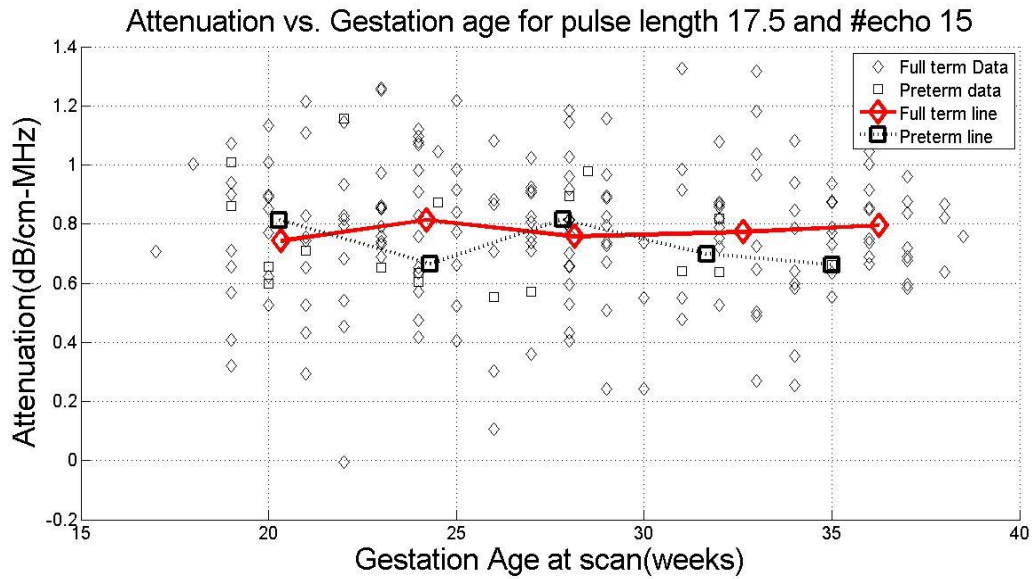


Figure 42: Attenuation vs gestation age for pulse length of 17.5 and 15 independent echoes

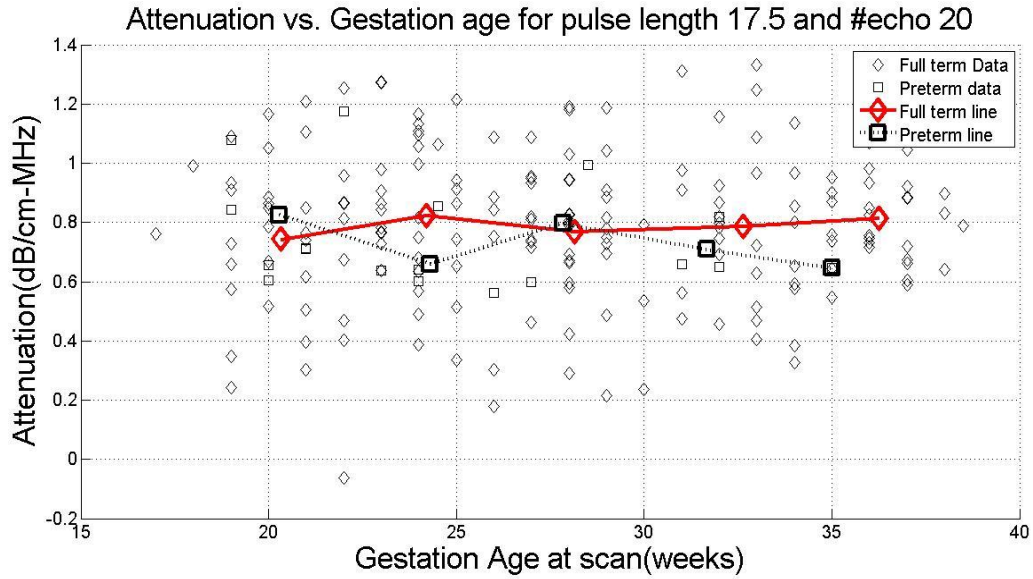


Figure 43: Attenuation vs gestation age for pulse length of 17.5 and 20 independent echoes

Figures for Chapter 2 showing change in attenuation plotted against time to delivery for the varying pulse lengths and number of echoes for Spectral log difference algorithm.

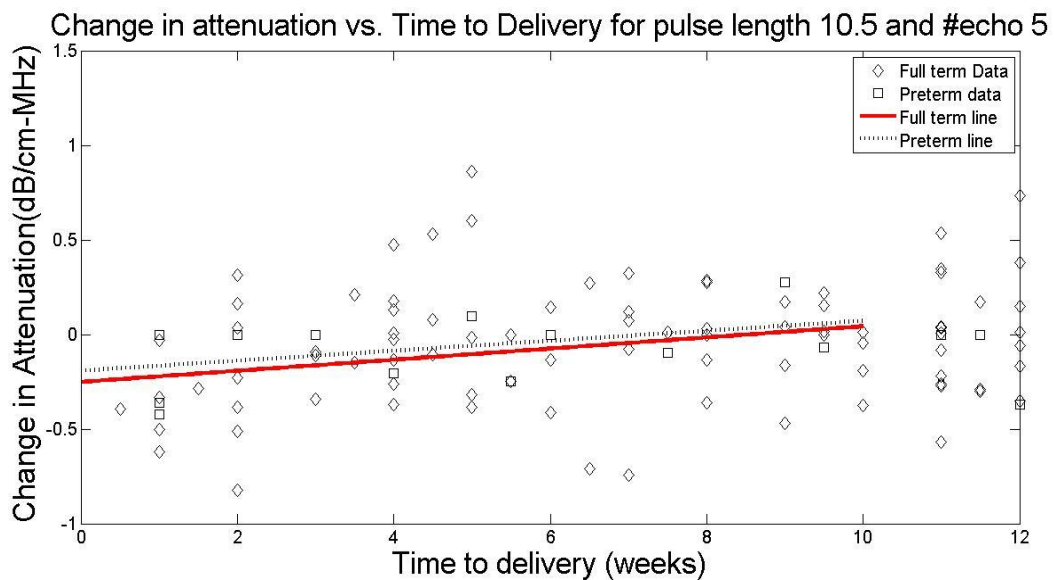


Figure 44: Change in attenuation vs time to delivery for pulse length of 10.5 and 5 independent echoes

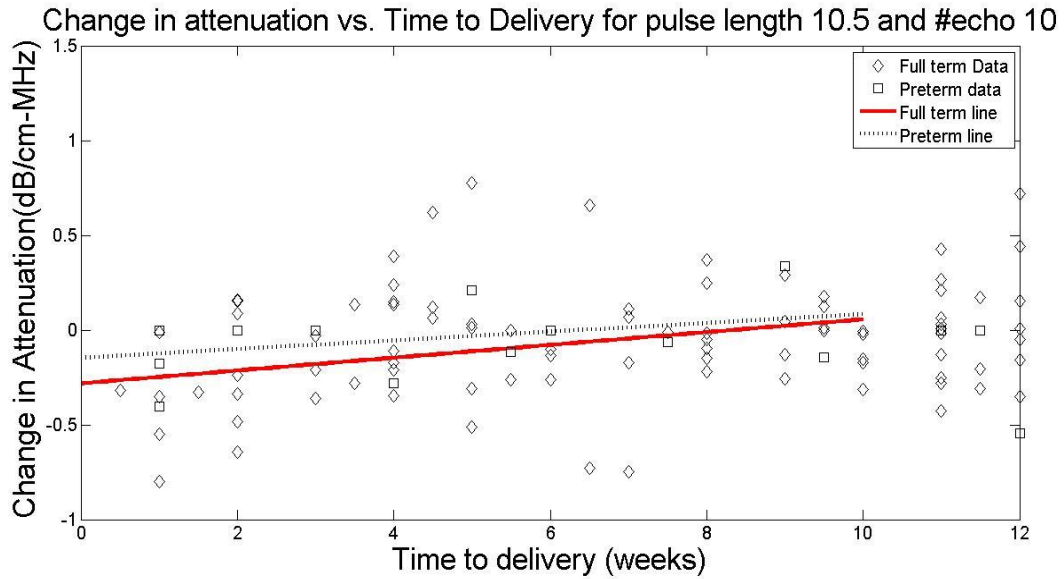


Figure 45: Change in attenuation vs time to delivery for pulse length of 10.5 and 10 independent echoes

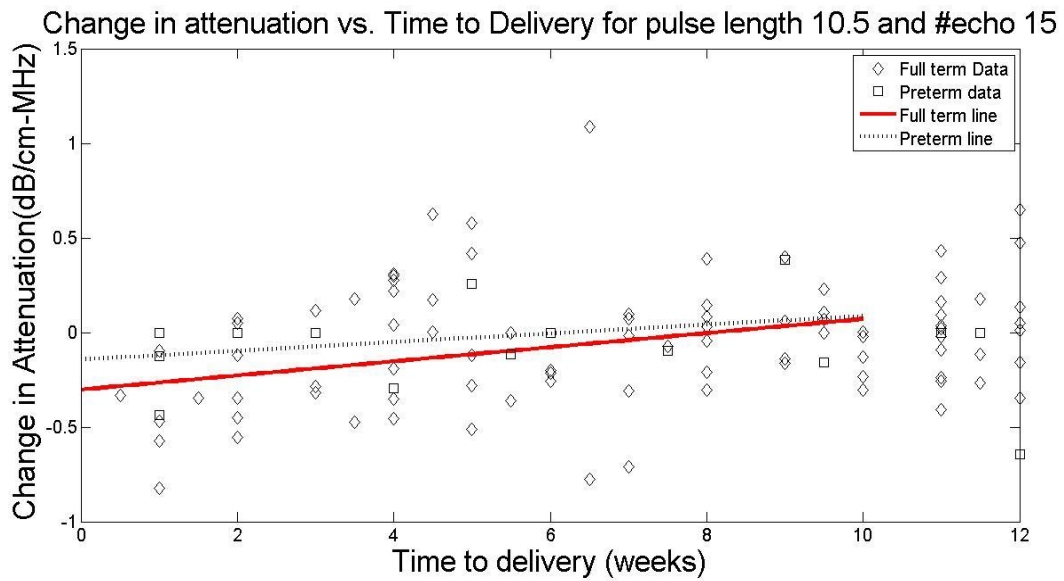


Figure 46: Change in attenuation vs time to delivery for pulse length of 10.5 and 15 independent echoes



Figure 47: Change in attenuation vs time to delivery for pulse length of 10.5 and 20 independent echoes

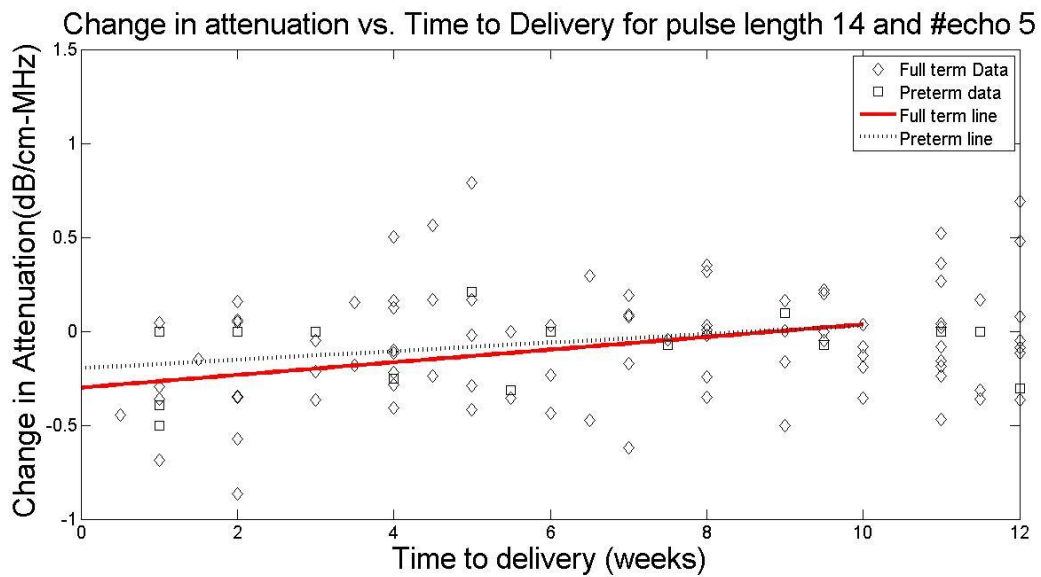


Figure 48: Change in attenuation vs time to delivery for pulse length of 14 and 5 independent echoes

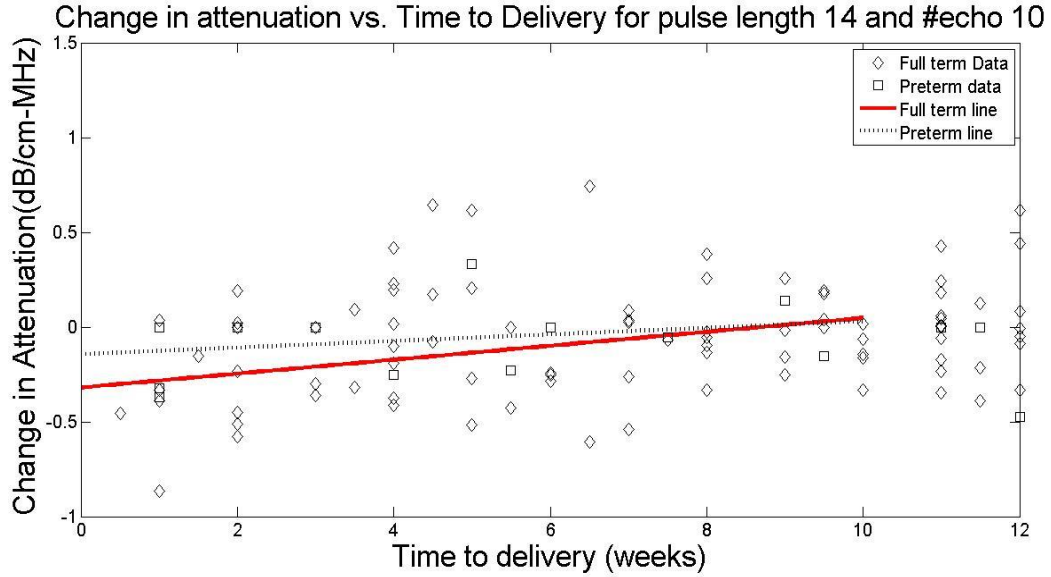


Figure 49: Change in attenuation vs time to delivery for pulse length of 14 and 10 independent echoes

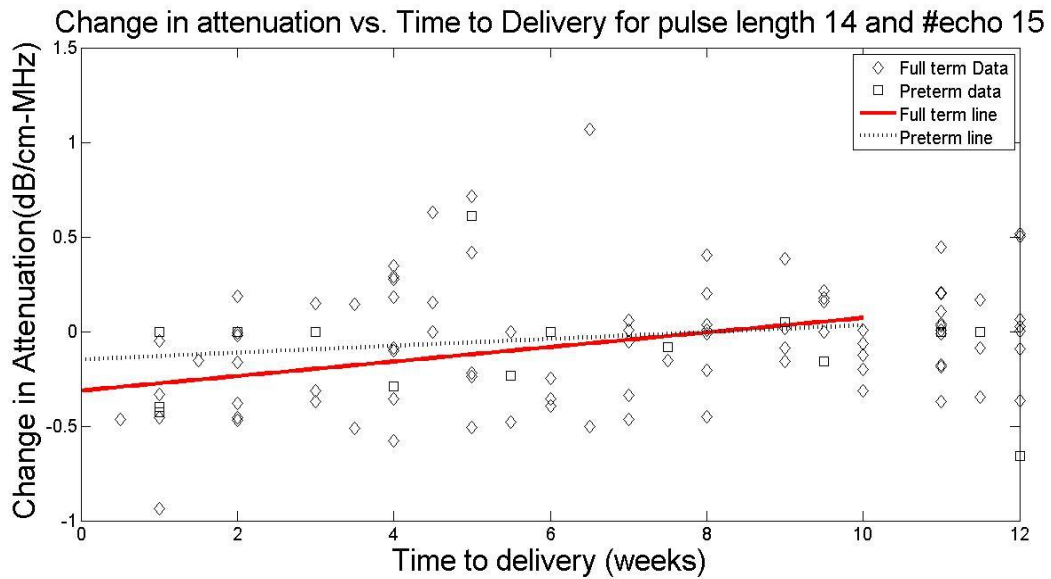


Figure 50: Change in attenuation vs time to delivery for pulse length of 14 and 15 independent echoes

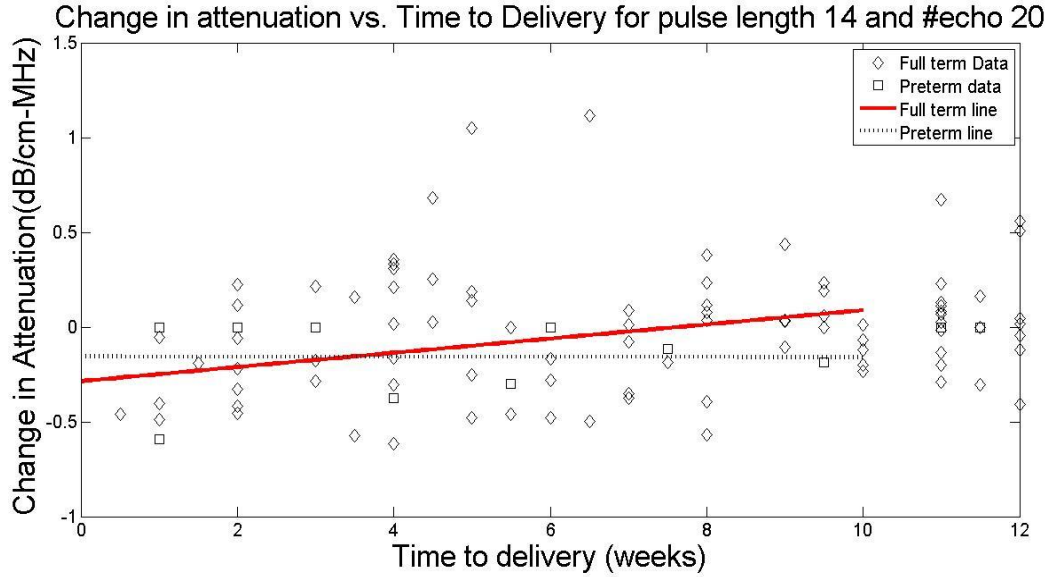


Figure 51: Change in attenuation vs time to delivery for pulse length of 14 and 20 independent echoes

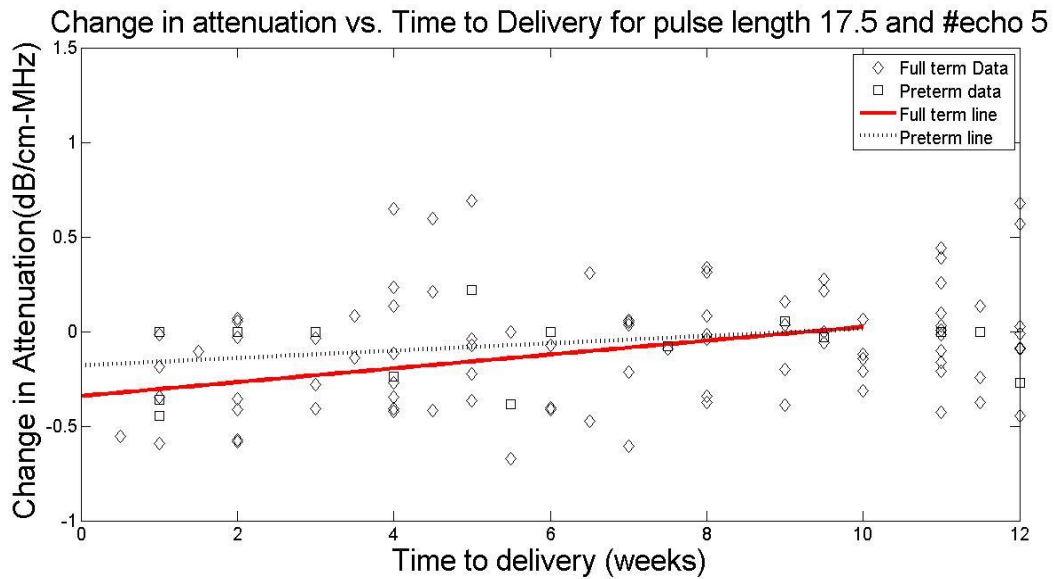


Figure 52: Change in attenuation vs time to delivery for pulse length of 17.5 and 5 independent echoes

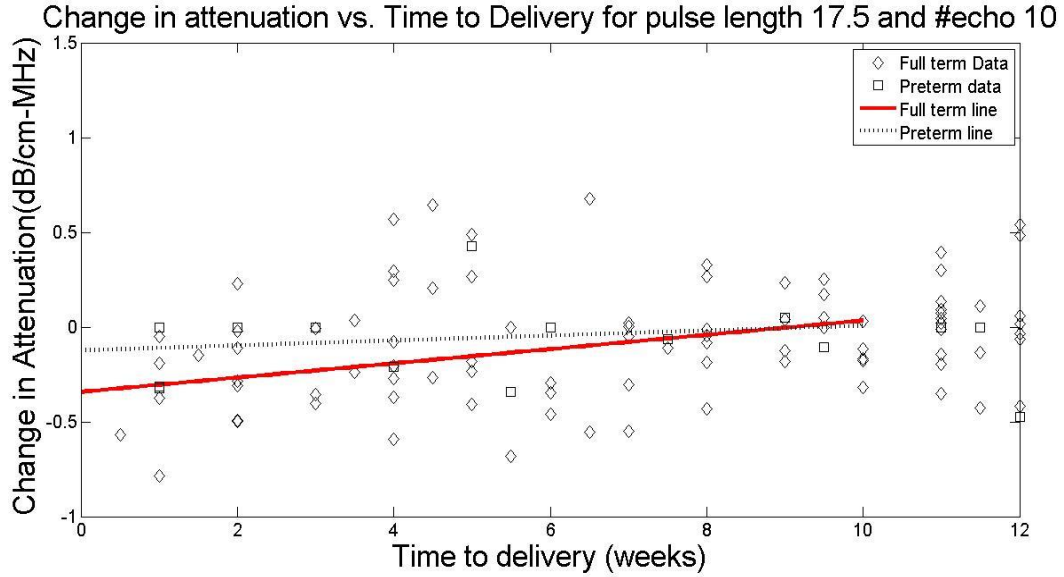


Figure 53: Change in attenuation vs time to delivery for pulse length of 17.5 and 10 independent echoes

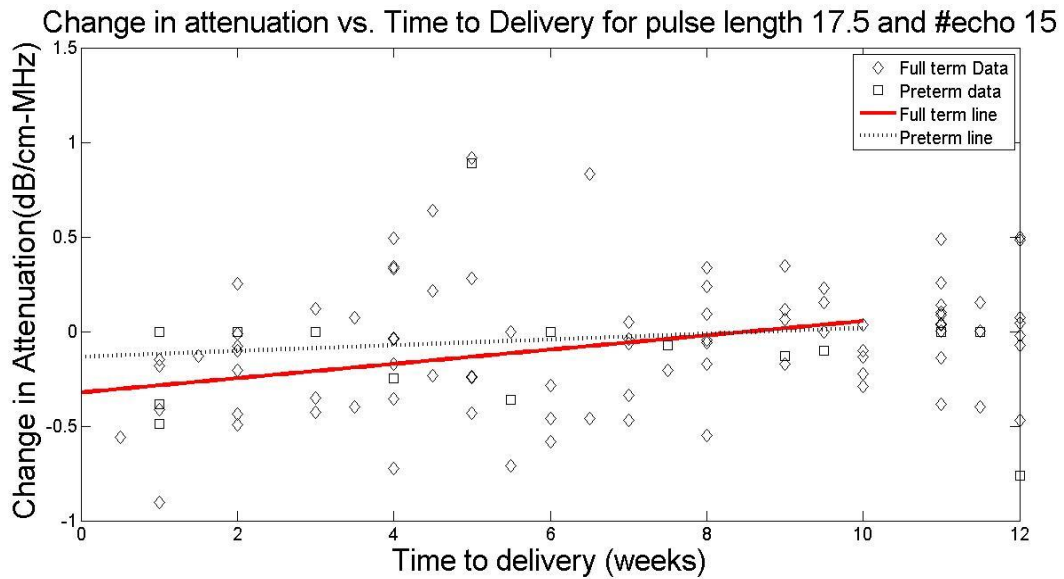


Figure 54: Change in attenuation vs time to delivery for pulse length of 17.5 and 15 independent echoes

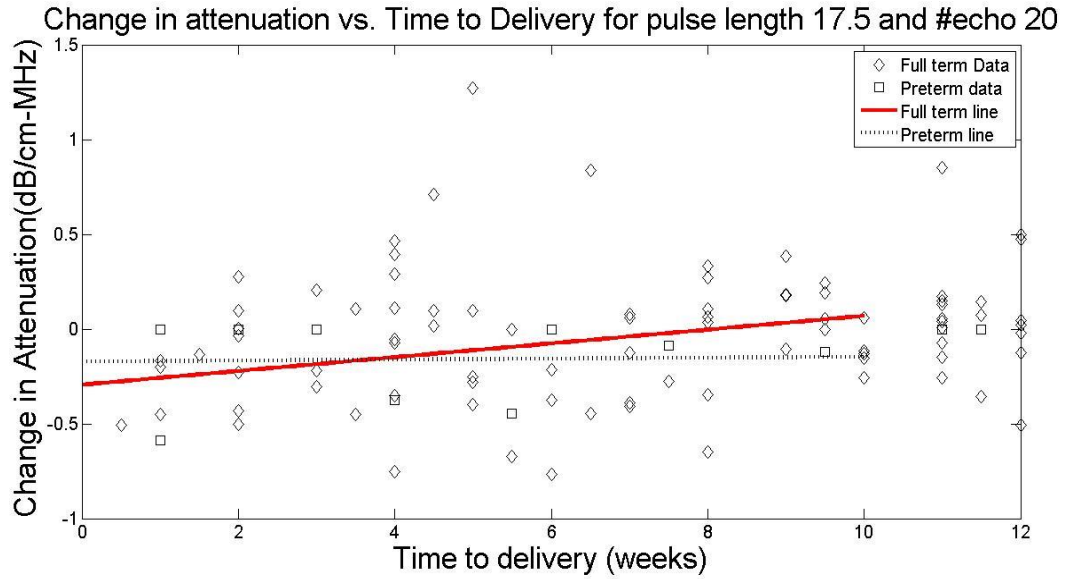


Figure 55: Change in attenuation vs time to delivery for pulse length of 17.5 and 20 independent echoes

Figures for Chapter 2 showing change in attenuation plotted against time to delivery for the varying pulse lengths and number of echoes for Spectral difference algorithm.



Figure 56: Change in attenuation vs time to delivery for pulse length of 10.5 and 5 independent echoes

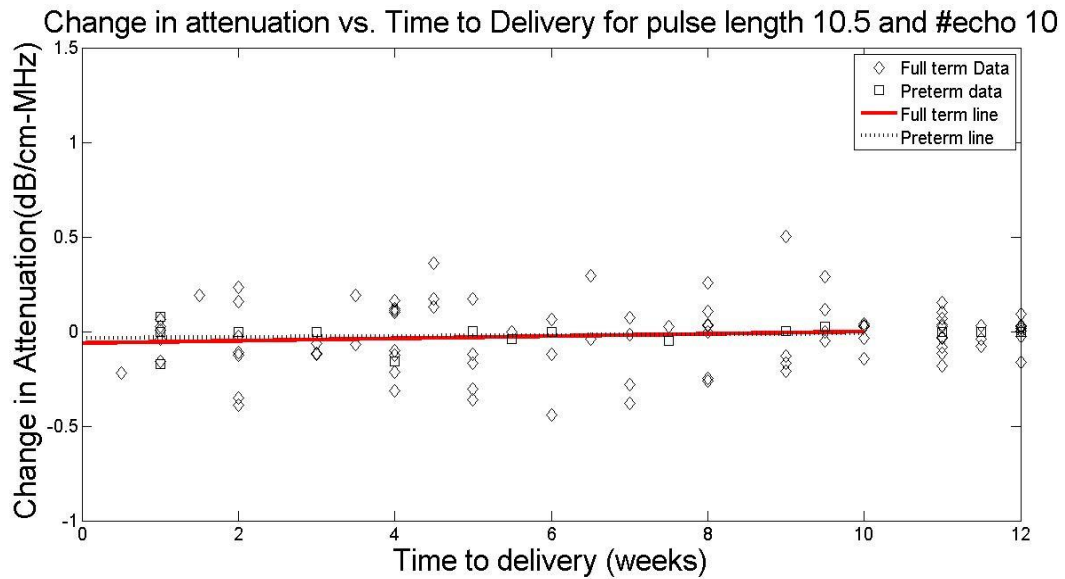


Figure 57: Change in attenuation vs time to delivery for pulse length of 10.5 and 10 independent echoes

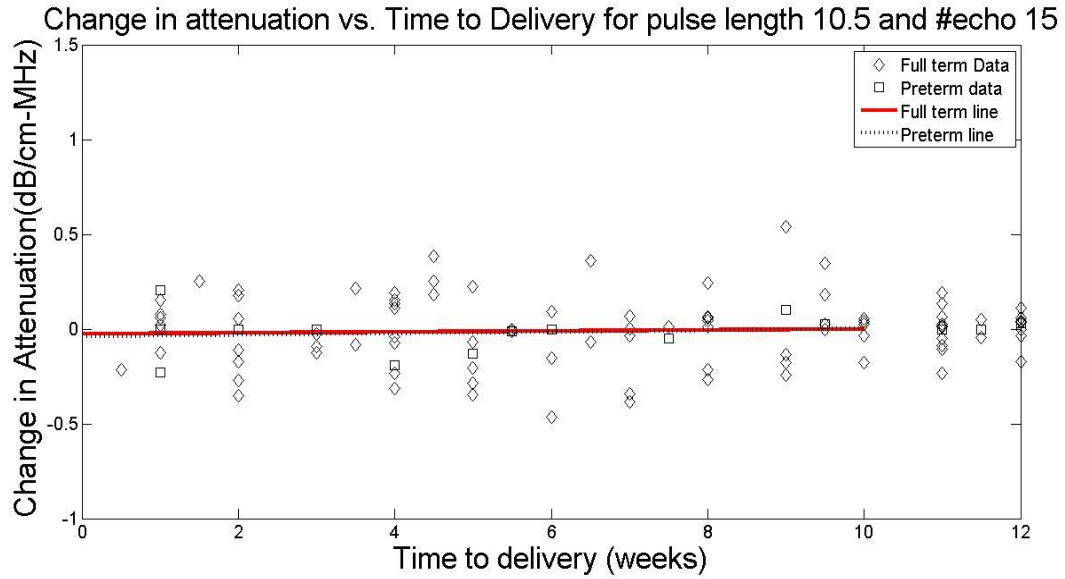


Figure 58: Change in attenuation vs time to delivery for pulse length of 10.5 and 15 independent echoes



Figure 59: Change in attenuation vs time to delivery for pulse length of 10.5 and 20 independent echoes



Figure 60: Change in attenuation vs time to delivery for pulse length of 14 and 5 independent echoes

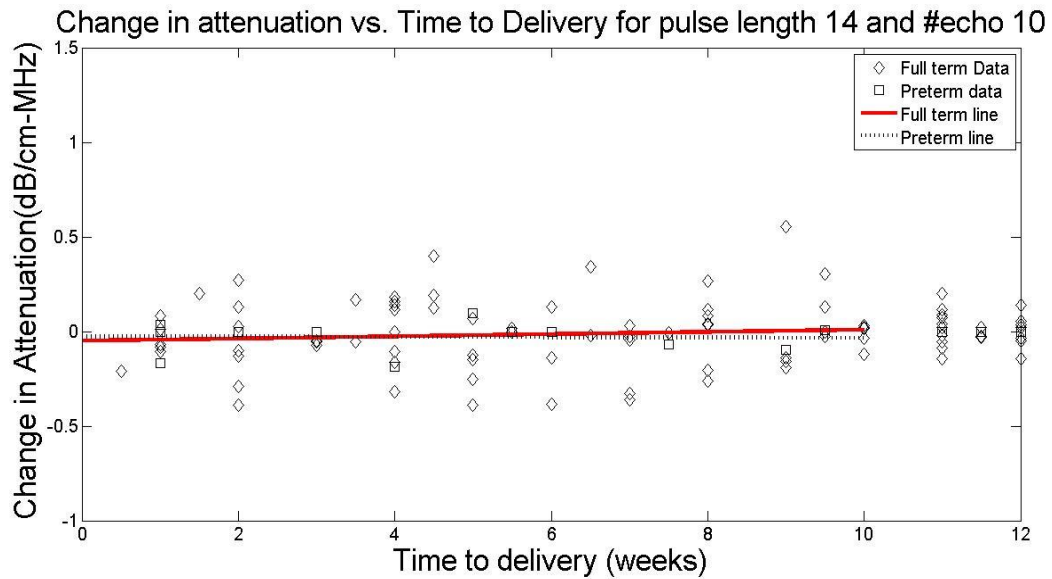


Figure 61: Change in attenuation vs time to delivery for pulse length of 14 and 10 independent echoes

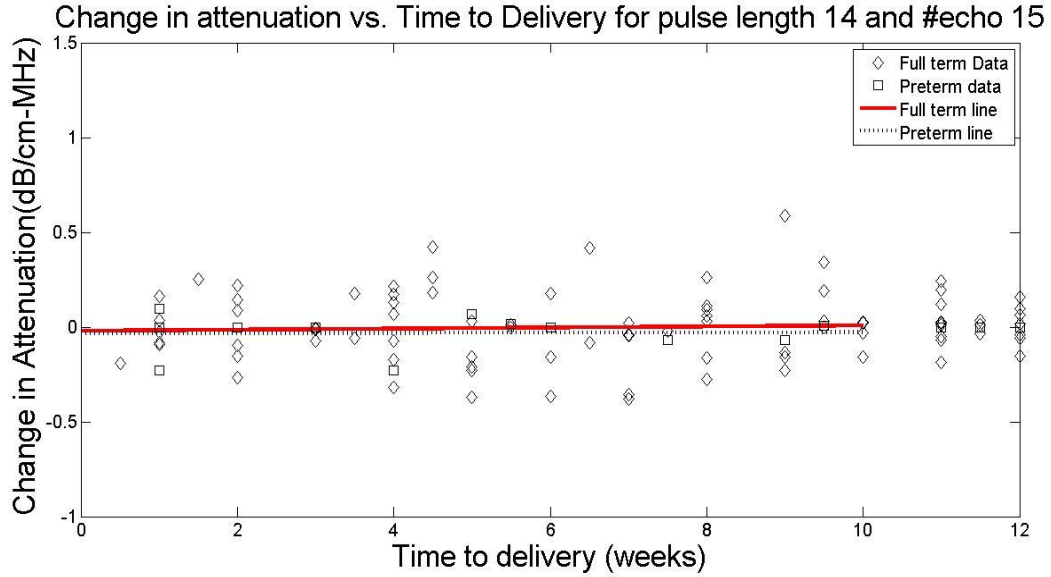


Figure 62: Change in attenuation vs time to delivery for pulse length of 14 and 15 independent echoes

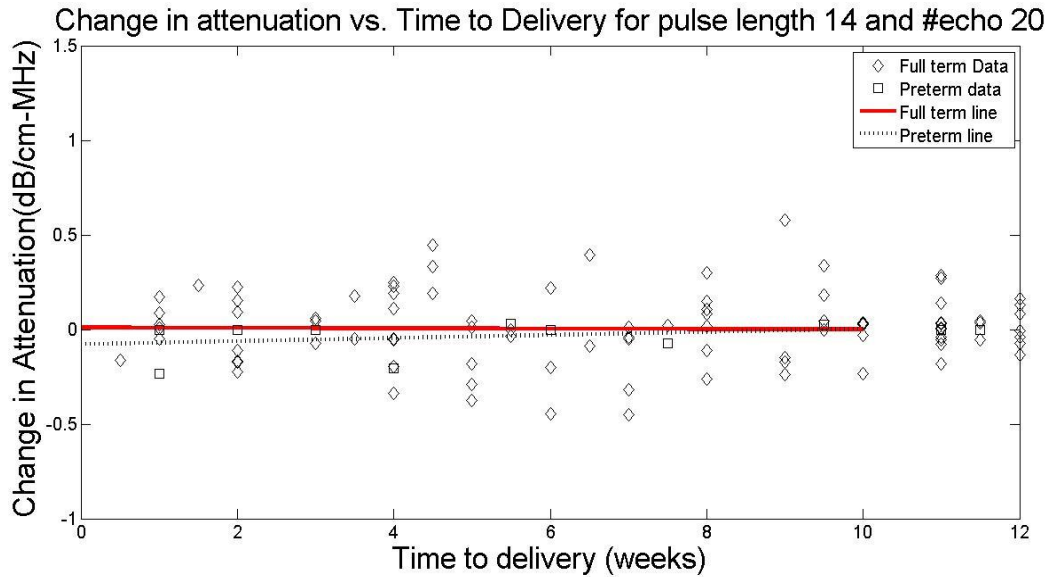


Figure 63: Change in attenuation vs time to delivery for pulse length of 14 and 20 independent echoes

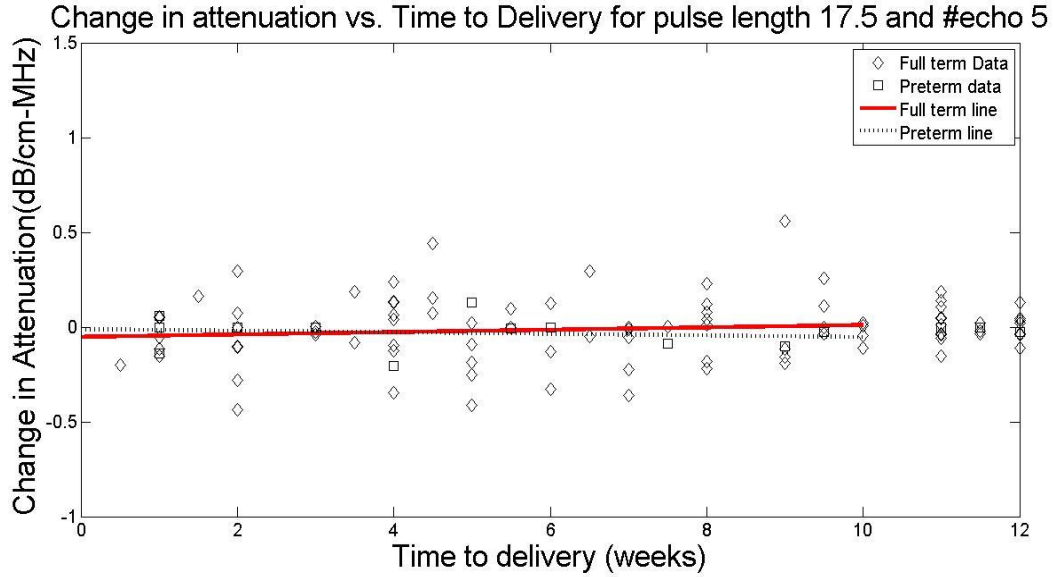


Figure 64: Change in attenuation vs time to delivery for pulse length of 17.5 and 5 independent echoes

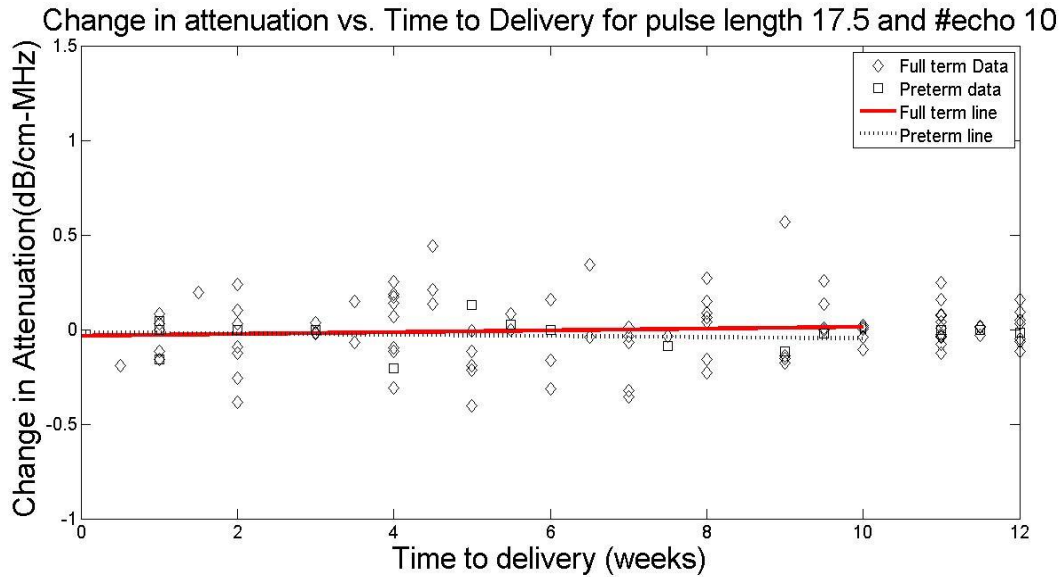


Figure 65: Change in attenuation vs time to delivery for pulse length of 17.5 and 10 independent echoes

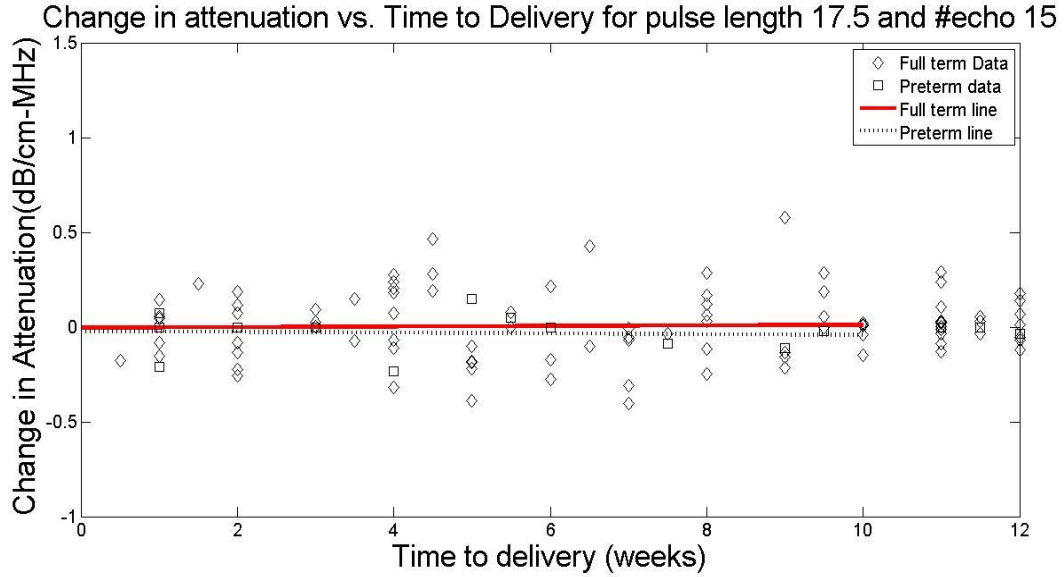


Figure 66: Change in attenuation vs time to delivery for pulse length of 17.5 and 15 independent echoes

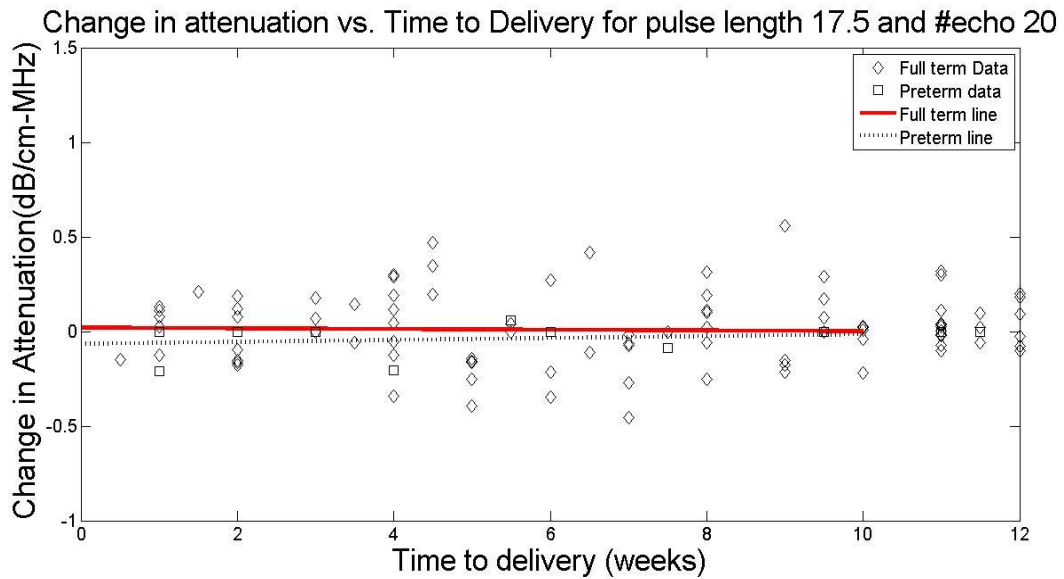


Figure 67: Change in attenuation vs time to delivery for pulse length of 17.5 and 20 independent echoes

Figures for chapter 2 showing ROC curves for the varying pulse lengths and number of echoes for Spectral log difference algorithm.

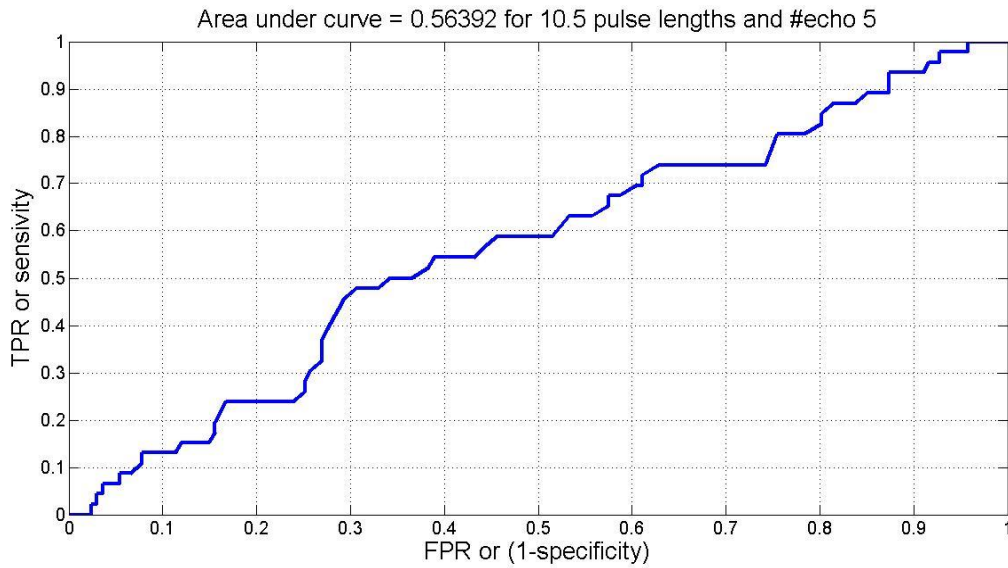


Figure 68: ROC curve for pulse length of 10.5 and 5 independent echoes

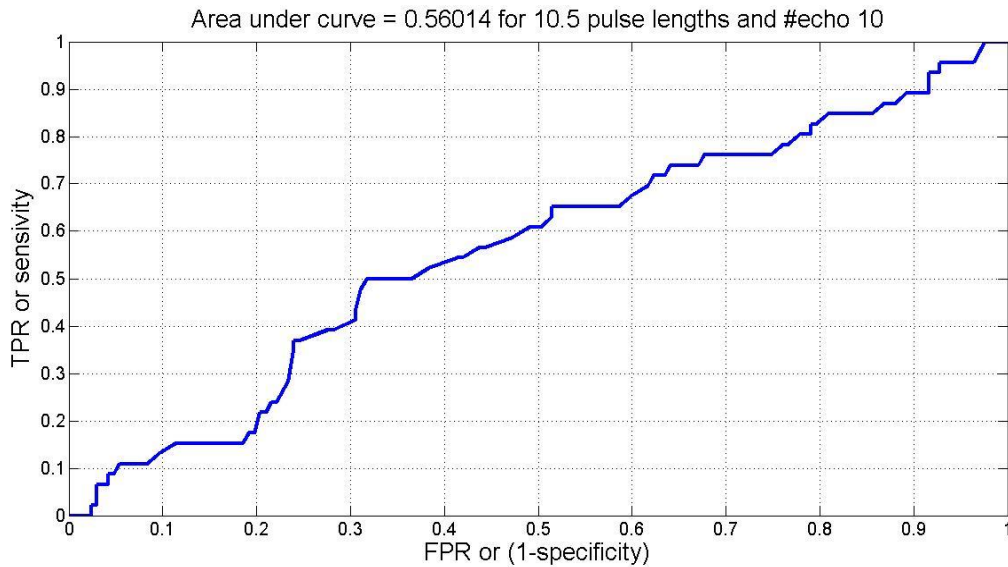


Figure 69: ROC curve for pulse length of 10.5 and 10 independent echoes

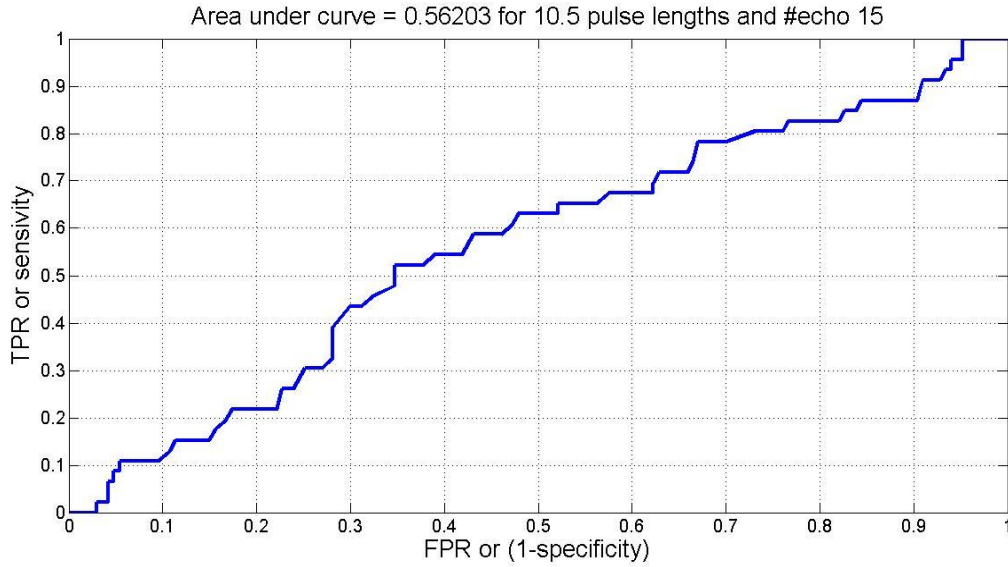


Figure 70: ROC curve for pulse length of 10.5 and 15 independent echoes

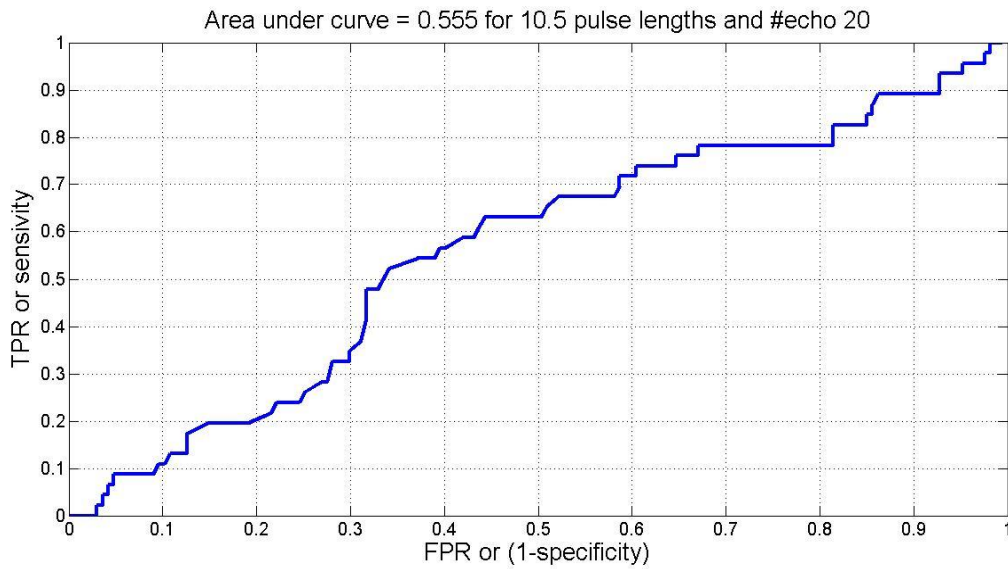


Figure 71: ROC curve for pulse length of 10.5 and 20 independent echoes

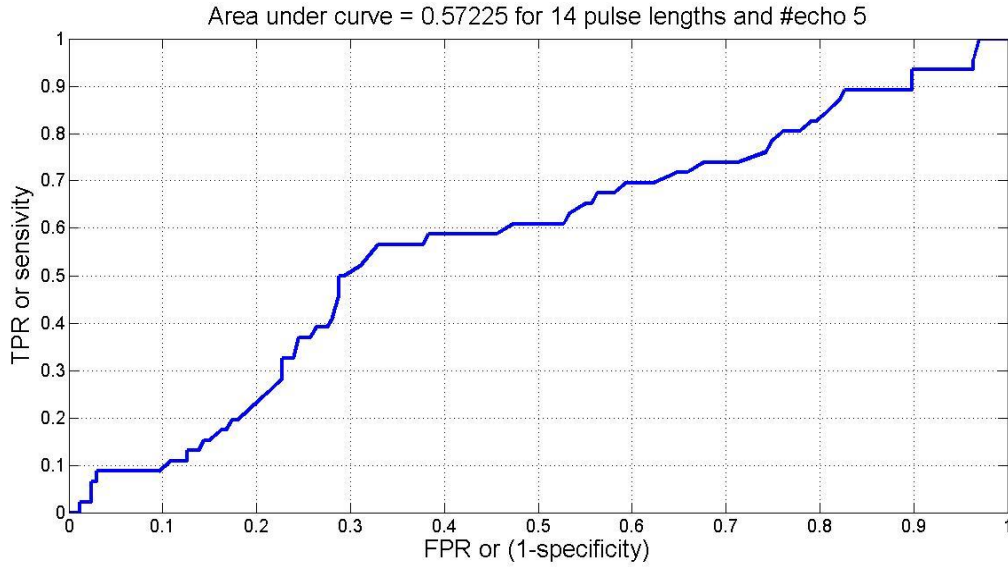


Figure 72: ROC curve for pulse length of 14 and 5 independent echoes

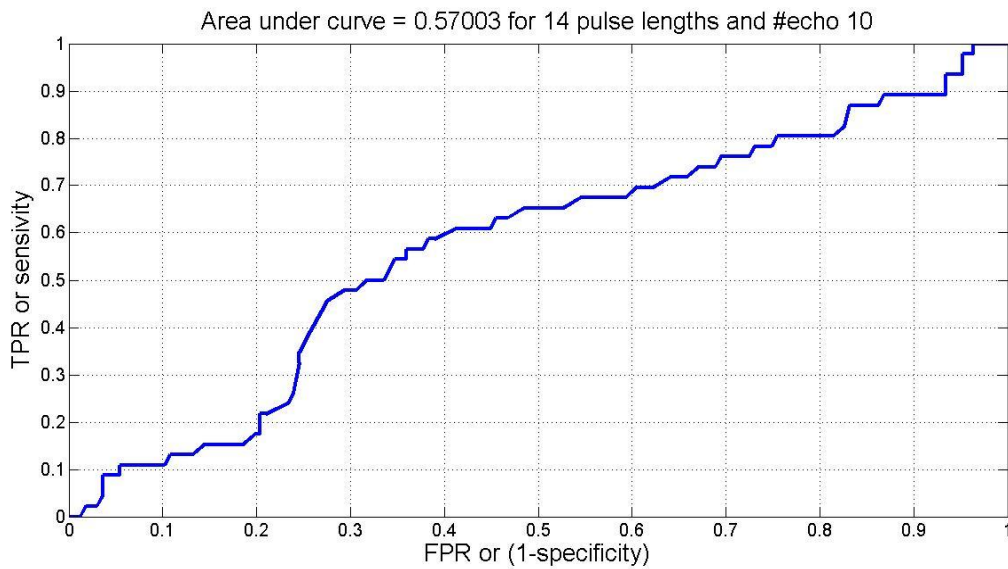


Figure 73: ROC curve for pulse length of 14 and 10 independent echoes

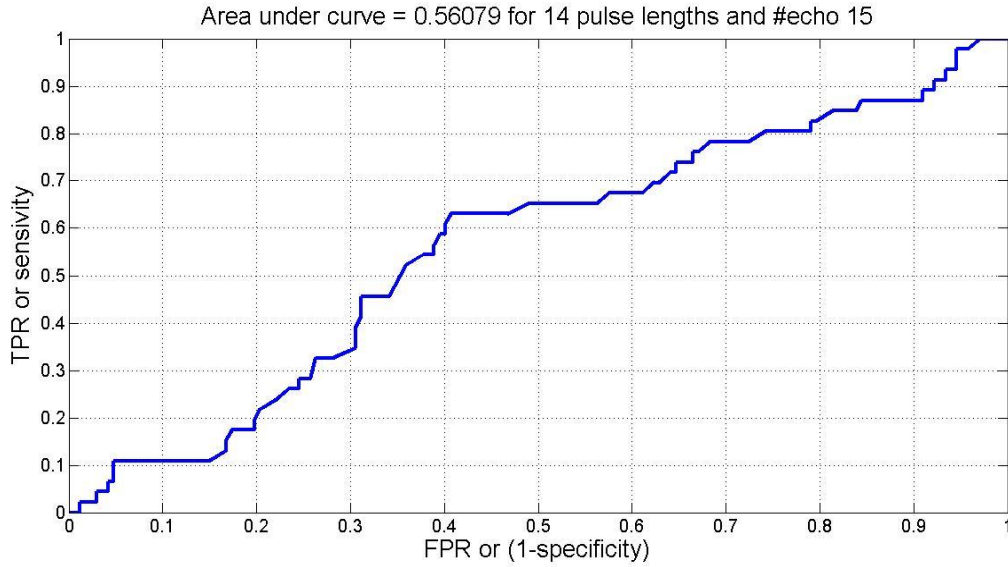


Figure 74: ROC curve for pulse length of 14 and 15 independent echoes

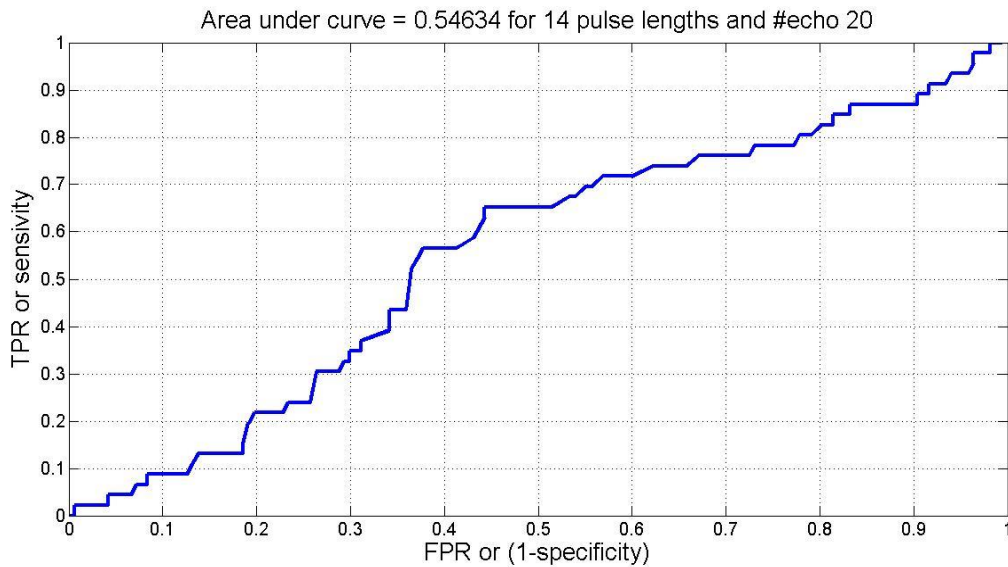


Figure 75: ROC curve for pulse length of 14 and 20 independent echoes

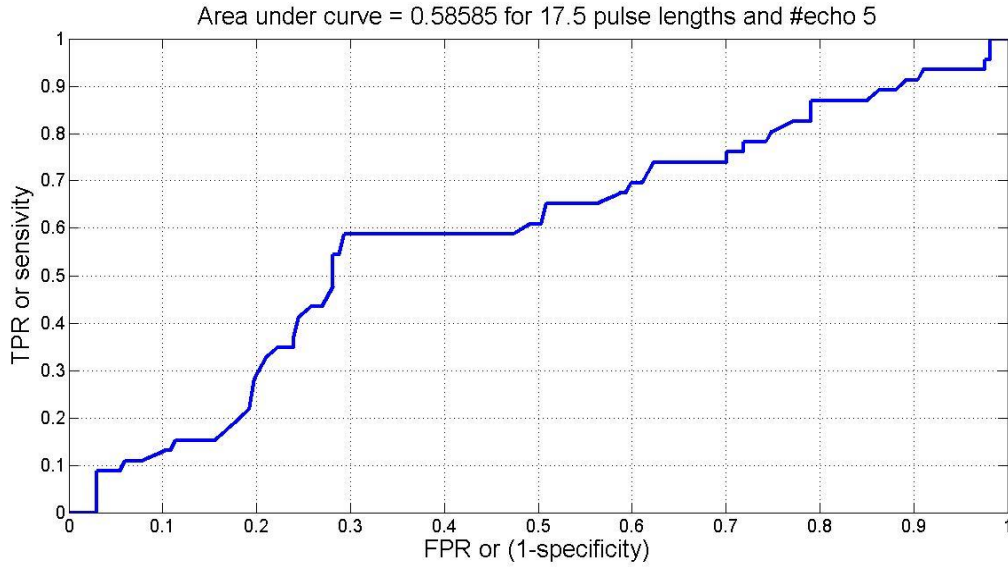


Figure 76: ROC curve for pulse length of 17.5 and 5 independent echoes

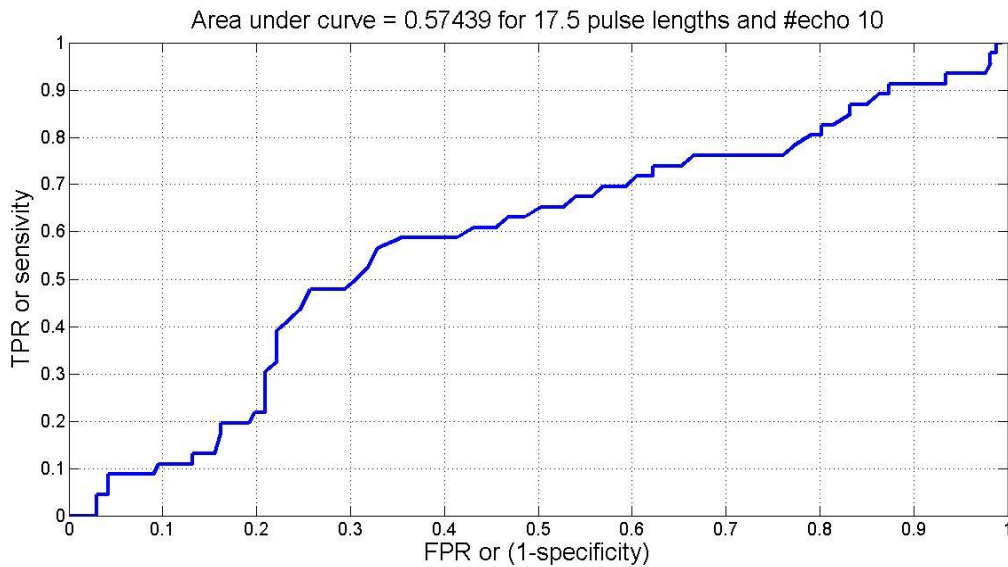


Figure 77: ROC curve for pulse length of 17.5 and 10 independent echoes

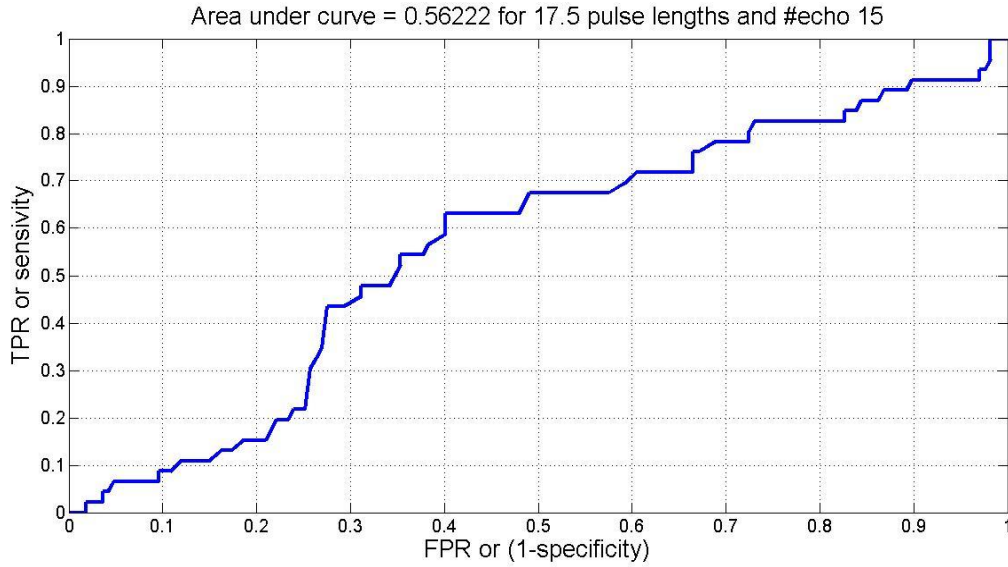


Figure 78: ROC curve for pulse length of 17.5 and 15 independent echoes

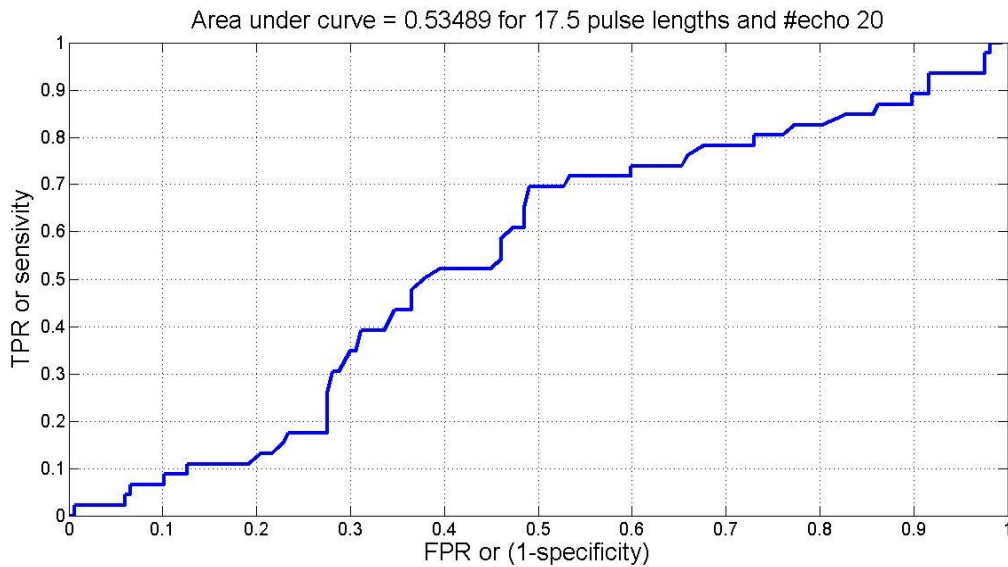


Figure 79: ROC curve for pulse length of 17.5 and 20 independent echoes

Figures for chapter 2 showing ROC curves for the varying pulse lengths and number of echoes for Spectral difference algorithm.

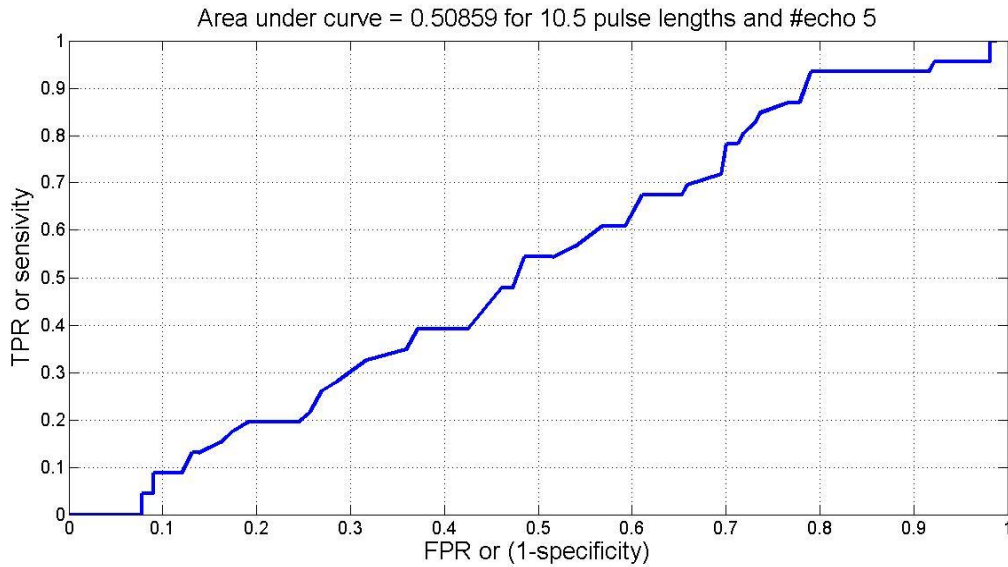


Figure 80: ROC curve for pulse length of 10.5 and 5 independent echoes

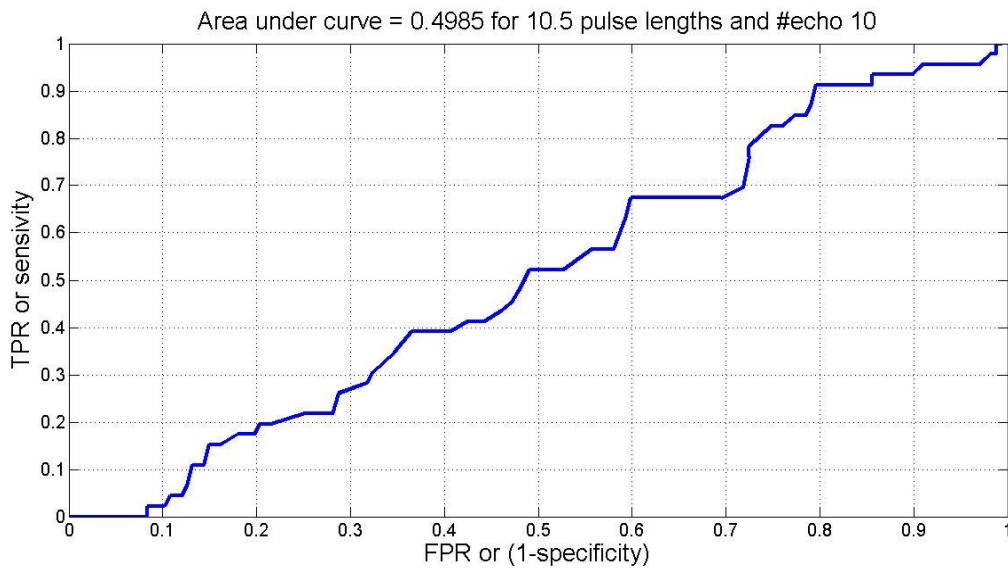


Figure 81: ROC curve for pulse length of 10.5 and 10 independent echoes

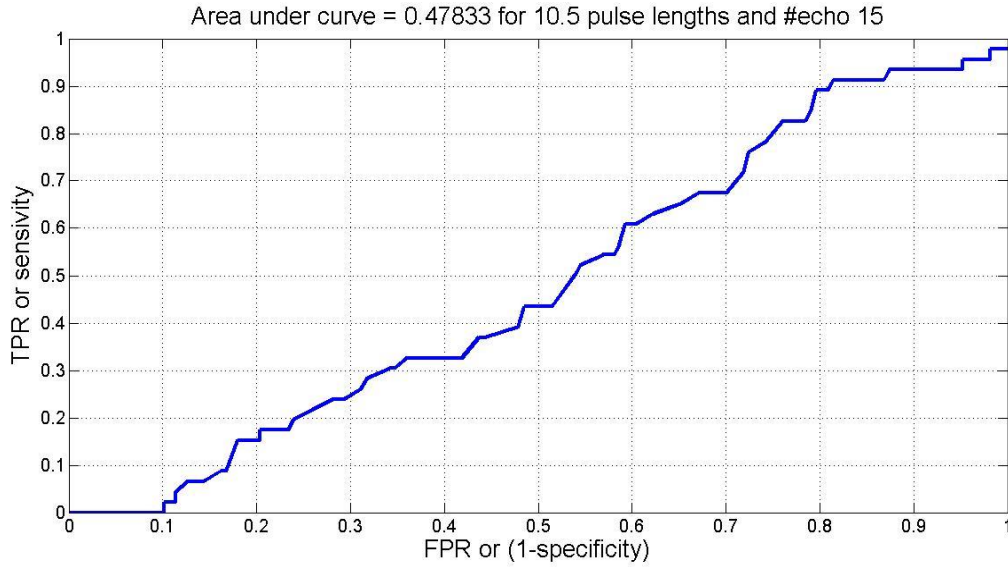


Figure 82: ROC curve for pulse length of 10.5 and 15 independent echoes

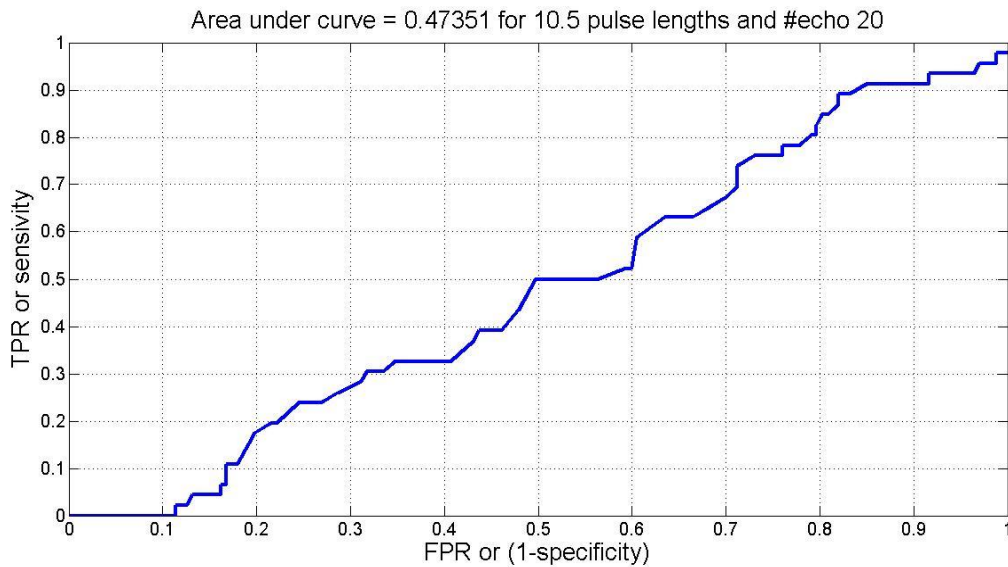


Figure 83: ROC curve for pulse length of 10.5 and 20 independent echoes

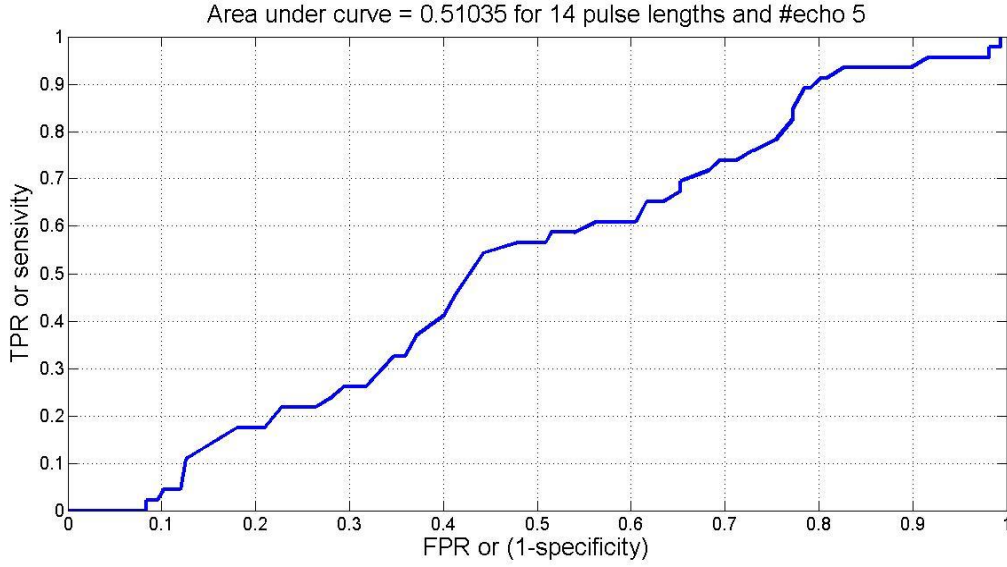


Figure 84: ROC curve for pulse length of 14 and 5 independent echoes

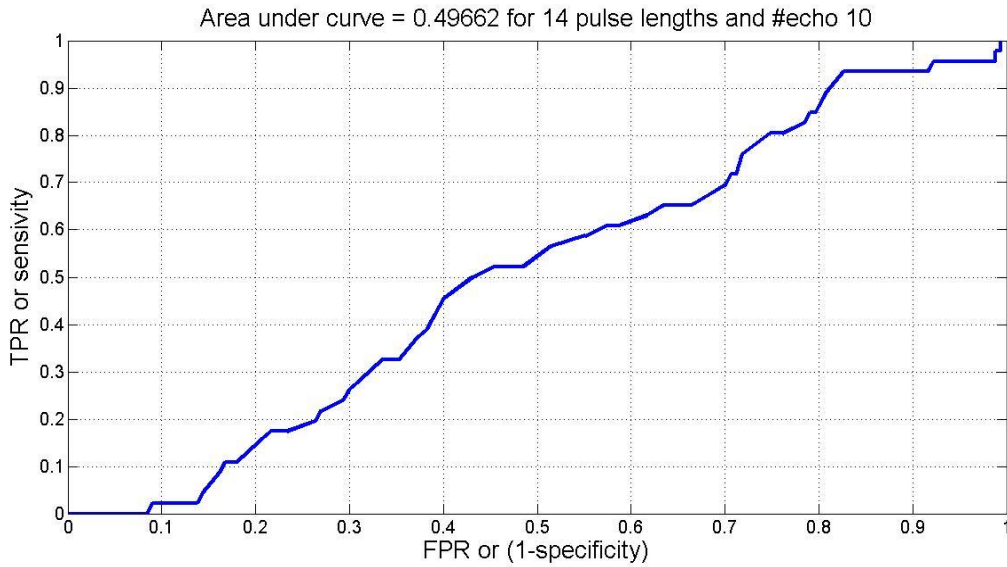


Figure 85: ROC curve for pulse length of 14 and 10 independent echoes

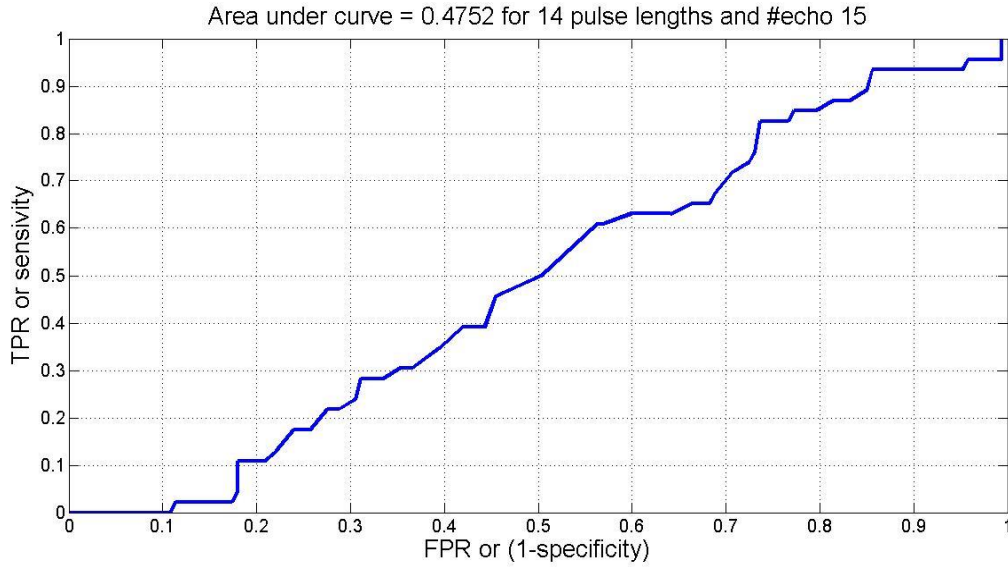


Figure 86: ROC curve for pulse length of 14 and 15 independent echoes

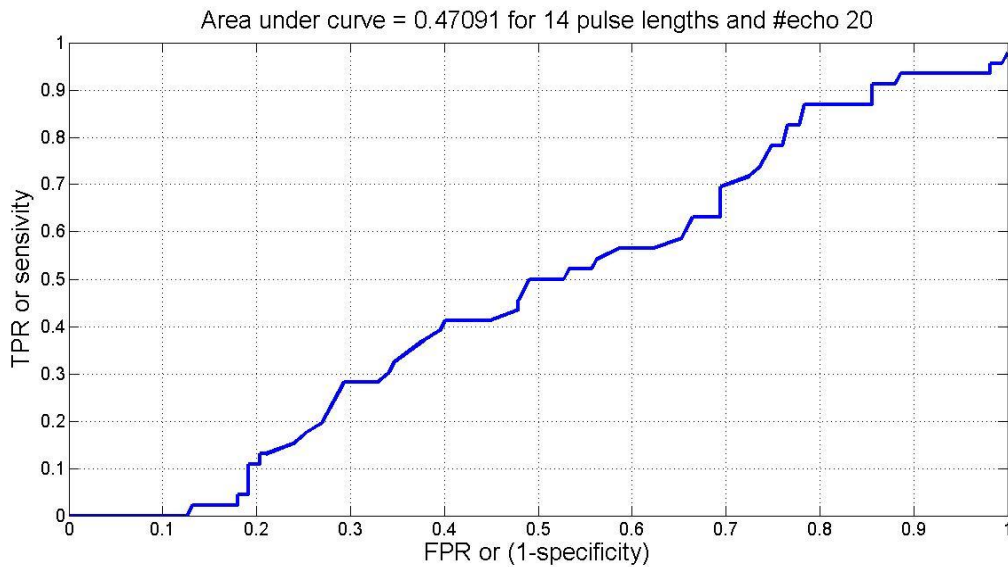


Figure 87: ROC curve for pulse length of 14 and 20 independent echoes

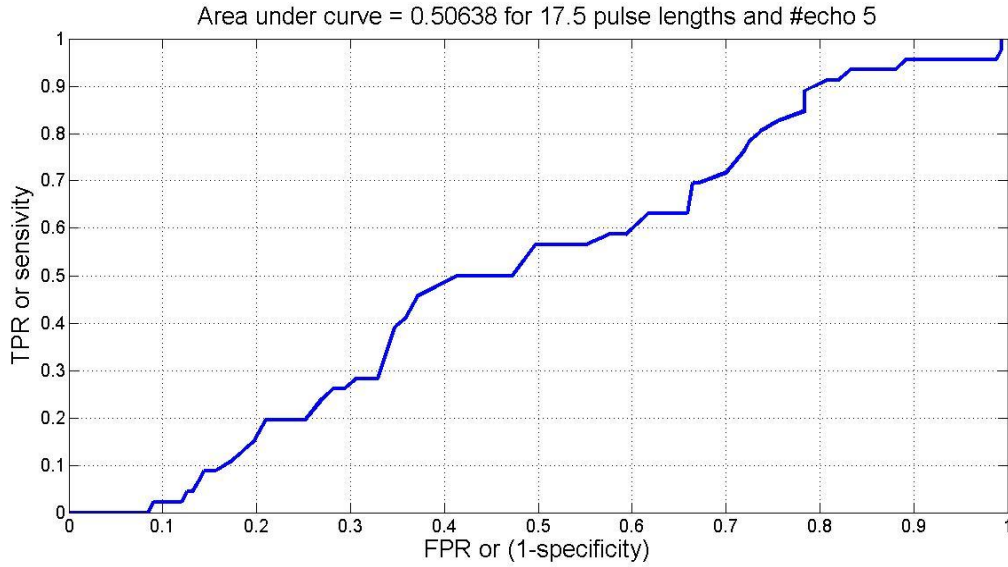


Figure 88: ROC curve for pulse length of 17.5 and 5 independent echoes

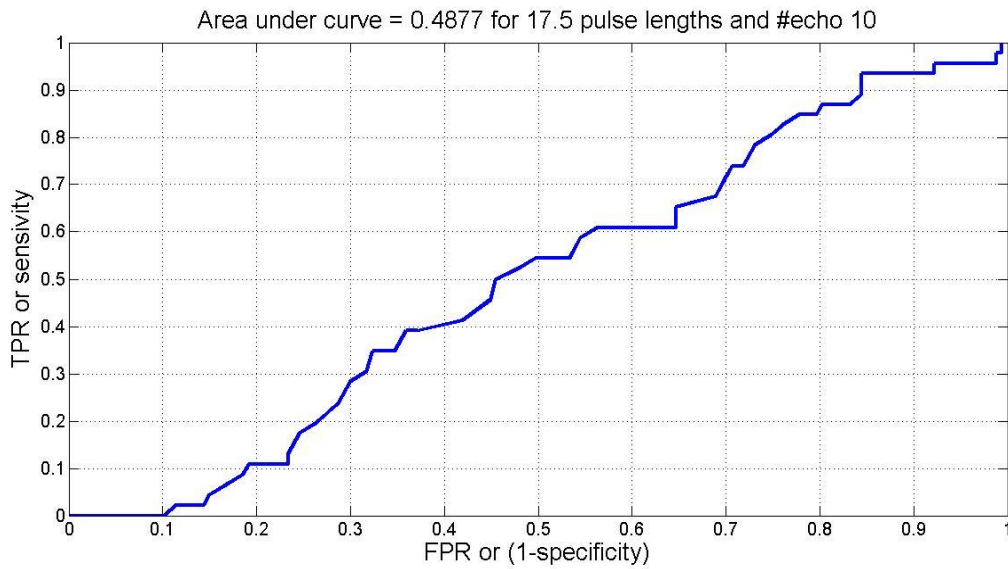


Figure 89: ROC curve for pulse length of 17.5 and 10 independent echoes

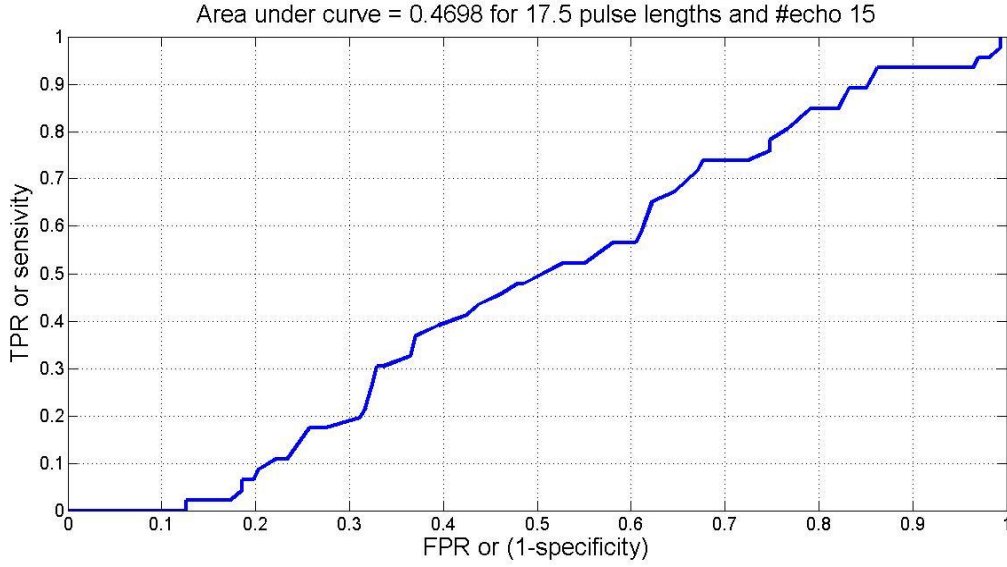


Figure 90: ROC curve for pulse length of 17.5 and 15 independent echoes

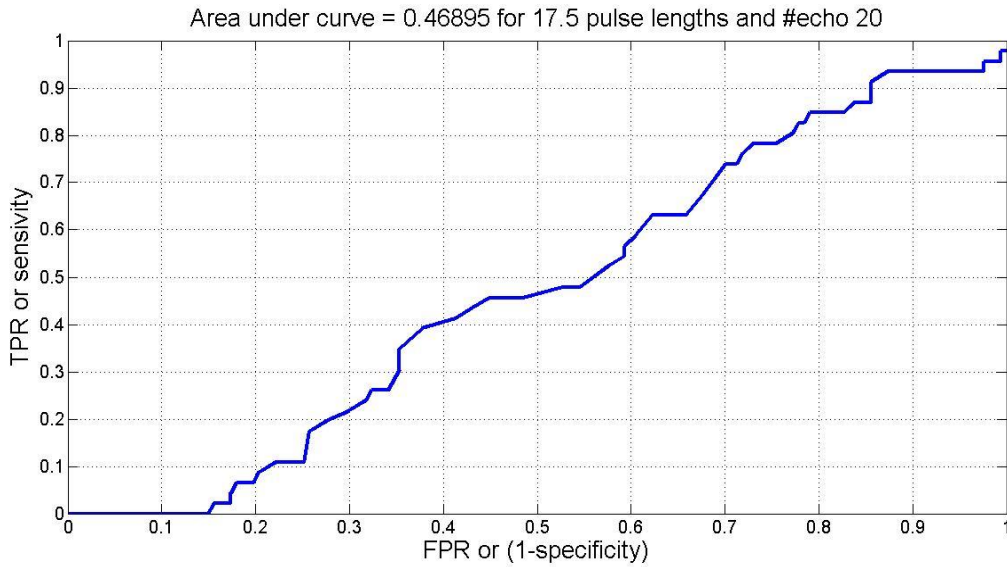


Figure 91: ROC curve for pulse length of 17.5 and 20 independent echoes

Figure for chapter 2 showing ROC values for parameters involving cervical length.

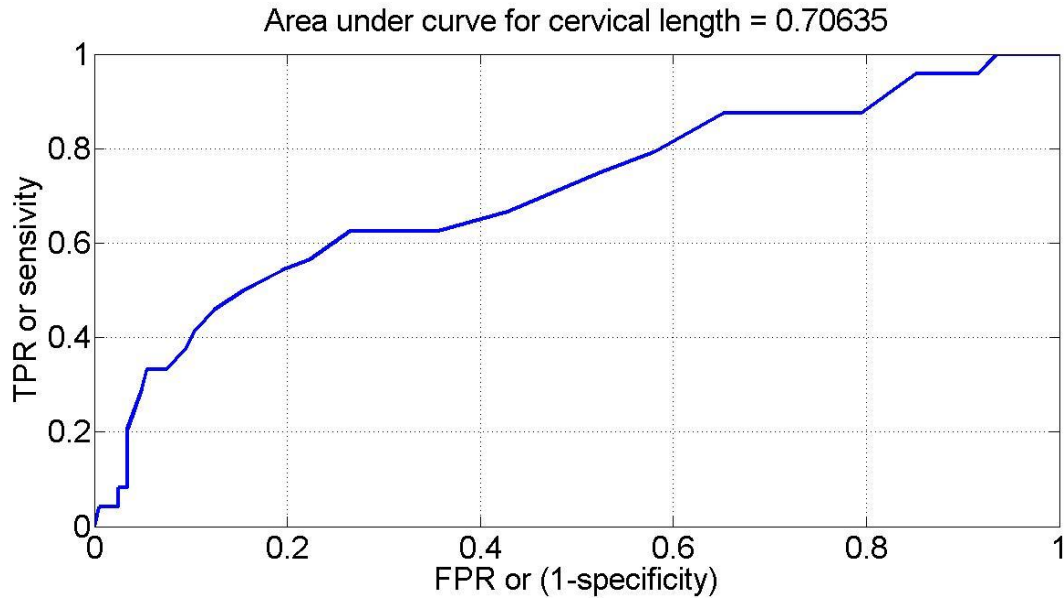


Figure 92: ROC curve for cervical length with cutoff 5 weeks from delivery

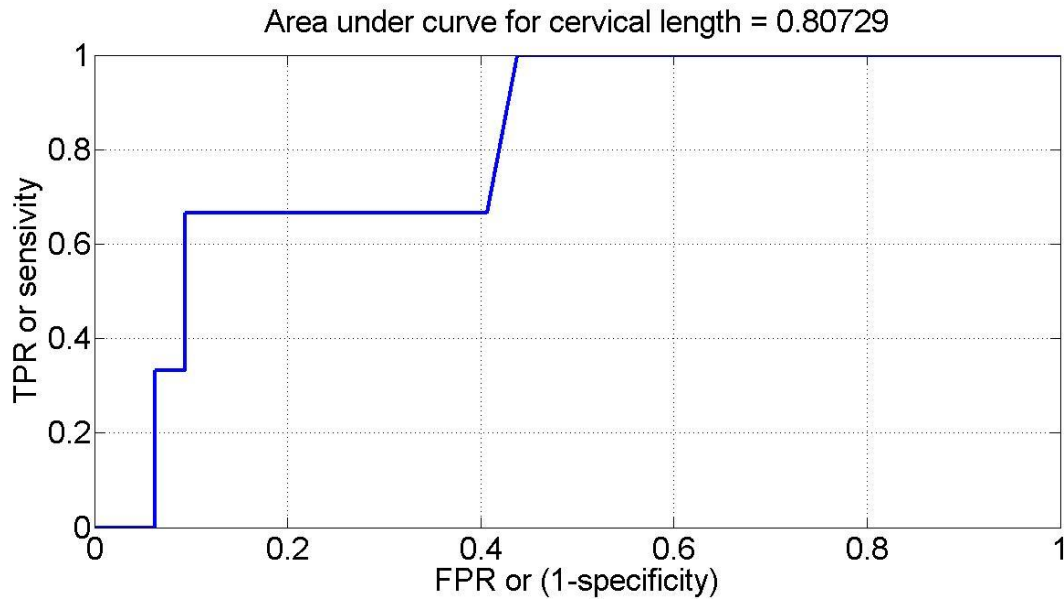


Figure 93: ROC curve for cervical length multiplied by attenuation values with cutoff 5 weeks from delivery.

APPENDIX B

SUPPLEMENTARY PLOTS FOR CHAPTER 4

Figures from chapter 4 showing the results using GMM when restriction on SNR and beta values are applied. The scatter plot shows the attenuation vs time to delivery for the varying pulse length and echo size

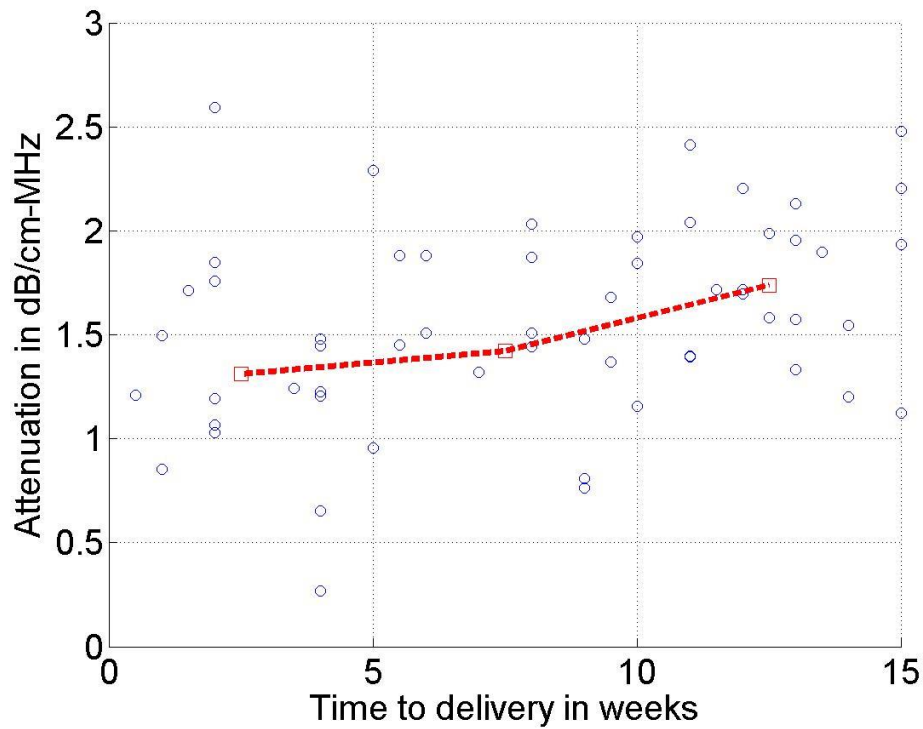


Figure 94: Attenuation vs time to delivery for pulse length of 10.5 and 5 independent echoes

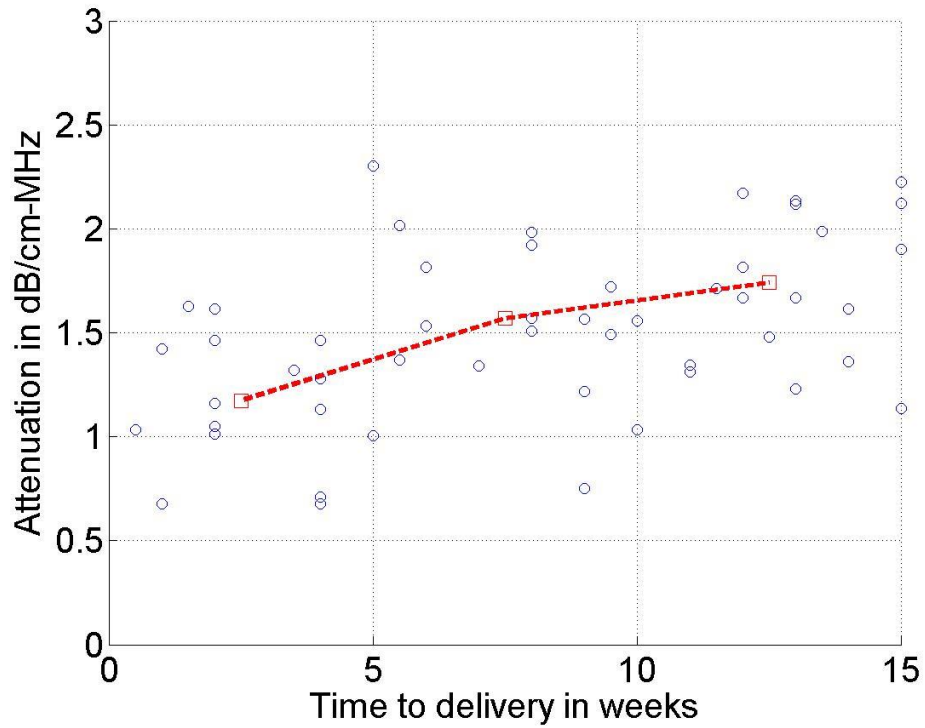


Figure 95: Attenuation vs time to delivery for pulse length of 10.5 and 10 independent echoes

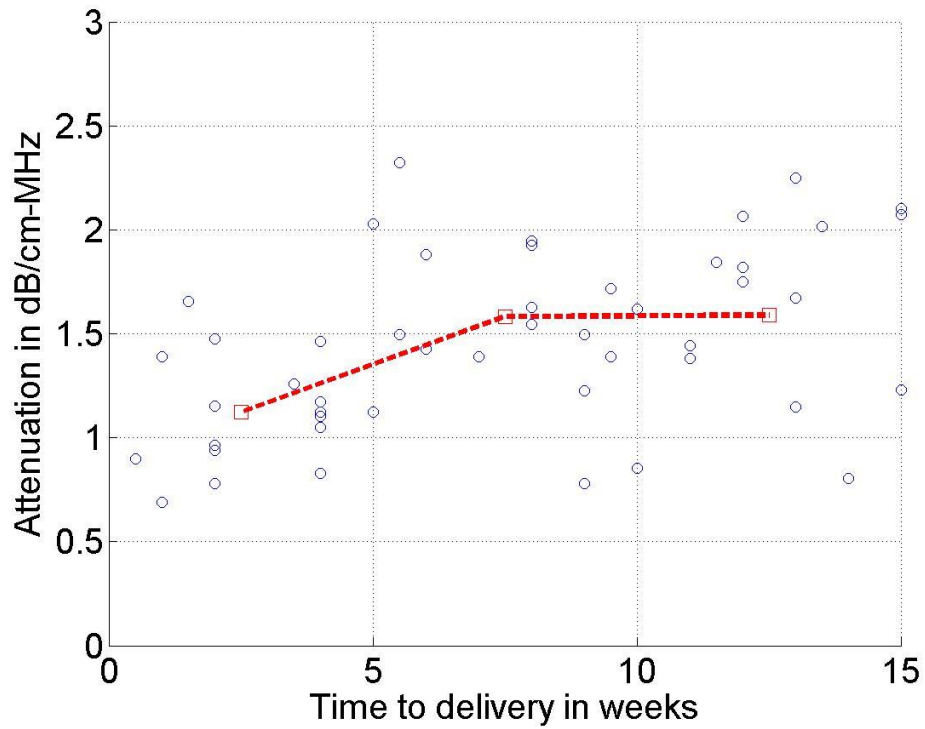


Figure 96: Attenuation vs time to delivery for pulse length of 10.5 and 15 independent echoes

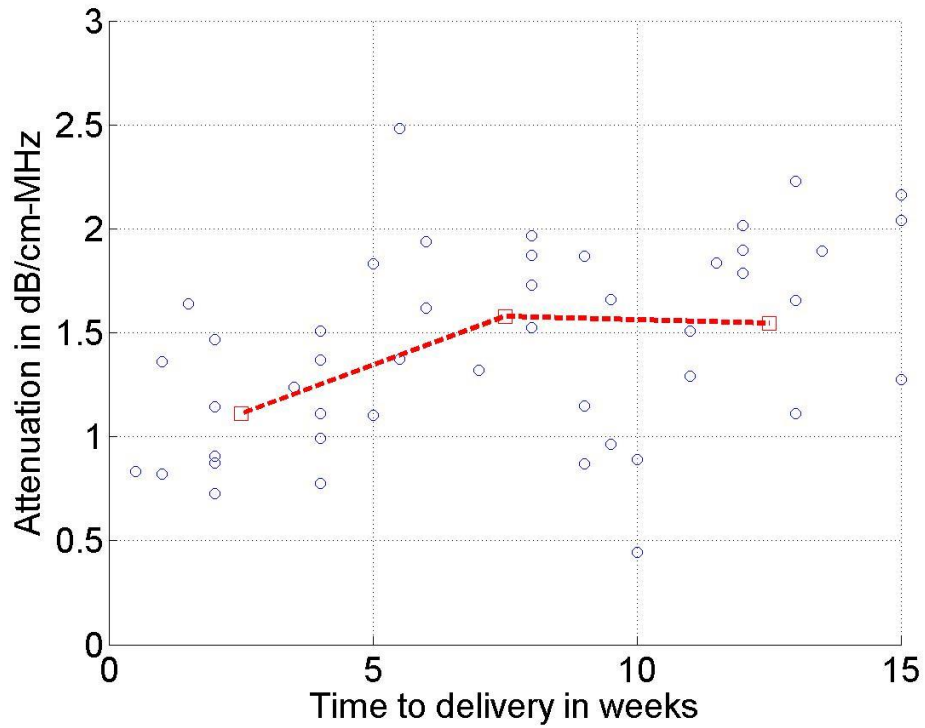


Figure 97: Attenuation vs time to delivery for pulse length of 10.5 and 20 independent echoes

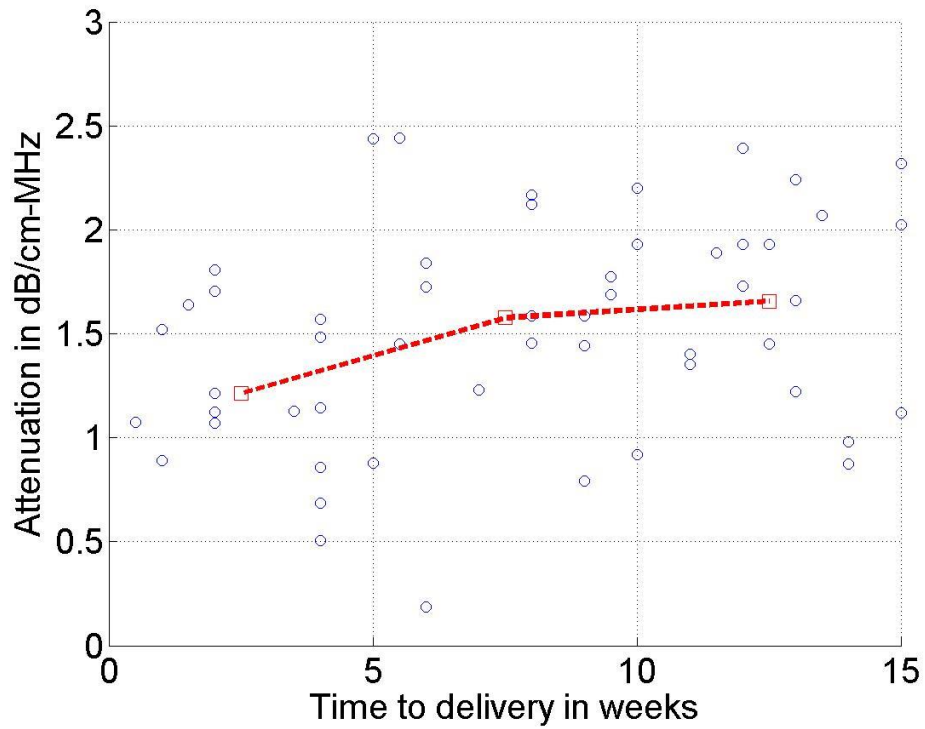


Figure 98: Attenuation vs time to delivery for pulse length of 14 and 5 independent echoes

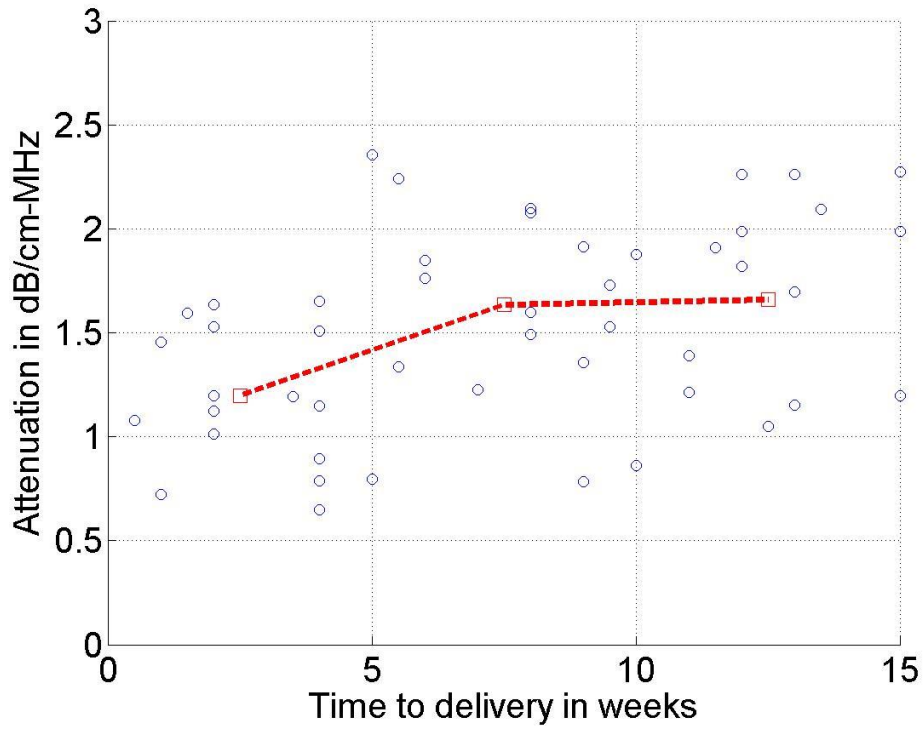


Figure 99: Attenuation vs time to delivery for pulse length of 14 and 10 independent echoes

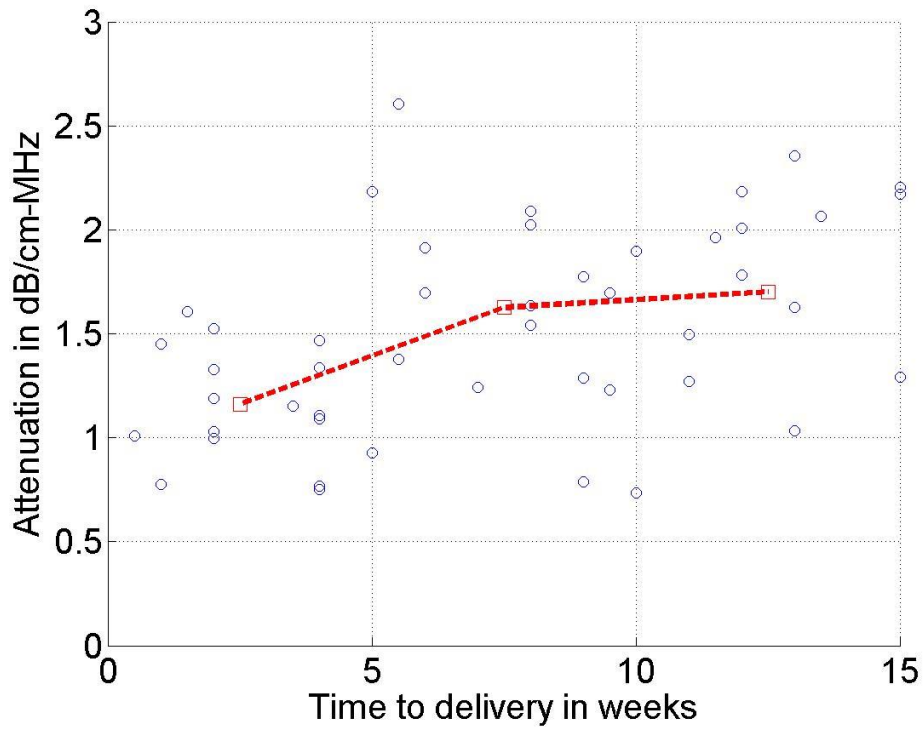


Figure 100: Attenuation vs time to delivery for pulse length of 14 and 15 independent echoes

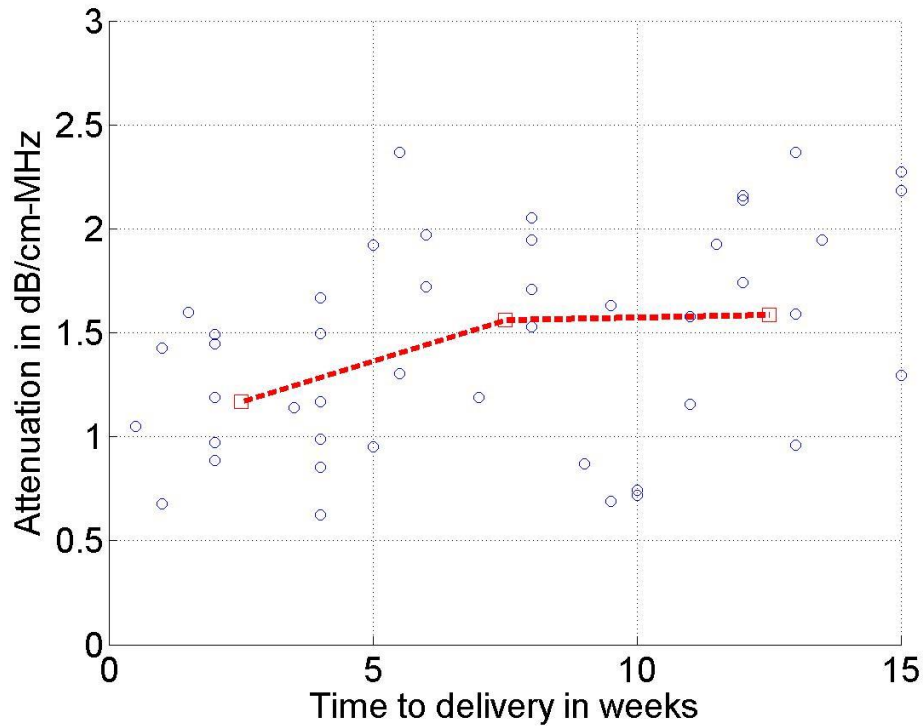


Figure 101: Attenuation vs time to delivery for pulse length of 14 and 20 independent echoes

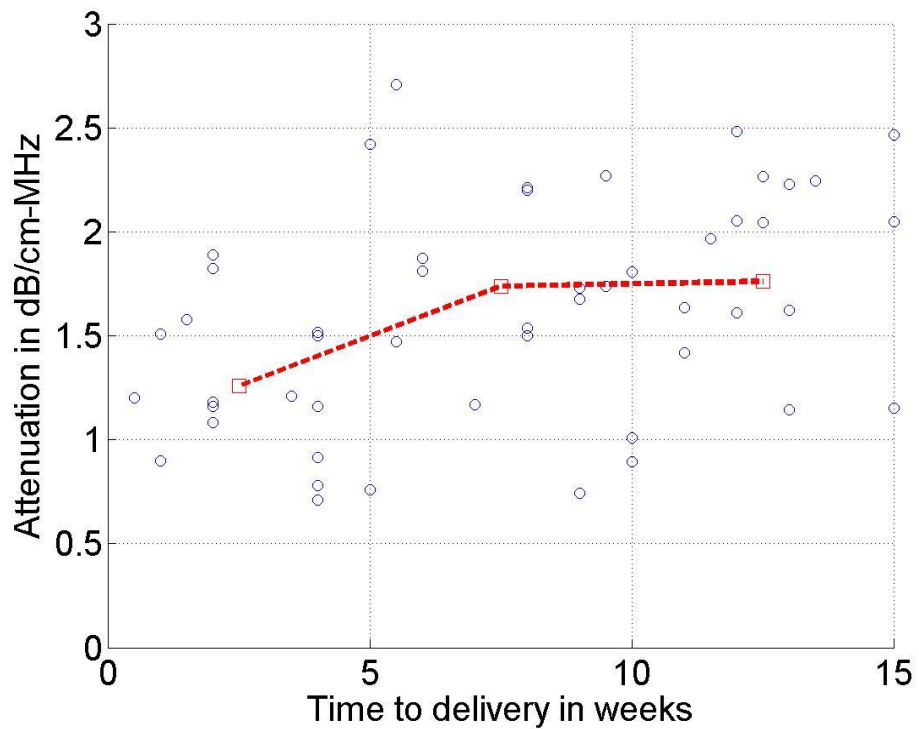


Figure 102: Attenuation vs time to delivery for pulse length of 17.5 and 5 independent echoes

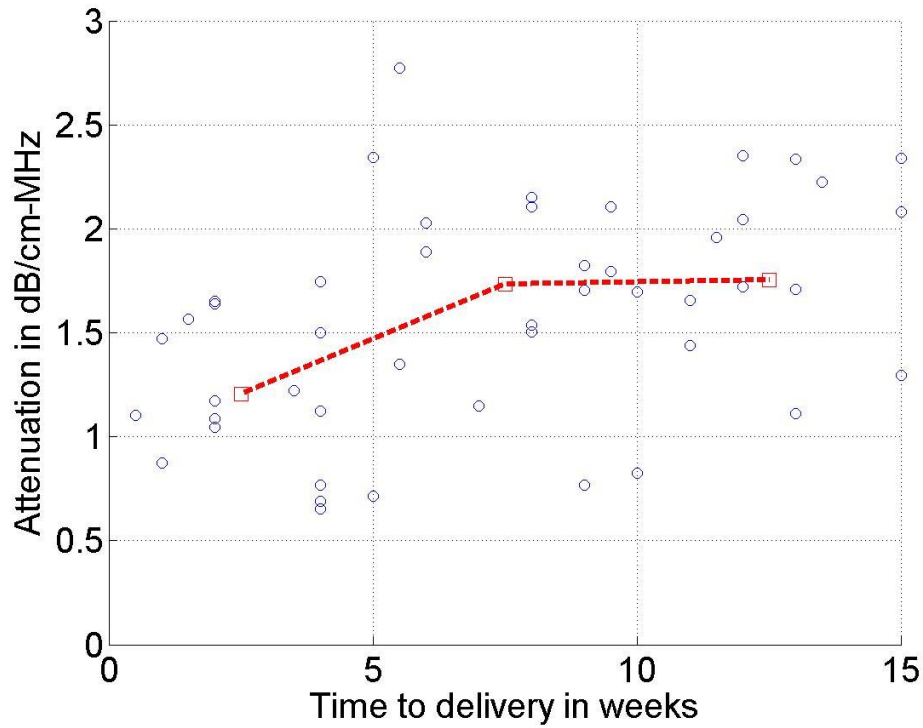


Figure 103: Attenuation vs time to delivery for pulse length of 17.5 and 10 independent echoes

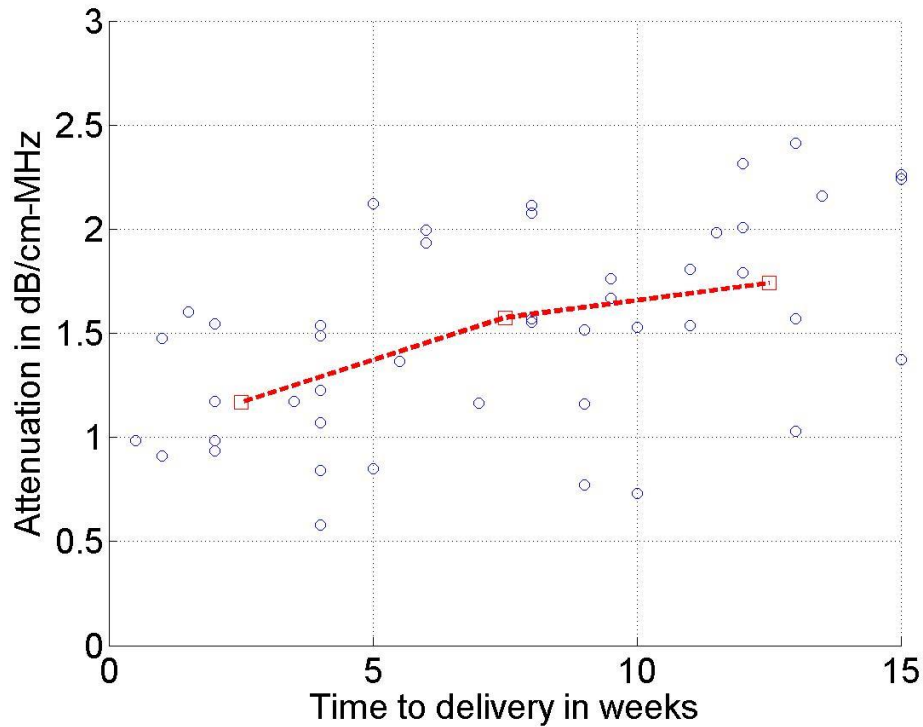


Figure 104: Attenuation vs time to delivery for pulse length of 17.5 and 15 independent echoes

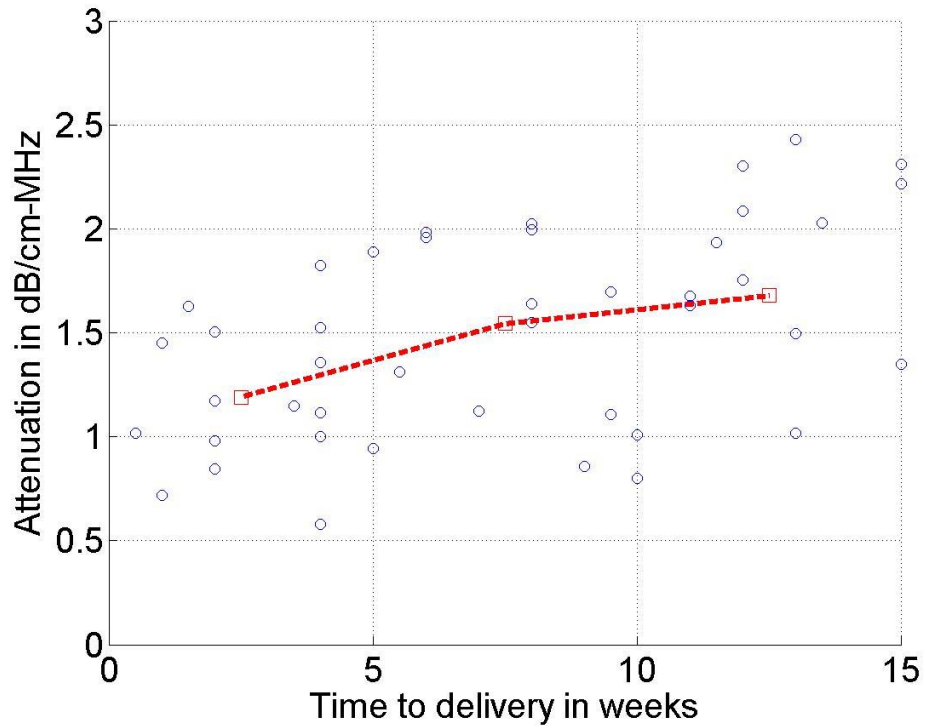


Figure 105: Attenuation vs time to delivery for pulse length of 17.5 and 20 independent echoes

Figures from chapter 4 showing the results using GMM along with restriction on SNR and beta values. The ROC curve quantify the results in a measurable way.

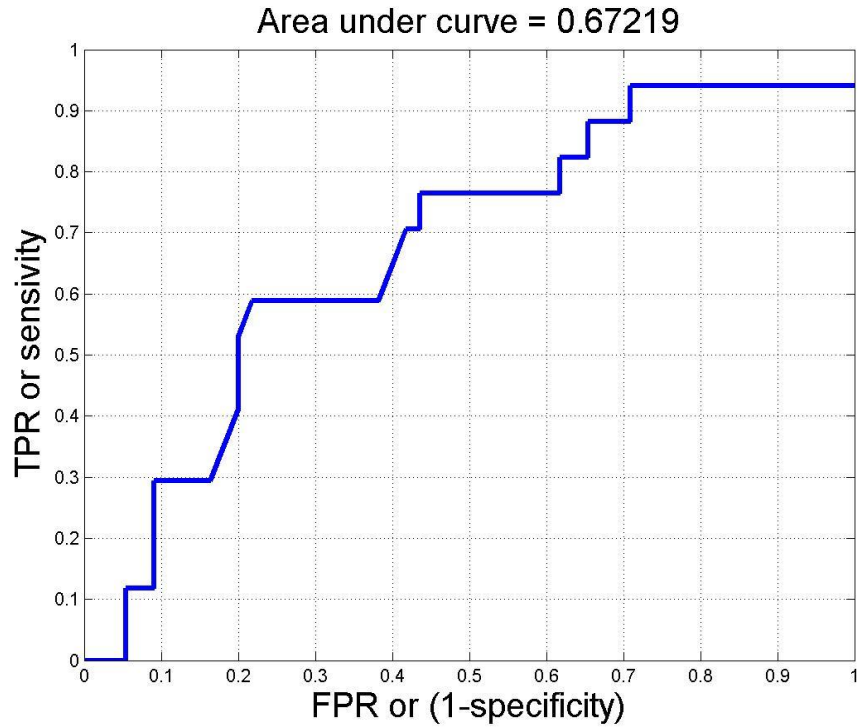


Figure 106: ROC curve for pulse length of 10.5 and 5 independent echoes

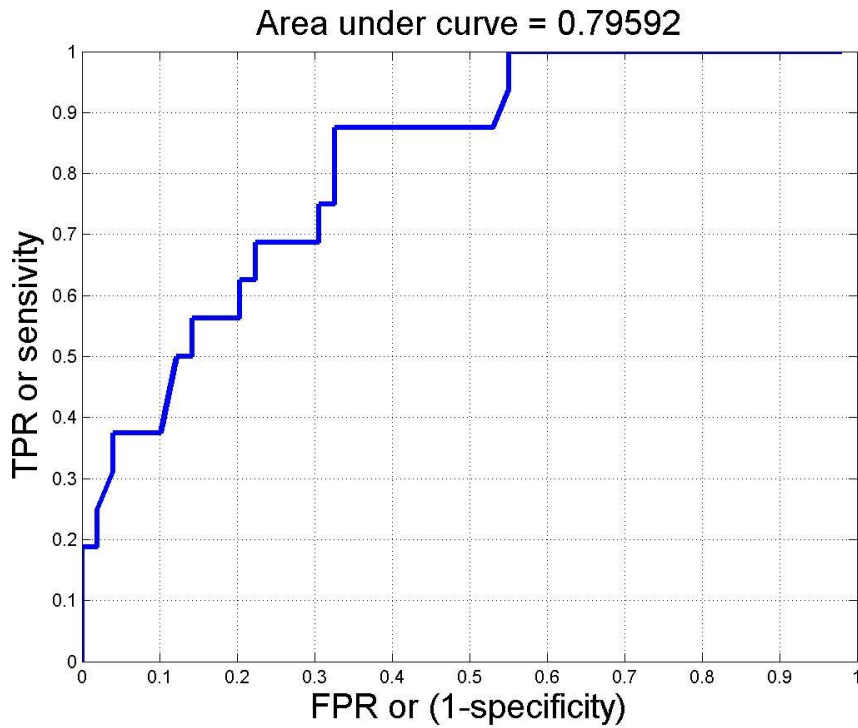


Figure 107: ROC curve for pulse length of 10.5 and 10 independent echoes

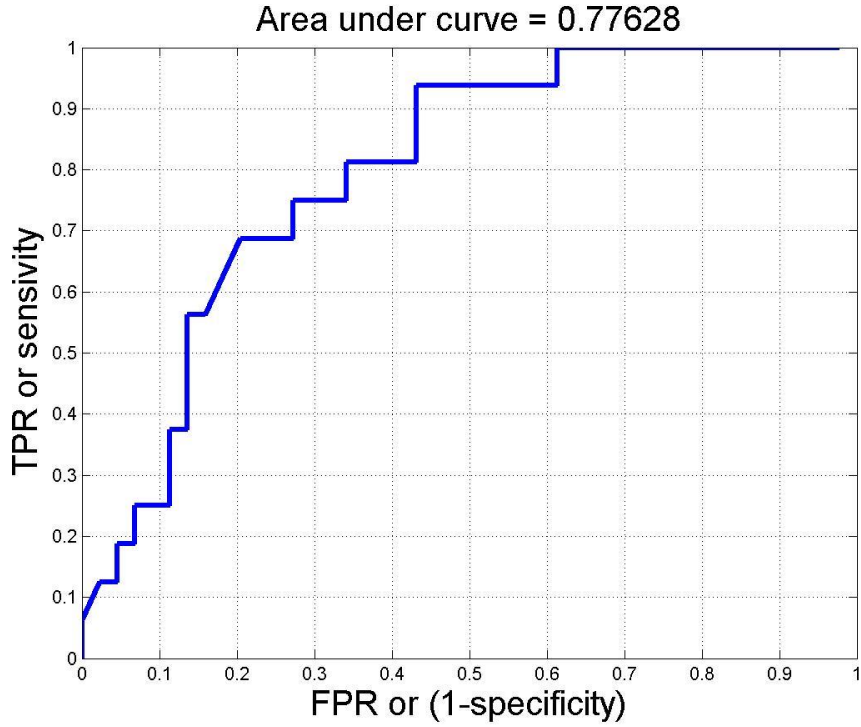


Figure 108: ROC curve for pulse length of 10.5 and 15 independent echoes

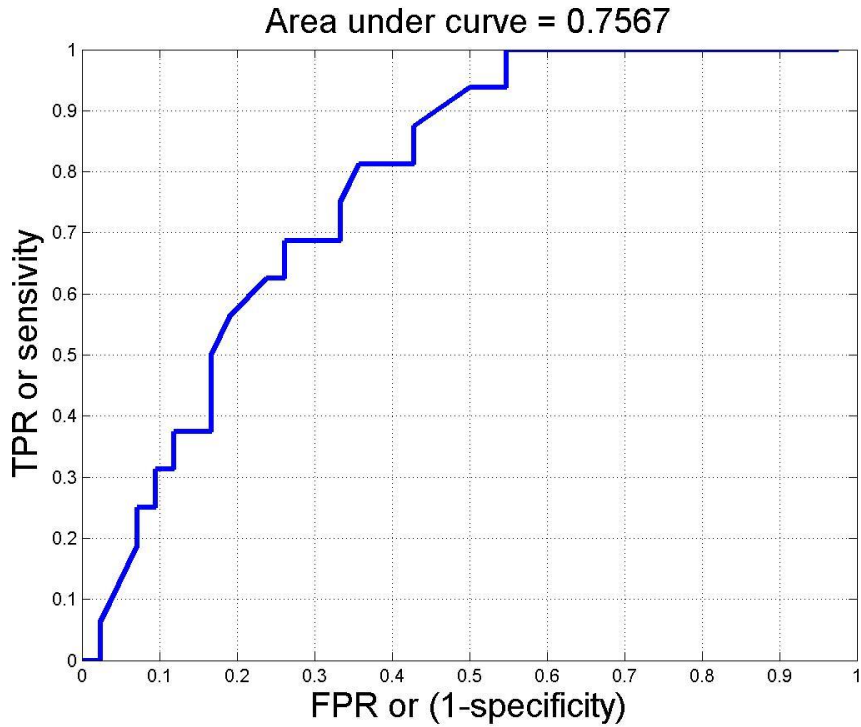


Figure 109: ROC curve for pulse length of 10.5 and 20 independent echoes

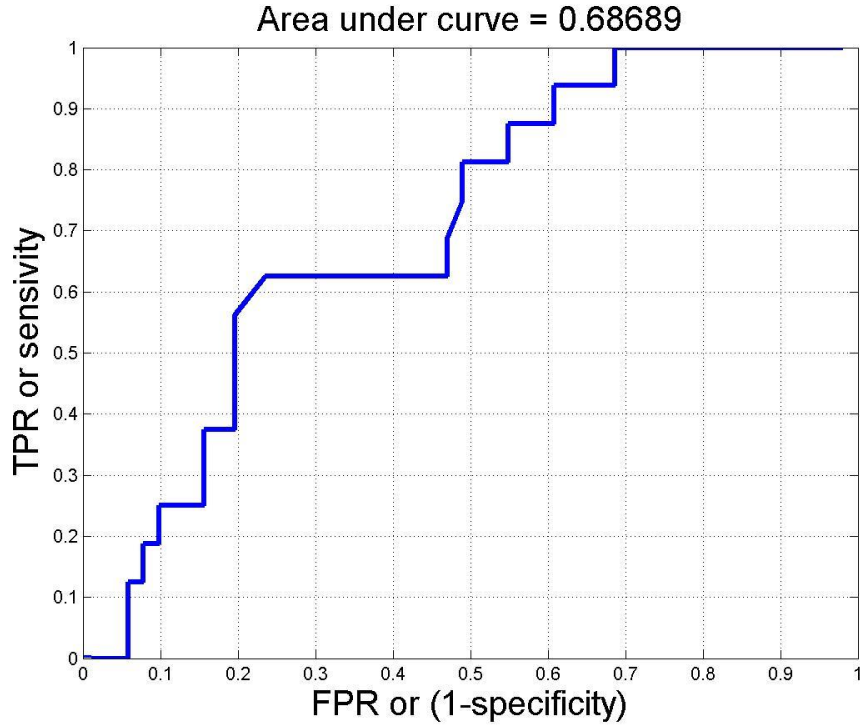


Figure 110: ROC curve for pulse length of 14 and 5 independent echoes

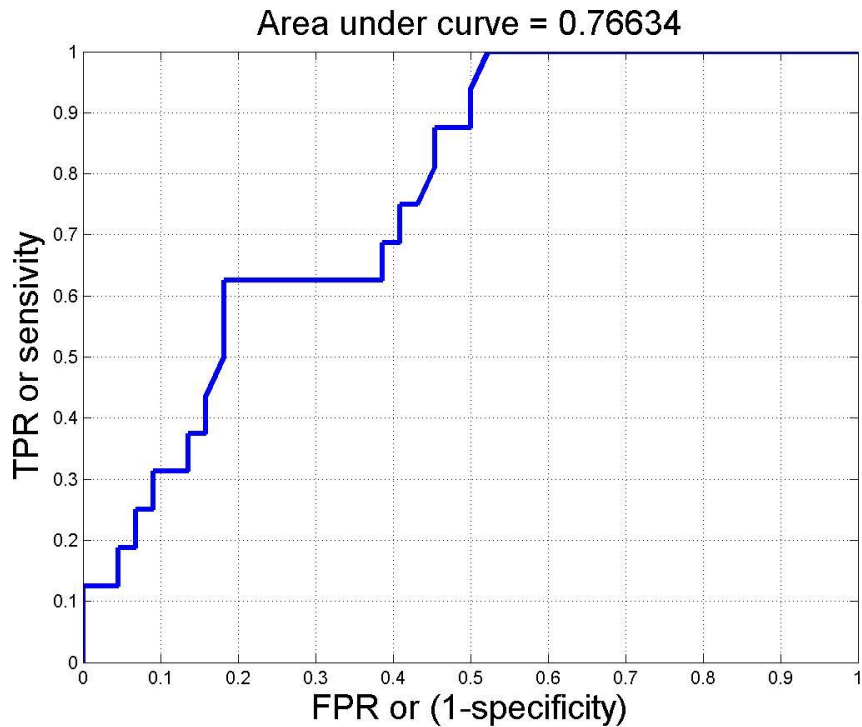


Figure 111: ROC curve for pulse length of 14 and 10 independent echoes

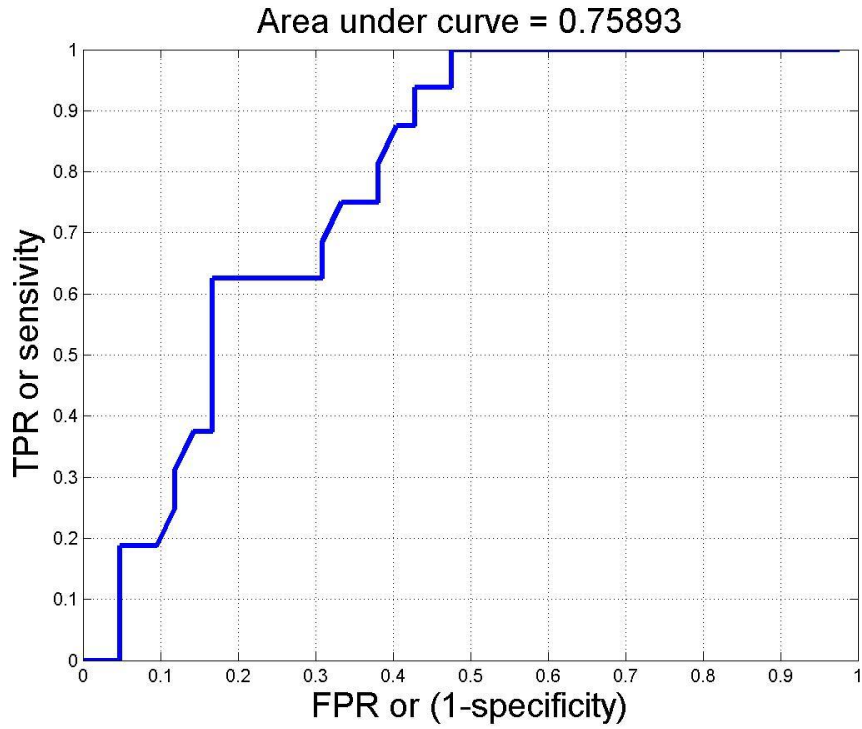


Figure 112: ROC curve for pulse length of 14 and 15 independent echoes

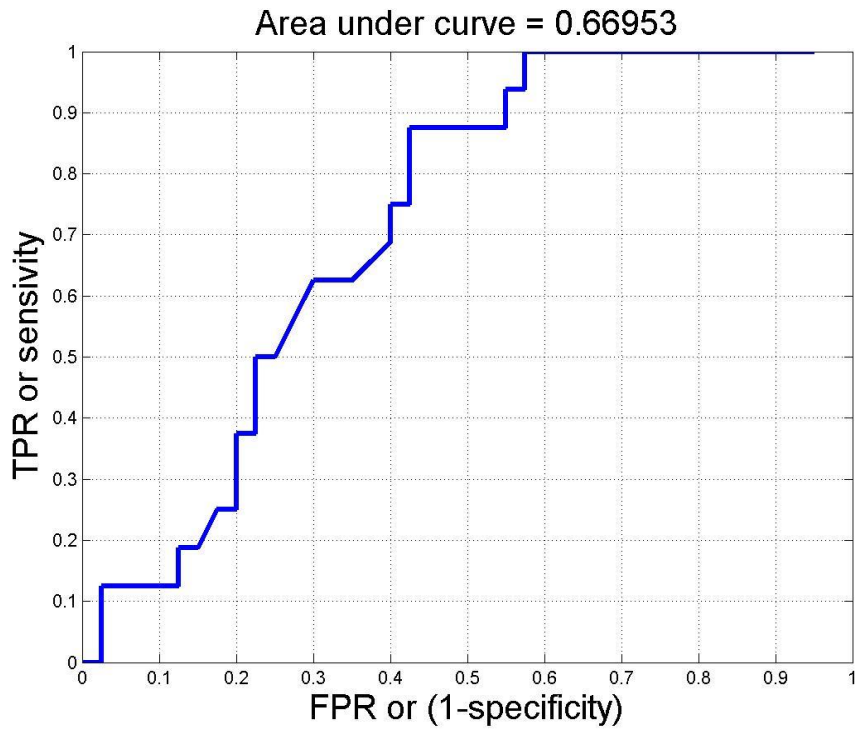


Figure 113: ROC curve for pulse length of 14 and 20 independent echoes

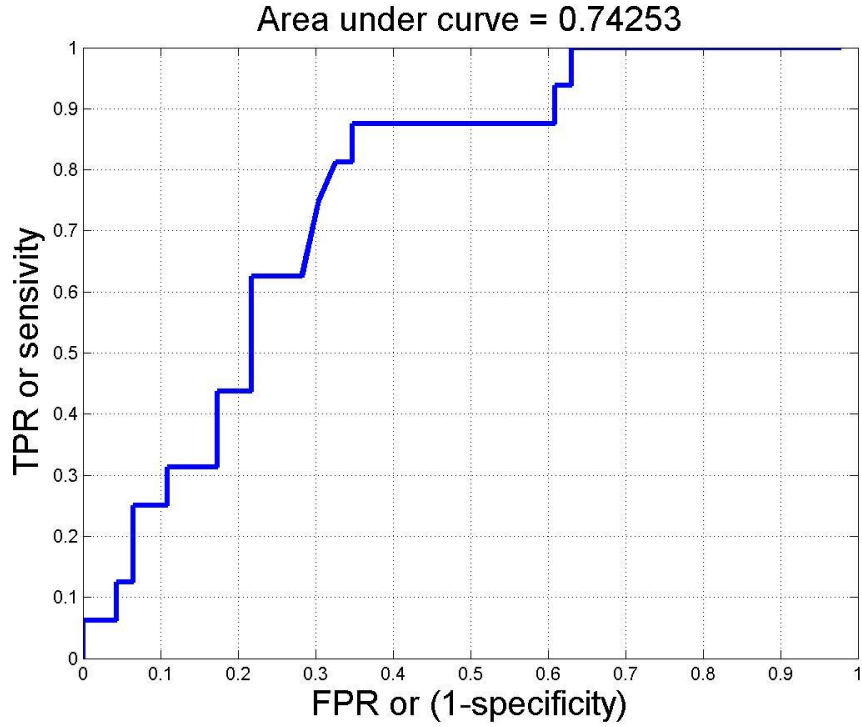


Figure 114: ROC curve for pulse length of 17.5 and 5 independent echoes

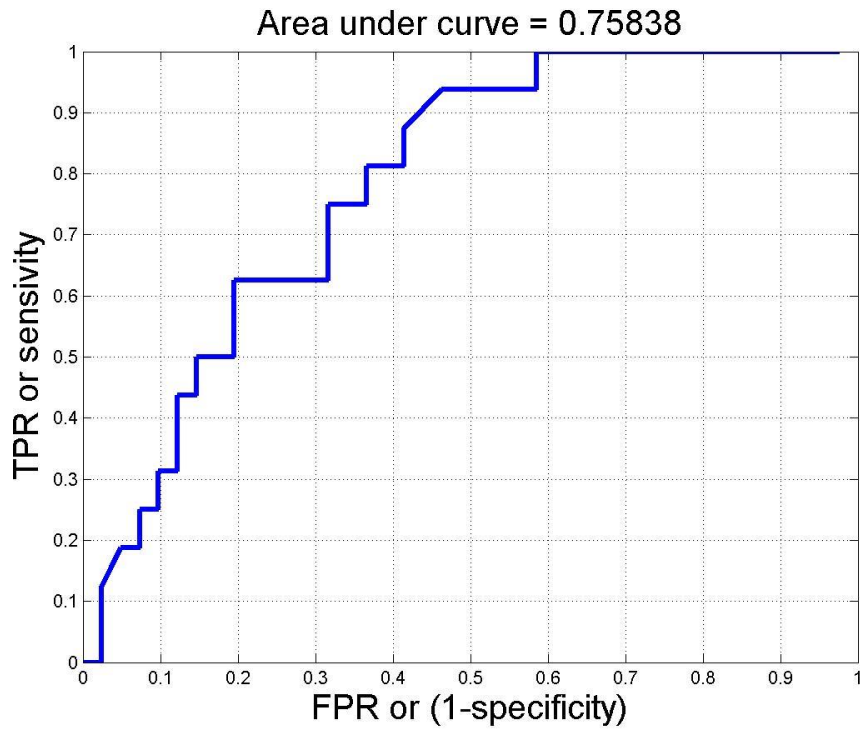


Figure 115: ROC curve for pulse length of 17.5 and 10 independent echoes

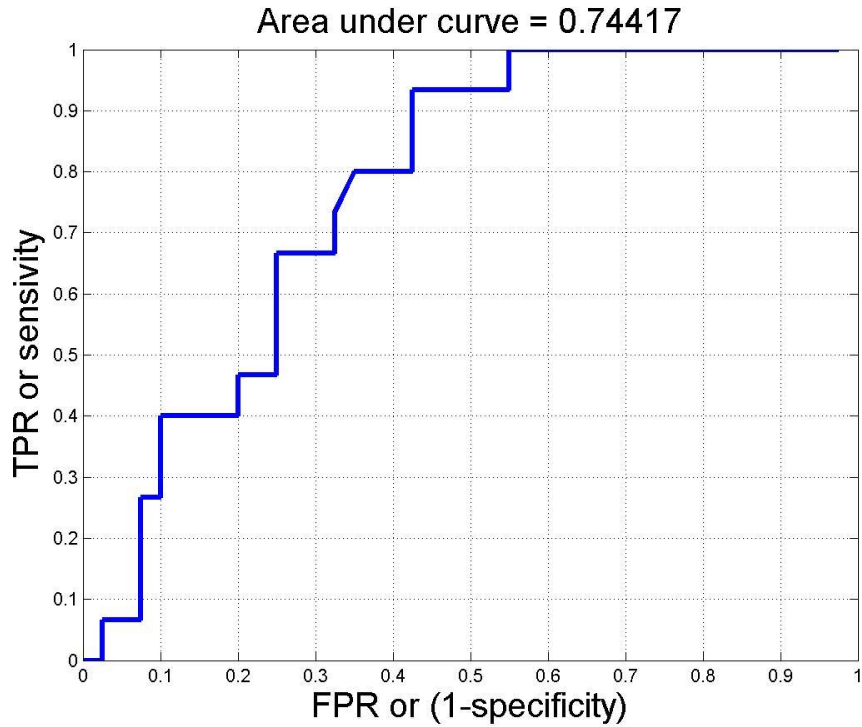


Figure 116: ROC curve for pulse length of 17.5 and 15 independent echoes

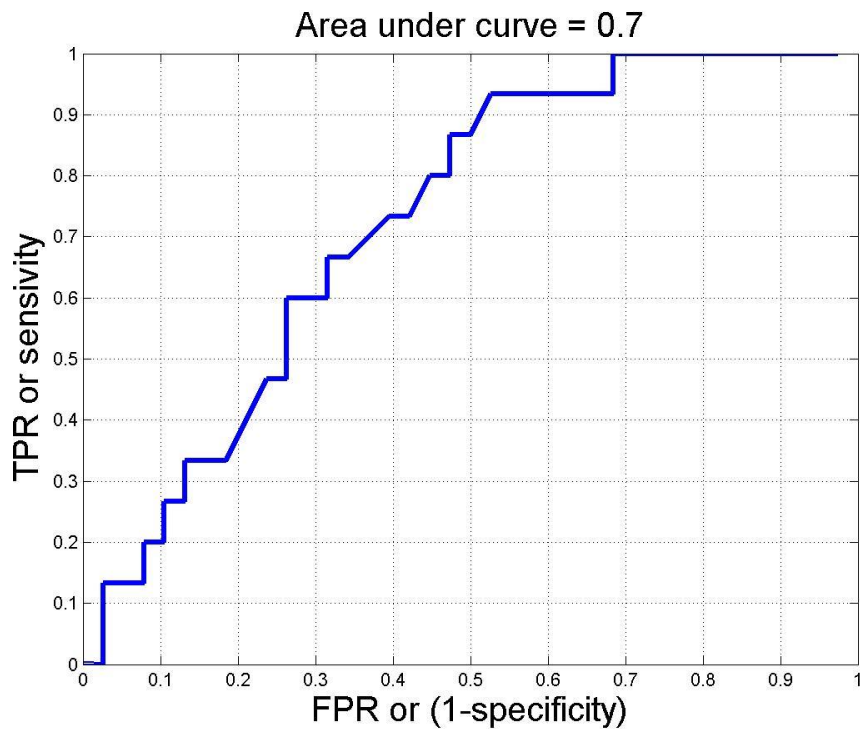


Figure 117: ROC curve for pulse length of 17.5 and 20 independent echoes

APPENDIX C

COMPARISON ON PER PATIENT BASIS

Figures comparing the results from chapter 2 study (attenuation only) vs chapter 4 (attenuation along with GMM and restriction on alpha and beta).

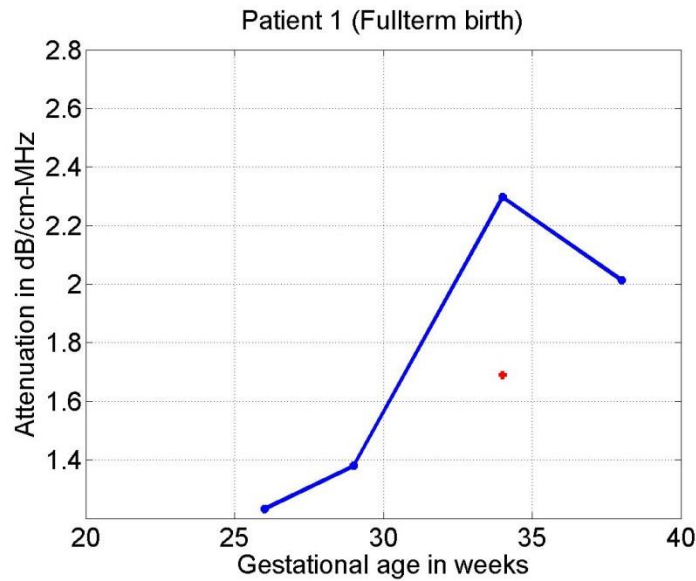


Figure 118: Attenuation vs gestation age for patient 1. Age of the patient is 42. Patient had a history of 2 full term, 0 preterm, and 1 abortion.

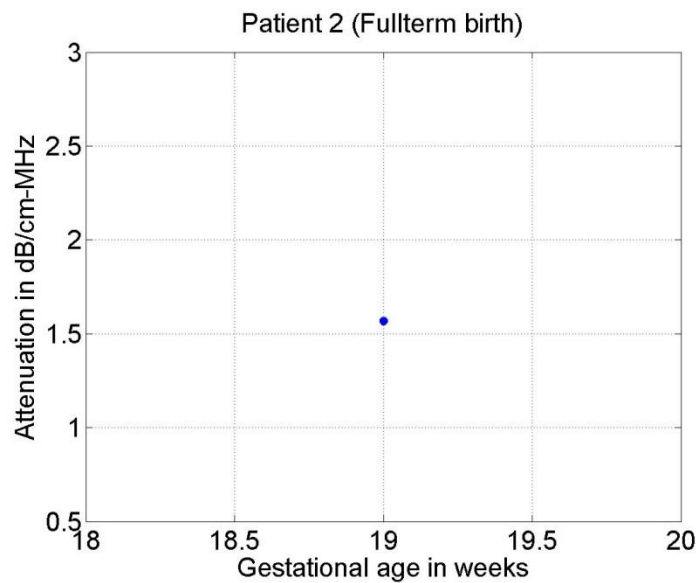


Figure 119: Attenuation vs gestation age for patient 2. Age of the patient is 25. Patient had a history of 2 full term, 1 preterm, and 0 abortion.

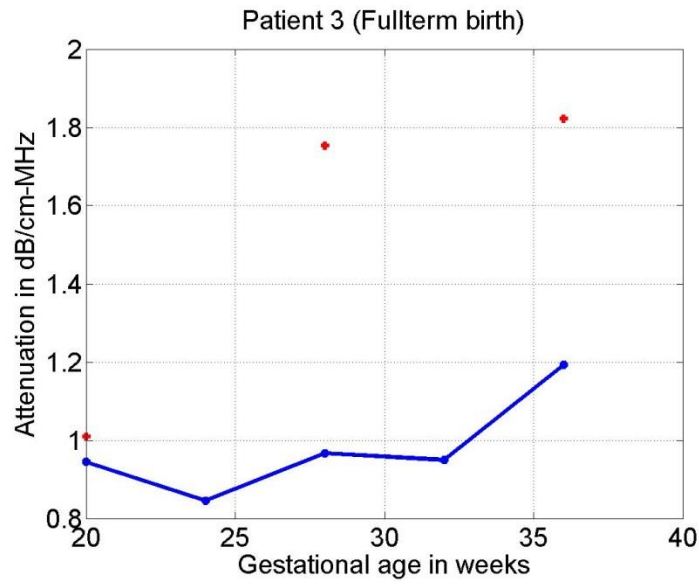


Figure 120: Attenuation vs gestation age for patient 3. Age of the patient is 24. Patient had a history of 2 full term, 0 preterm, and 1 abortion.

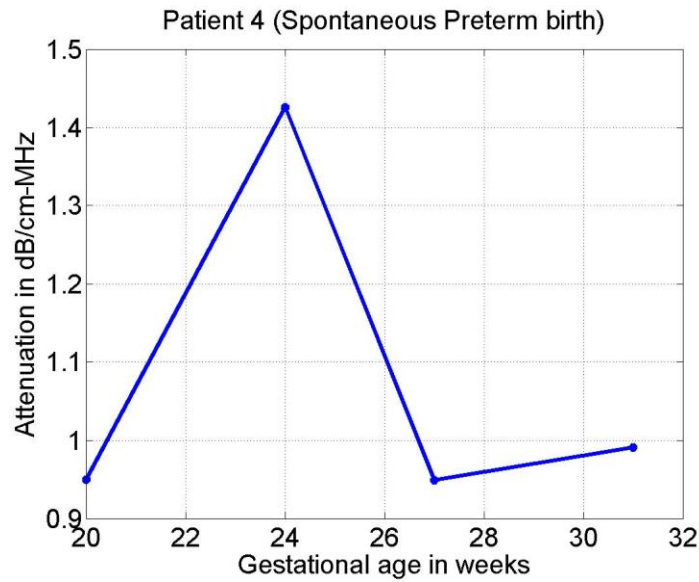


Figure 121: Attenuation vs gestation age for patient 4. Age of the patient is 19. Patient had a history of 1 full term, 0 preterm, and 0 abortion.

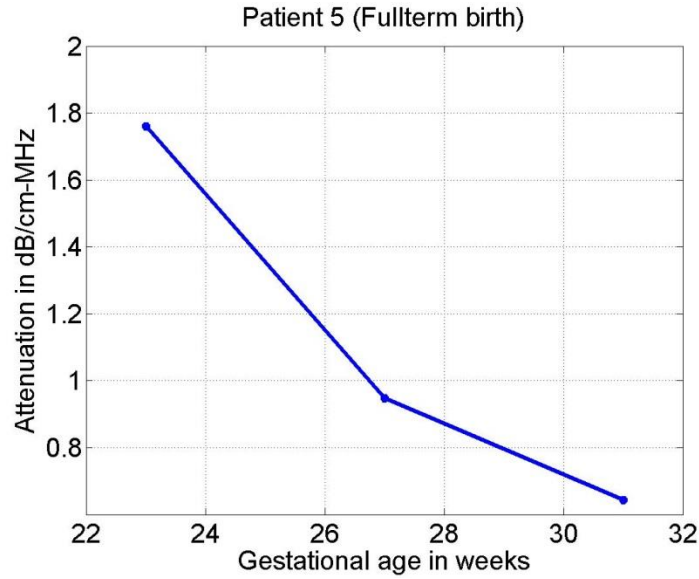


Figure 122: Attenuation vs gestation age for patient 5. Age of the patient is 20. Patient had a history of 0 full term, 0 preterm, and 3 abortions.

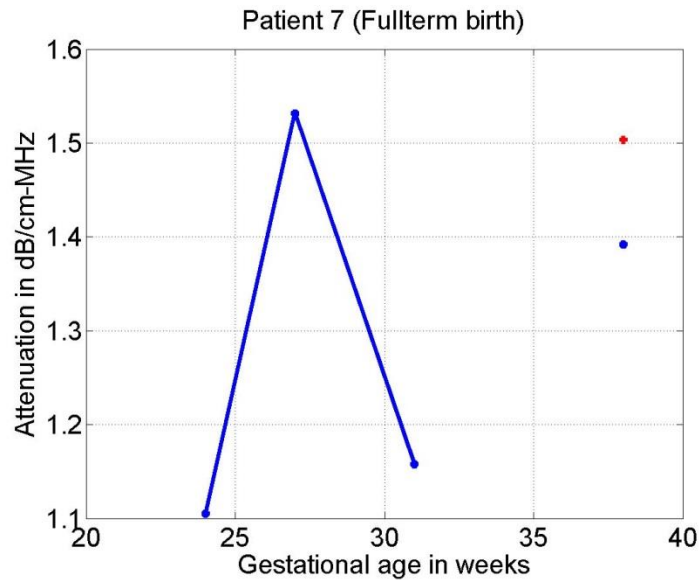


Figure 123: Attenuation vs gestation age for patient 7. Age of the patient is 30. Patient had a history of 1 full term, 0 preterm, and 1 abortion.

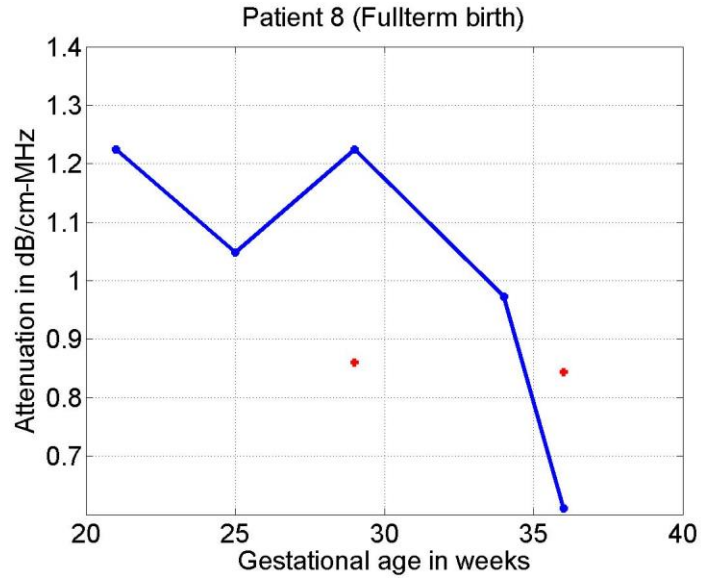


Figure 124: Attenuation vs gestation age for patient 8. Age of the patient is 24. Patient had a history of 4 full term, 2 preterm, 0 abortion.

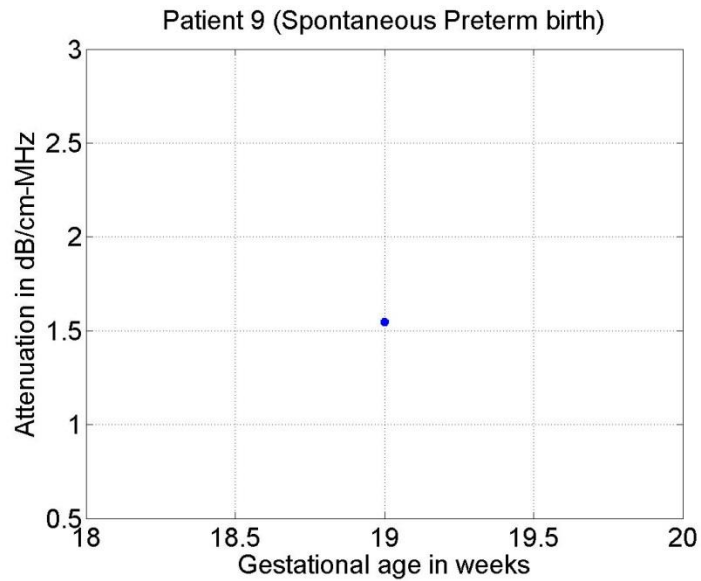


Figure 125: Attenuation vs gestation age for patient 9. Age of the patient is 33. Patient had a history of 0 full term, 2 preterm, 1 abortion.

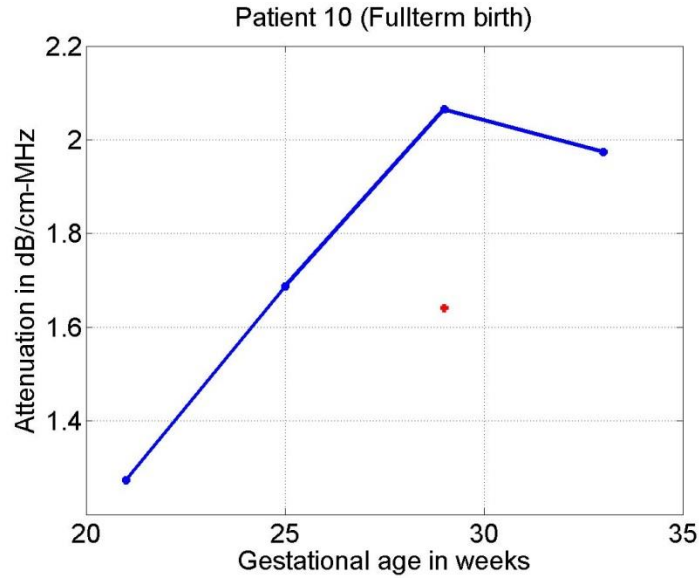


Figure 126: Attenuation vs gestation age for patient 10. Age of the patient is 33. Patient had a history of 5 full term, 1 preterm, and 1 abortion.

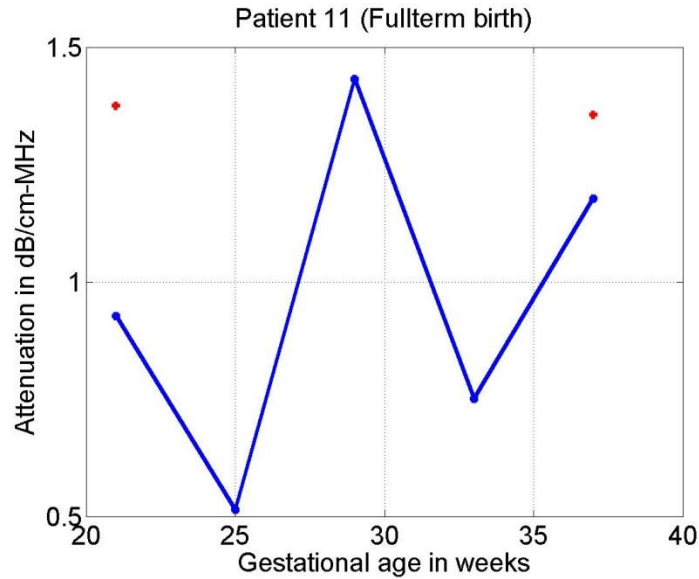


Figure 127: Attenuation vs gestation age for patient 11. Age of the patient is 21. Patient had a history of 1 full term, 1 preterm, 2 abortions.

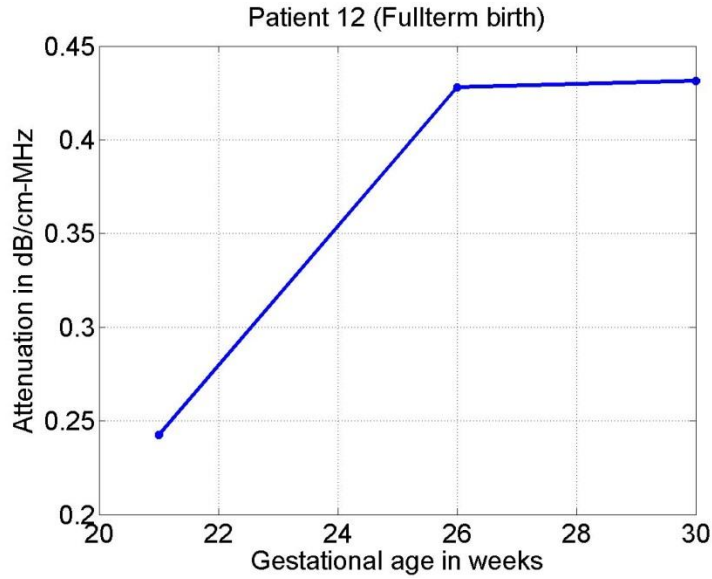


Figure 128: Attenuation vs gestation age for patient 12. Age of the patient is 33. Patient had a history of 0 full term, 0 preterm, and 0 abortion.

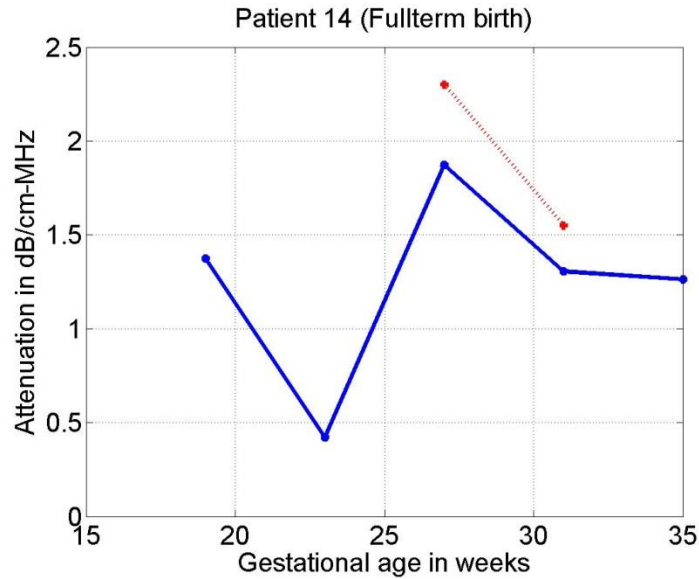


Figure 129: Attenuation vs gestation age for patient 14. Age of the patient is 28. Patient had a history of 2 full term, 1 preterm, and 1 abortion.

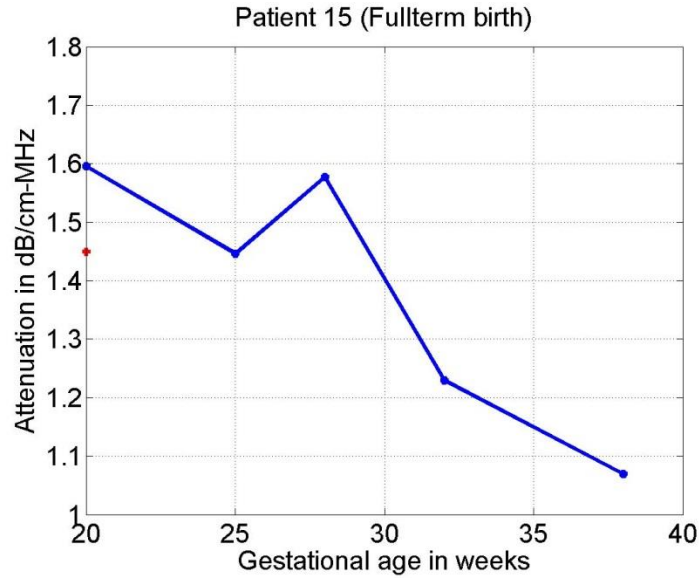


Figure 130: Attenuation vs gestation age for patient 15. Age of the patient is 32. Patient had a history of 4 full term, 0 preterm, 2 abortions.

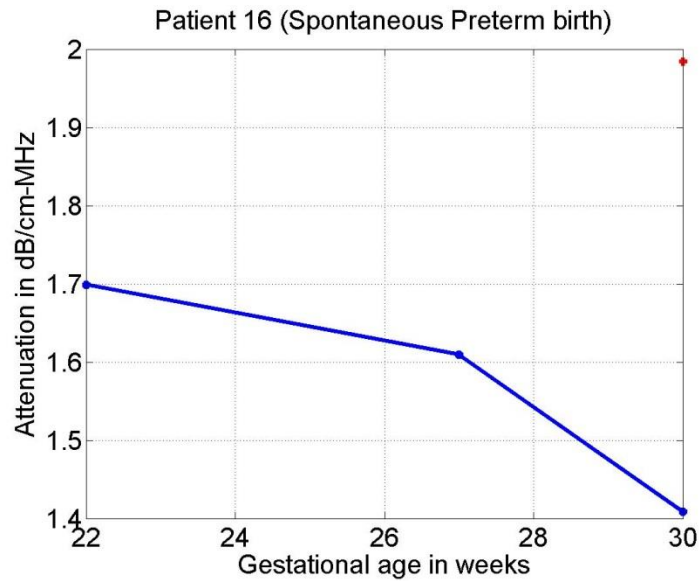


Figure 131: Attenuation vs gestation age for patient 16. Age of the patient is 23. Patient had a history of 0 full term, 1 preterm, and 1 abortion.

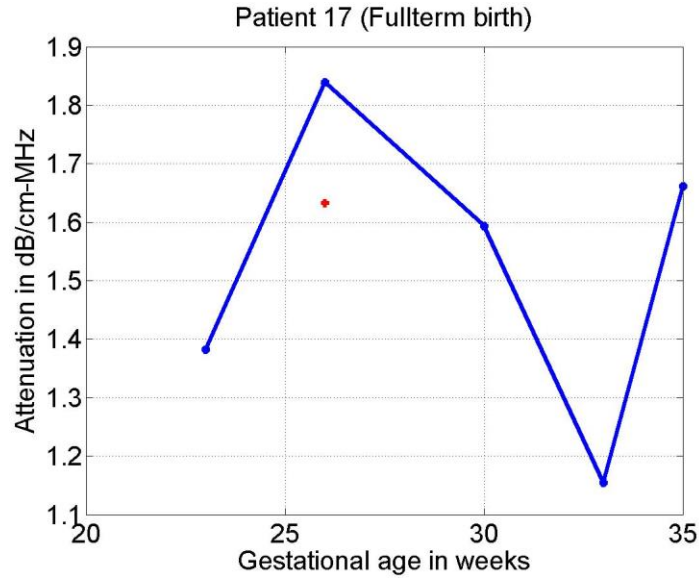


Figure 132: Attenuation vs gestation age for patient 17. Age of the patient is 31. Patient had a history of 0 full term, 1 preterm, and 0 abortion.

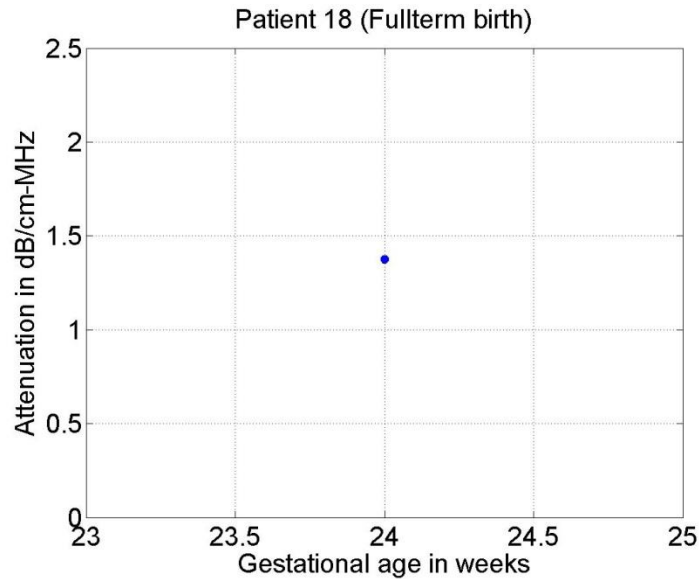


Figure 133: Attenuation vs gestation age for patient 18. Age of the patient is 31. Patient had a history of 2 full term, 1 preterm, 0 abortions.

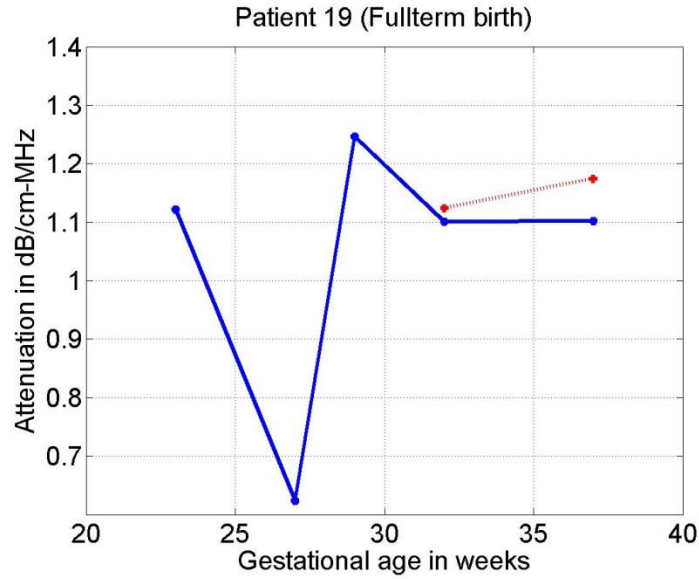


Figure 134: Attenuation vs gestation age for patient 19. Age of the patient is 20. Patient had a history of 1 full term, 1 preterm, and 1 abortion.

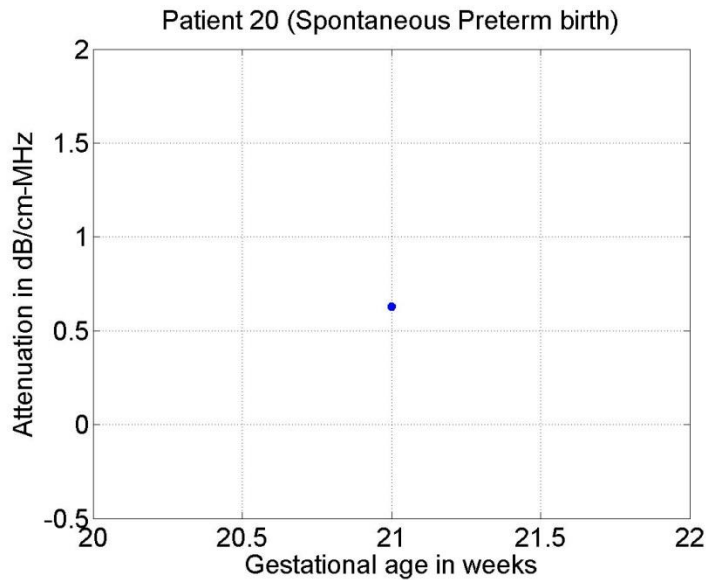


Figure 135: Attenuation vs gestation age for patient 20. Age of the patient is 23. Patient had a history of 0 full term, 0 preterm, and 3 abortions.

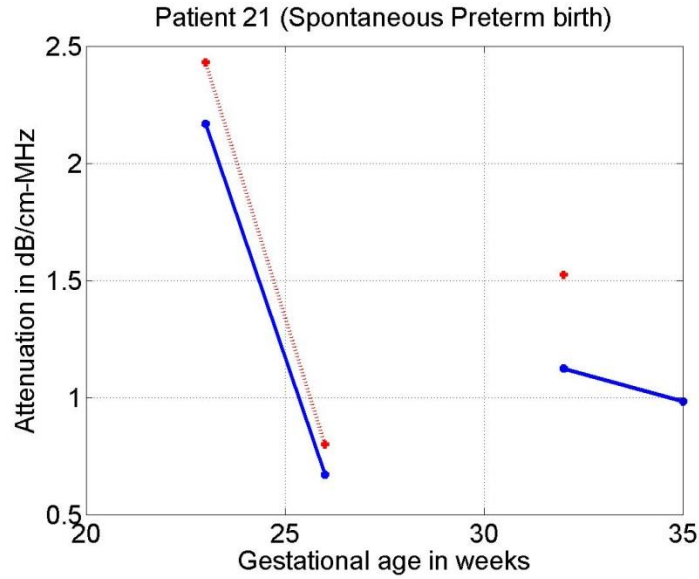


Figure 136: Attenuation vs gestation age for patient 21. Age of the patient is 30. Patient had a history of 2 full term, 2 preterm, 0 abortion.

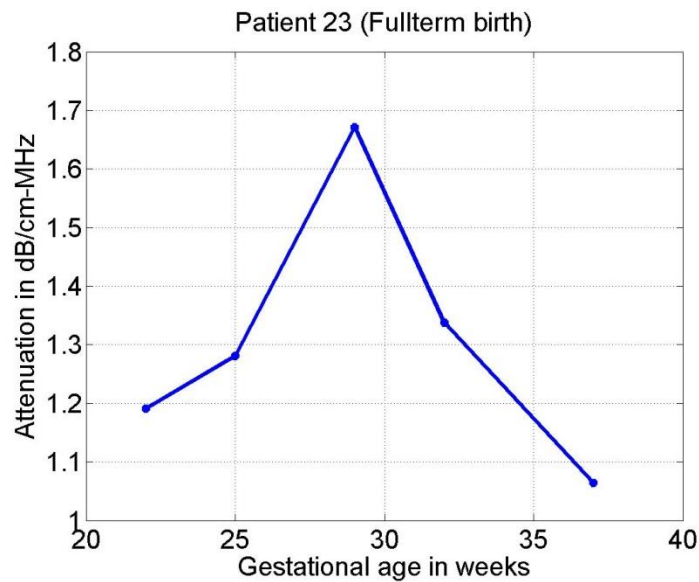


Figure 137: Attenuation vs gestation age for patient 23. Age of the patient is 17. Patient had a history of 0 full term, 0 preterm, 0 abortions.

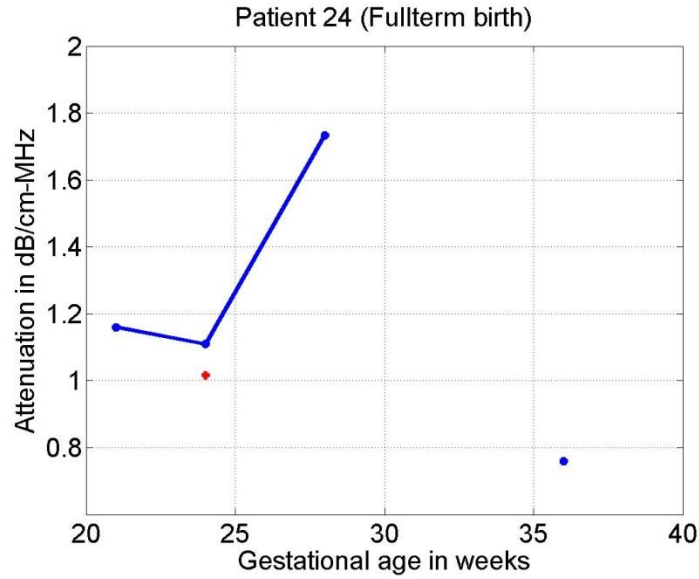


Figure 138: Attenuation vs gestation age for patient 24. Age of the patient is 26. Patient had a history of 1 full term, 2 preterm, 0 abortion.

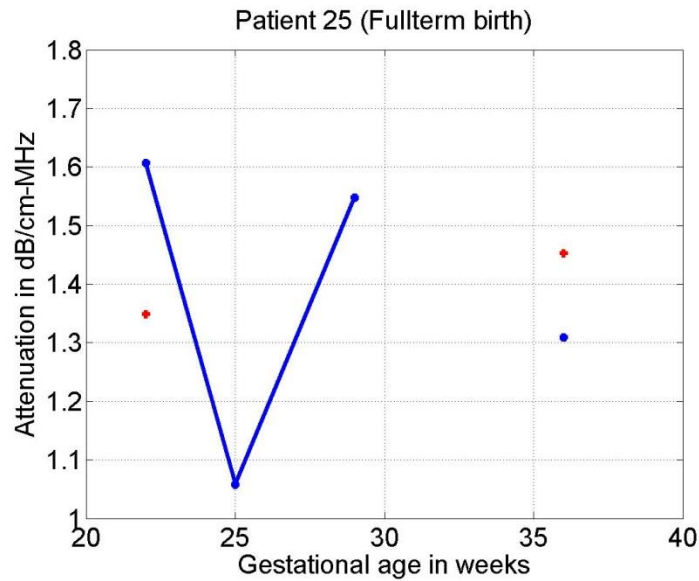


Figure 139: Attenuation vs gestation age for patient 25. Age of the patient is 36. Patient had a history of 0 full term, 0 preterm, and 2 abortions.

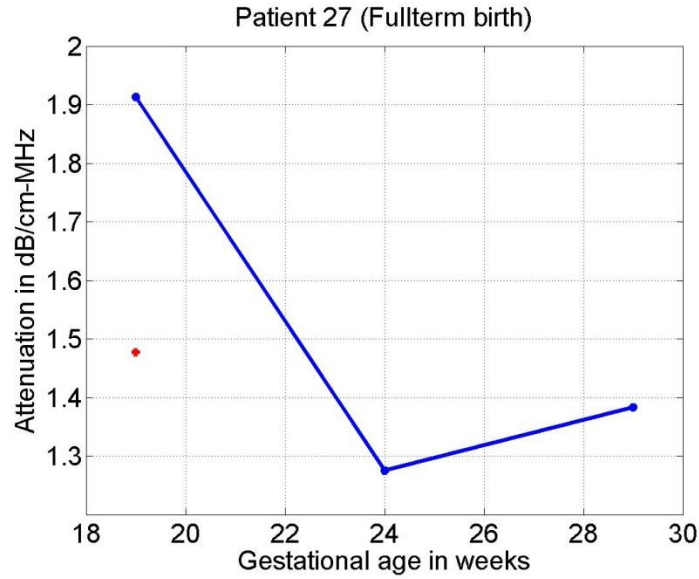


Figure 140: Attenuation vs gestation age for patient 27. Age of the patient is 29. Patient had a history of 0 full term, 2 preterm, 0 abortion.

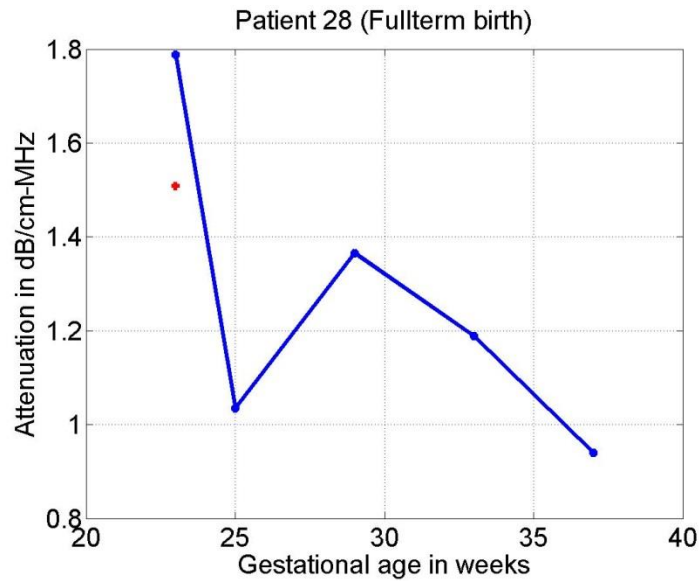


Figure 141: Attenuation vs gestation age for patient 28. Age of the patient is 21. Patient had a history of 1 full term, 0 preterm, and 1 abortion.

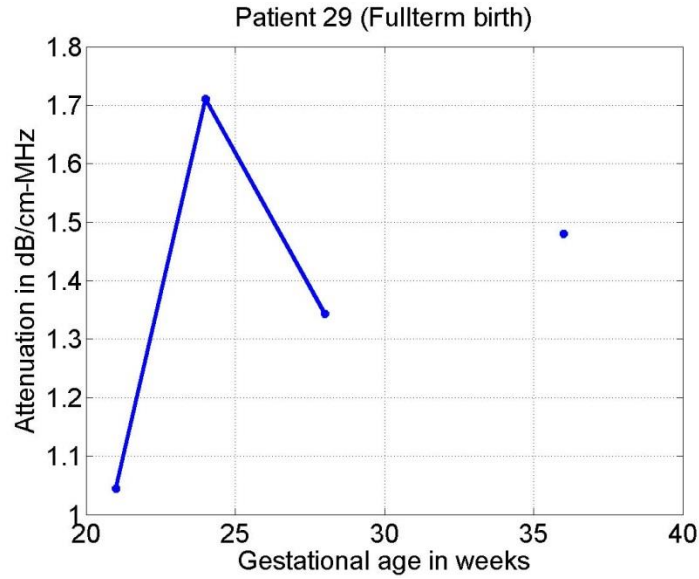


Figure 142: Attenuation vs gestation age for patient 29. Age of the patient is 36. Patient had a history of 0 full term, 0 preterm, and 3 abortions.

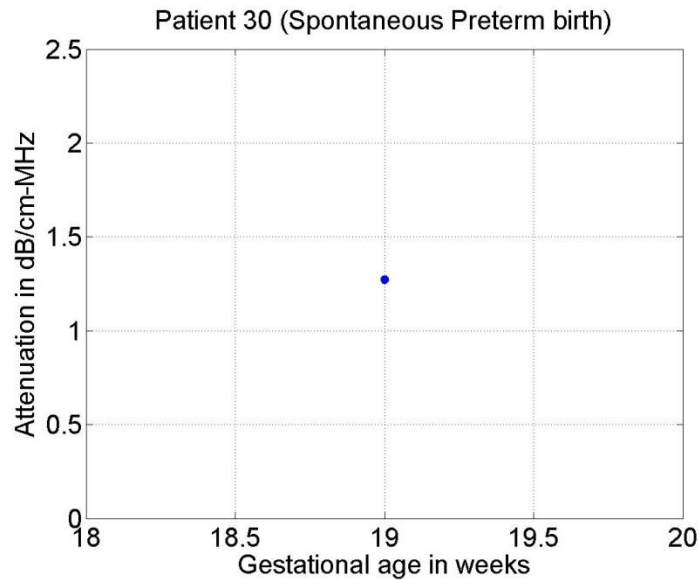


Figure 143: Attenuation vs gestation age for patient 30. Age of the patient is 23. Patient had a history of 0 full term, 0 preterm, and 6 abortions.

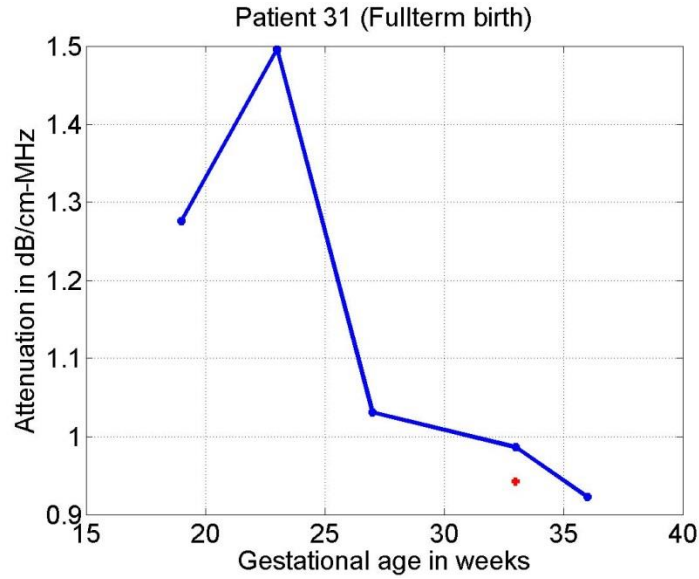


Figure 144: Attenuation vs gestation age for patient 31. Age of the patient is 30. Patient had a history of 0 full term, 0 preterm, and 3 abortions.

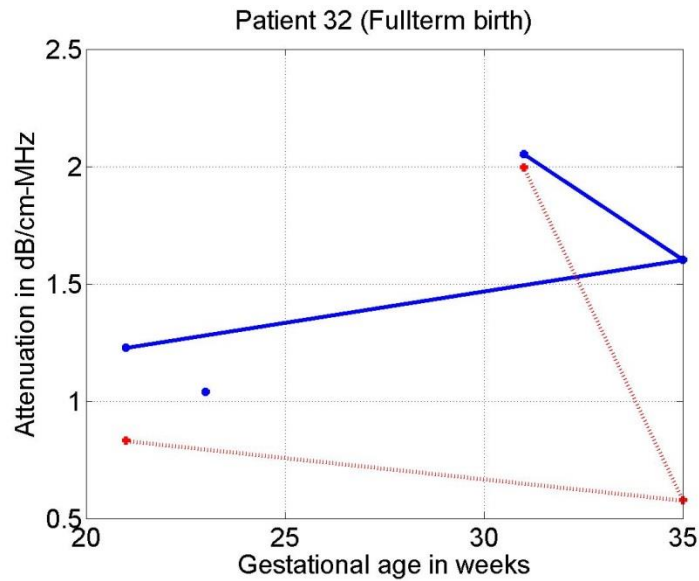


Figure 145: Attenuation vs gestation age for patient 32. Age of the patient is 33. Patient had a history of 2 full term, 0 preterm, and 0 abortion.

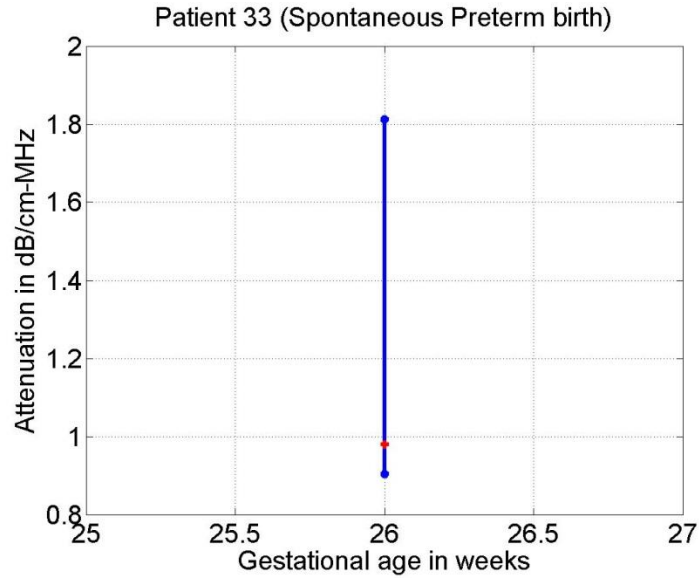


Figure 146: Attenuation vs gestation age for patient 33. Age of the patient is 28. Patient had a history of 1 full term, 4 preterm, 1 abortion.

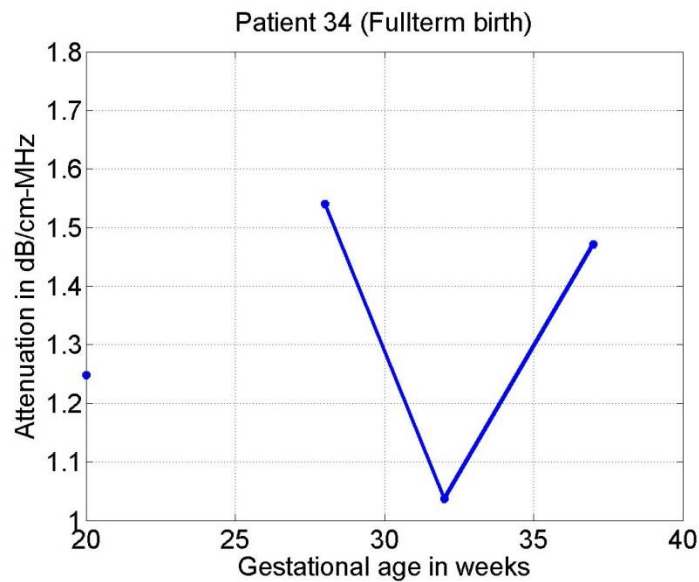


Figure 147: Attenuation vs gestation age for patient 34. Age of the patient is 41. Patient had a history of 0 full term, 0 preterm, and 1 abortion.

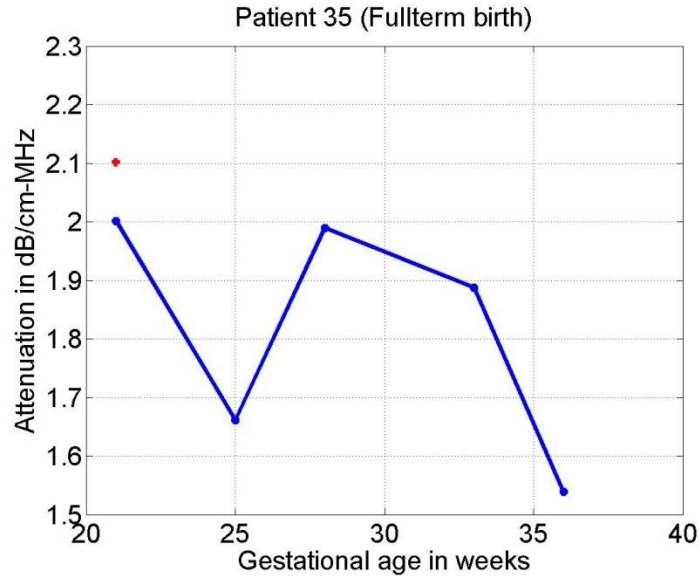


Figure 148: Attenuation vs gestation age for patient 35. Age of the patient is 35. Patient had a history of 6 full term, 0 preterm, and 1 abortion.

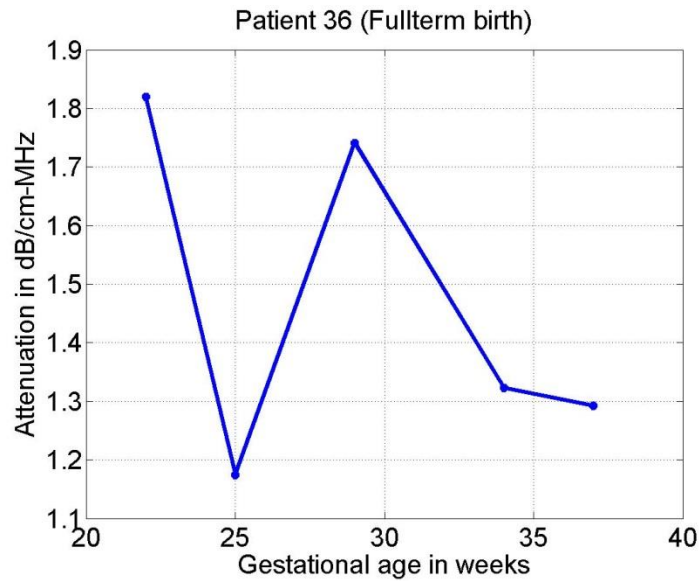


Figure 149: Attenuation vs gestation age for patient 36. Age of the patient is 25. Patient had a history of 0 full term, 0 preterm, and 0 abortion.

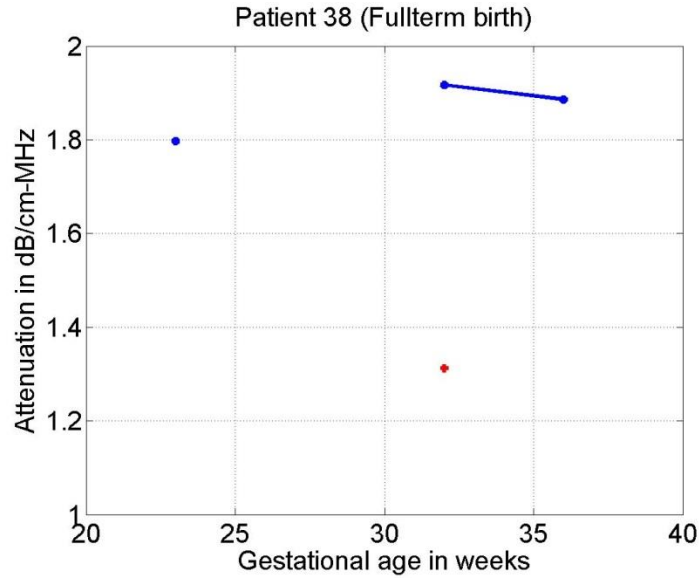


Figure 150: Attenuation vs gestation age for patient 38. Age of the patient is 21. Patient had a history of 0 full term, 1 preterm, 2 abortions.

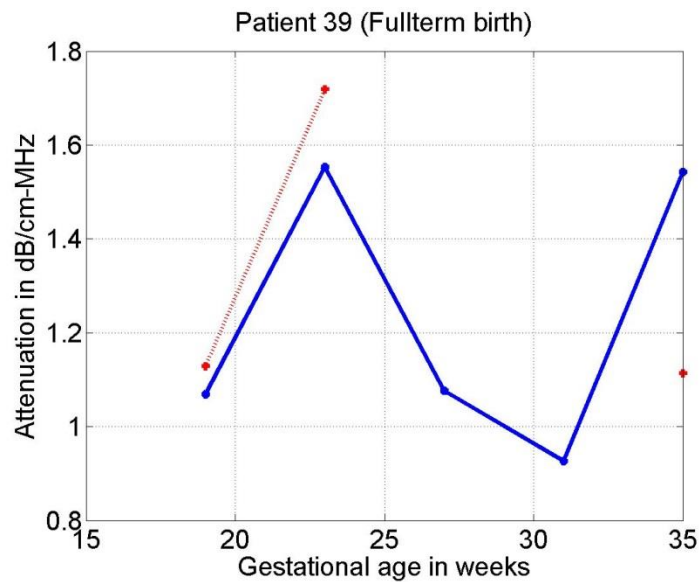


Figure 151: Attenuation vs gestation age for patient 39. Age of the patient is 21. Patient had a history of 0 full term, 0 preterm, and 0 abortion.

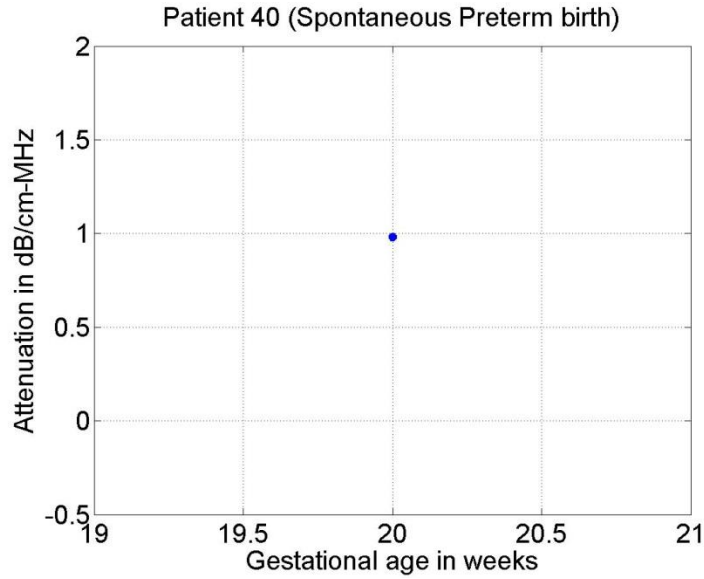


Figure 152: Attenuation vs gestation age for patient 40. Age of the patient is 18. Patient had a history of 0 full term, 1 preterm, 0 abortions.

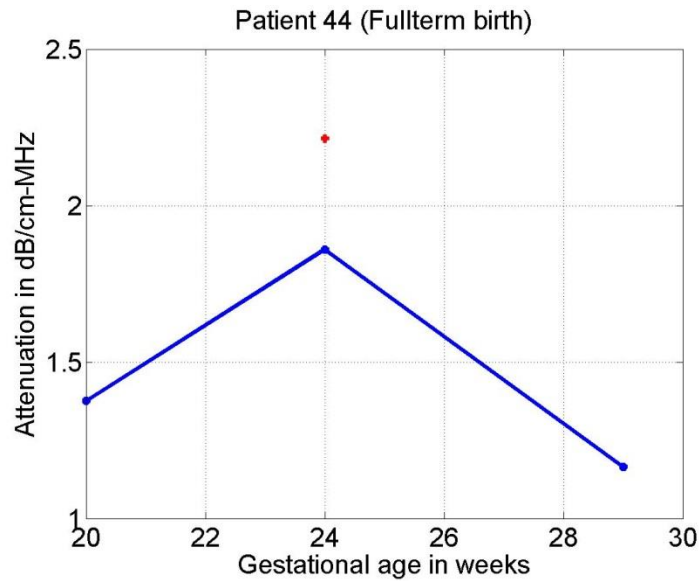


Figure 153: Attenuation vs gestation age for patient 44. Age of the patient is 33. Patient had a history of 1 full term, 0 preterm, and 0 abortion.

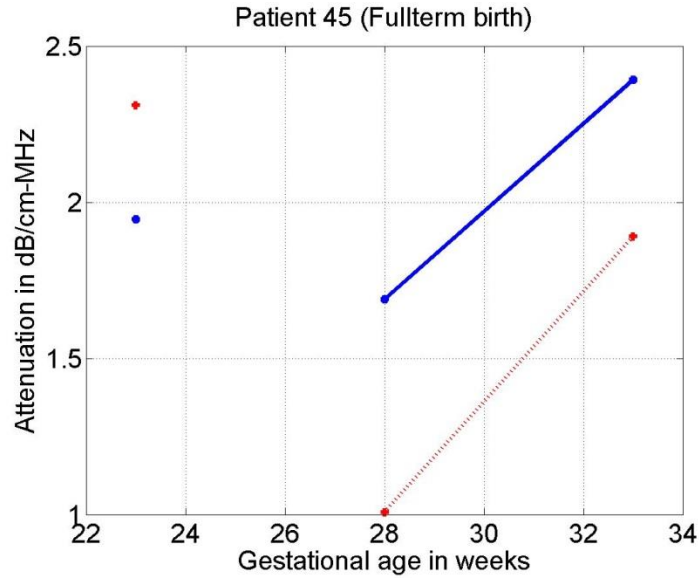


Figure 154: Attenuation vs gestation age for patient 45. Age of the patient is 29. Patient had a history of 0 full term, 1 preterm, 2 abortions.

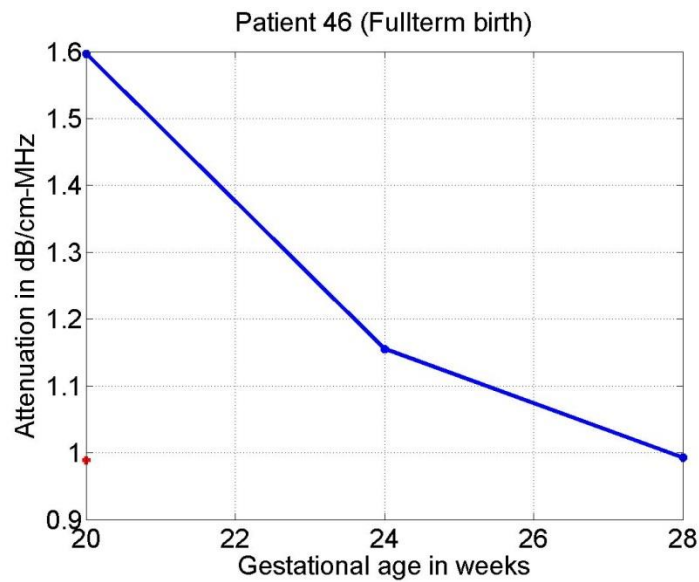


Figure 155: Attenuation vs gestation age for patient 46. Age of the patient is 33. Patient had a history of 4 full term, 0 preterm, 5 abortions.

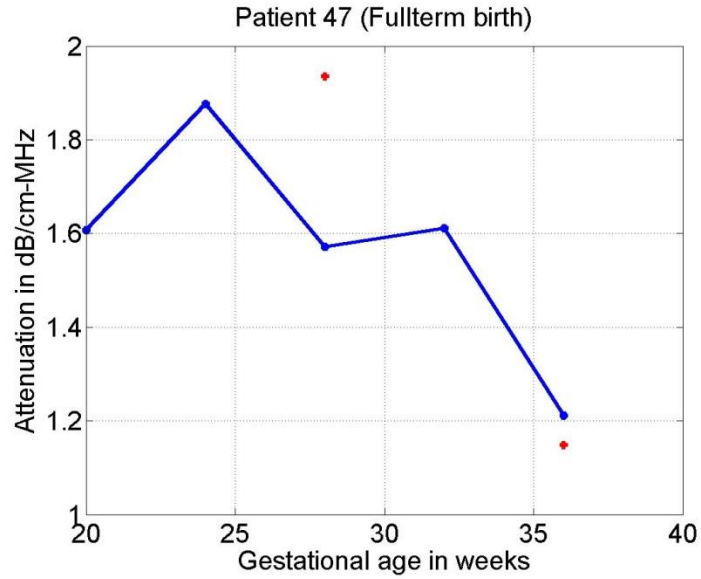


Figure 156: Attenuation vs gestation age for patient 47. Age of the patient is 26. Patient had a history of 0 full term, 0 preterm, and 0 abortion.

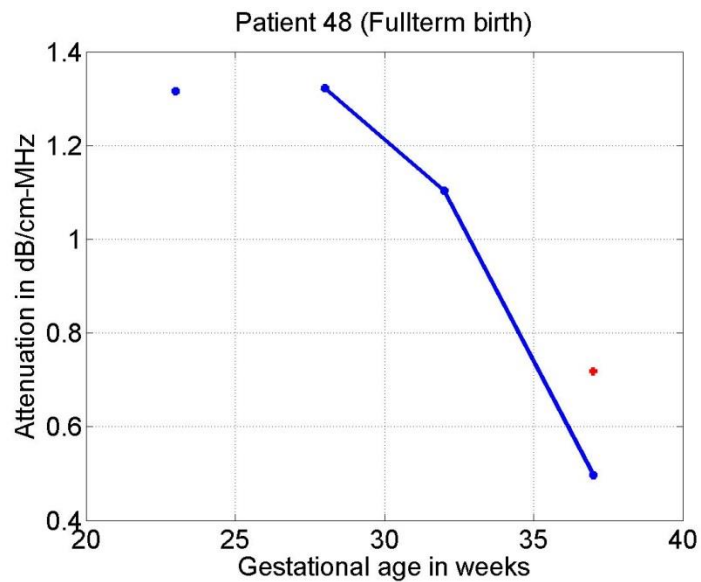


Figure 157: Attenuation vs gestation age for patient 48. Age of the patient is 18. Patient had a history of 0 full term, 0 preterm, and 0 abortion.

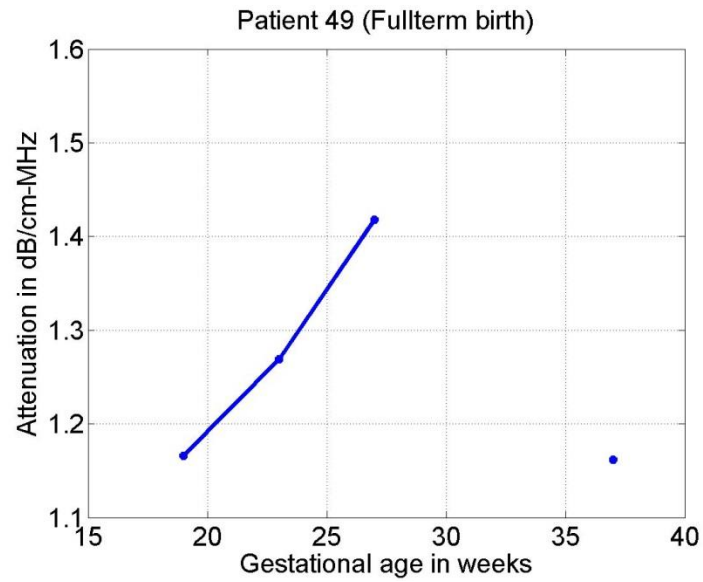


Figure 158: Attenuation vs gestation age for patient 49. Age of the patient is 24. Patient had a history of 0 full term, 1 preterm, and 0 abortion.

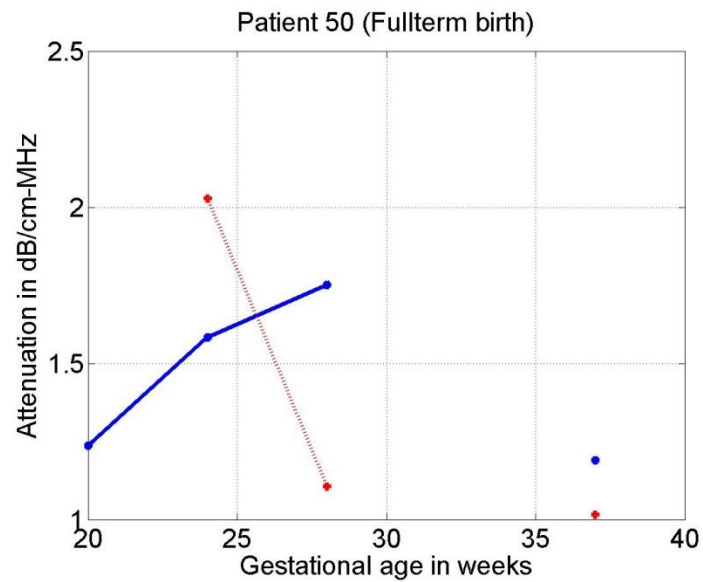


Figure 159: Attenuation vs gestation age for patient 50. Age of the patient is 28. Patient had a history of 2 full term, 1 preterm, and 1 abortion.

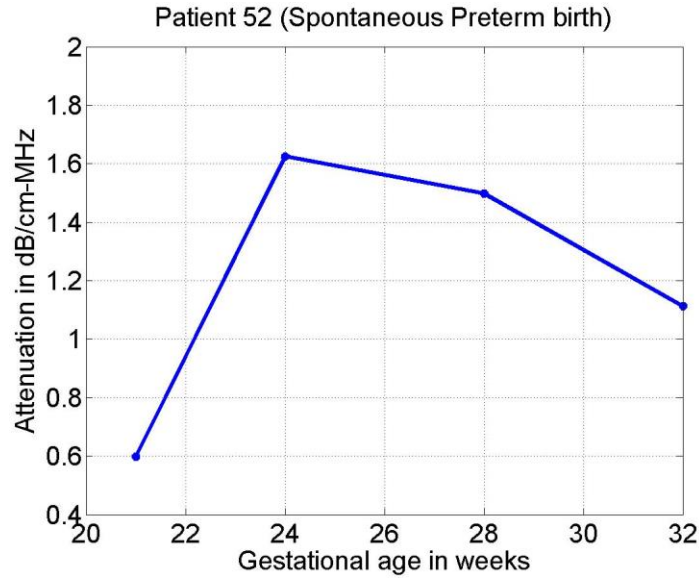


Figure 160: Attenuation vs gestation age for patient 52. Age of the patient is 34. Patient had a history of 1 full term, 0 preterm, 2 abortions.

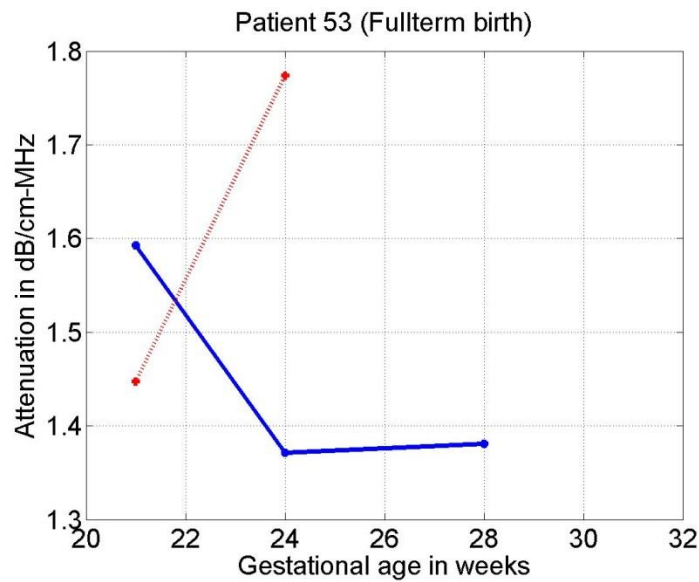


Figure 161: Attenuation vs gestation age for patient 53. Age of the patient is 28. Patient had a history of 1 full term, 0 preterm, and 0 abortion.

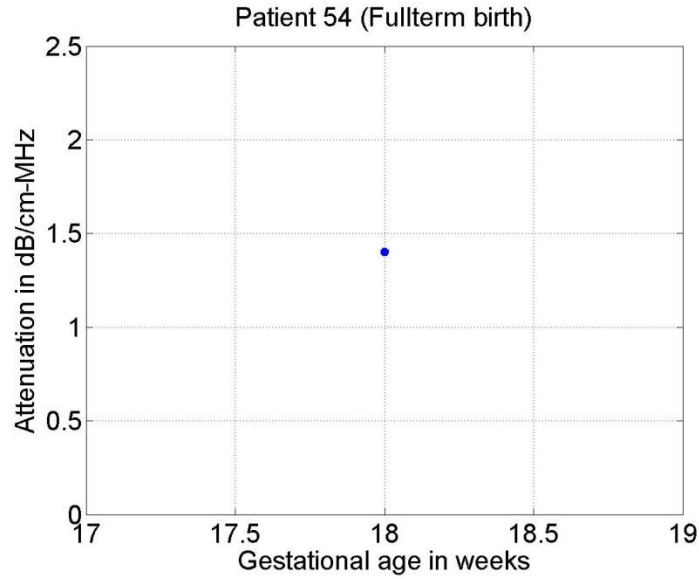


Figure 162: Attenuation vs gestation age for patient 54. Age of the patient is 25. Patient had a history of 0 full term, 2 preterm, 0 abortion.

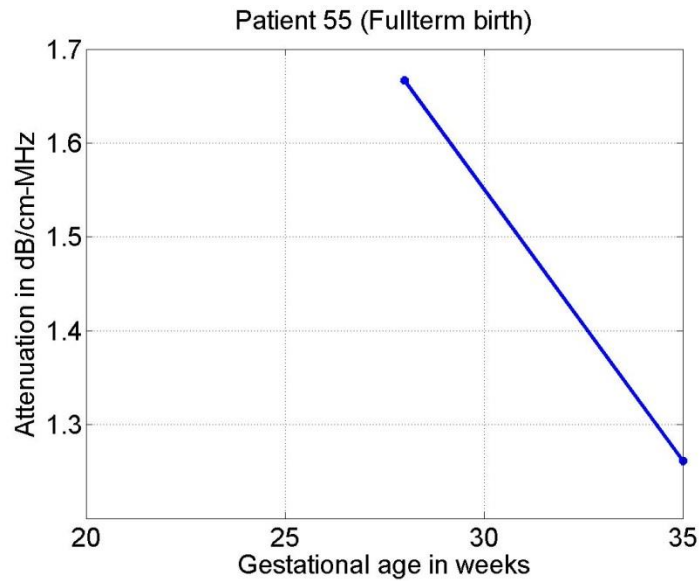


Figure 163: Attenuation vs gestation age for patient 55. Age of the patient is 21. Patient had a history of 0 full term, 0 preterm, 0 abortions.

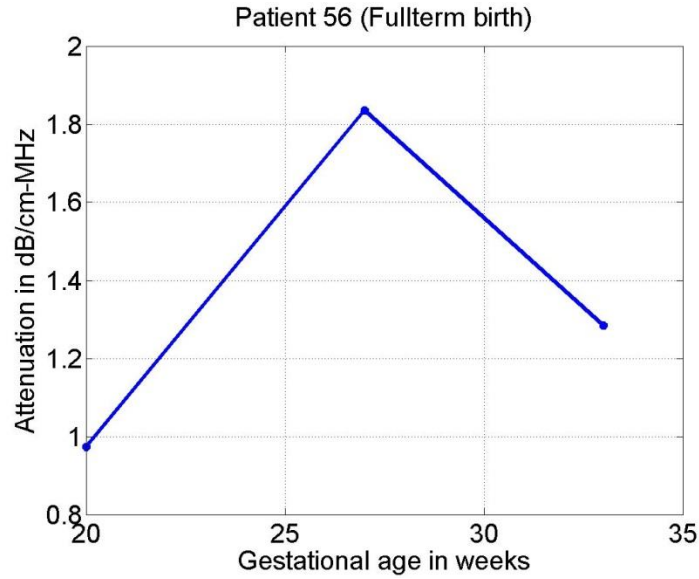


Figure 164: Attenuation vs gestation age for patient 56. Age of the patient is 35. Patient had a history of 5 full term, 0 preterm, and 1 abortion.

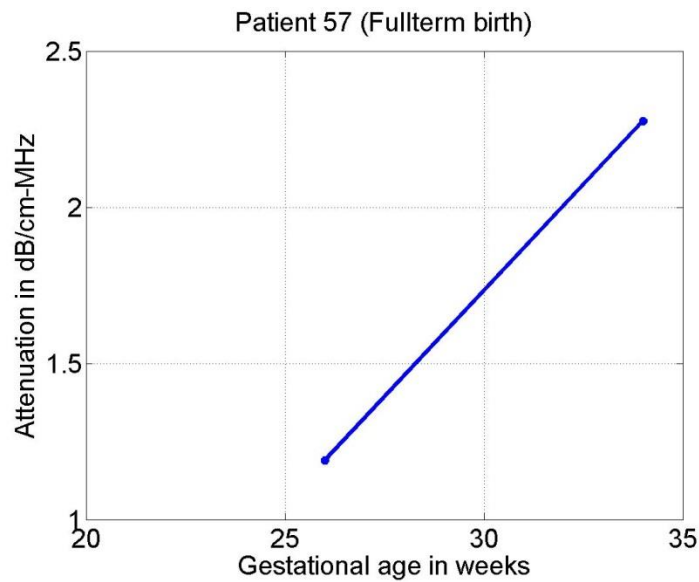


Figure 165: Attenuation vs gestation age for patient 57. Age of the patient is 21. Patient had a history of 1 full term, 0 preterm, and 0 abortion.

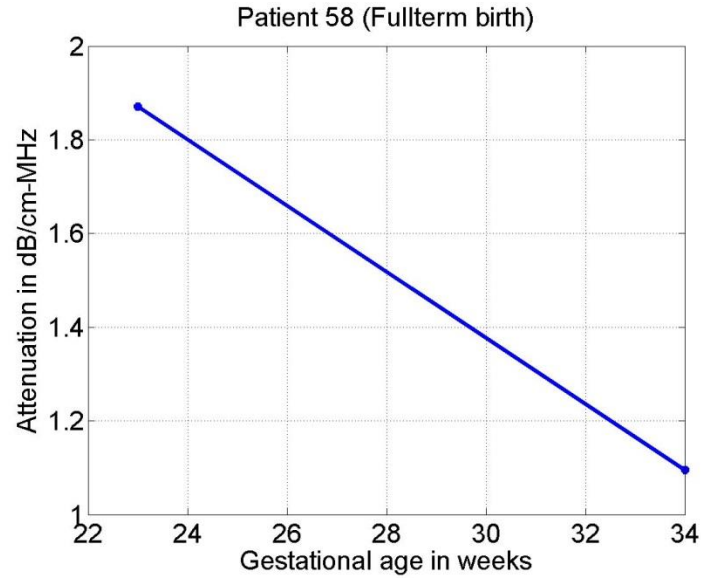


Figure 166: Attenuation vs gestation age for patient 58. Age of the patient is 23. Patient had a history of 1 full term, 0 preterm, and 1 abortion.

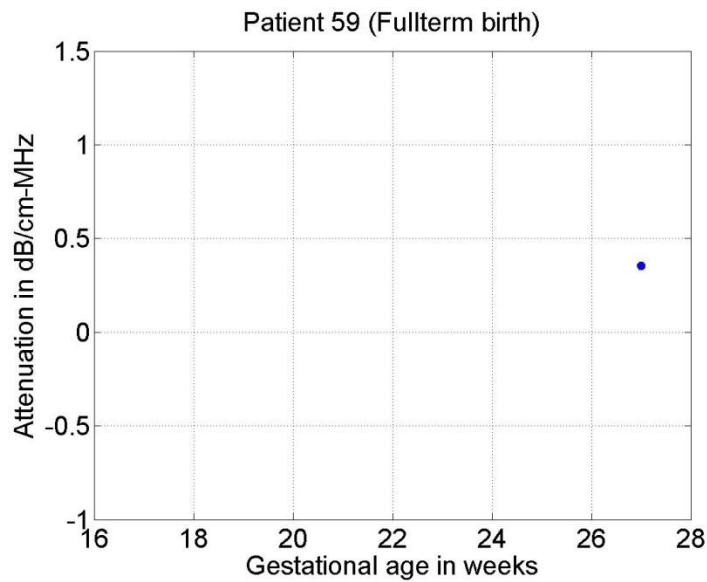


Figure 167: Attenuation vs gestation age for patient 59. Age of the patient is 20. Patient had a history of 0 full term, 0 preterm, and 0 abortion.

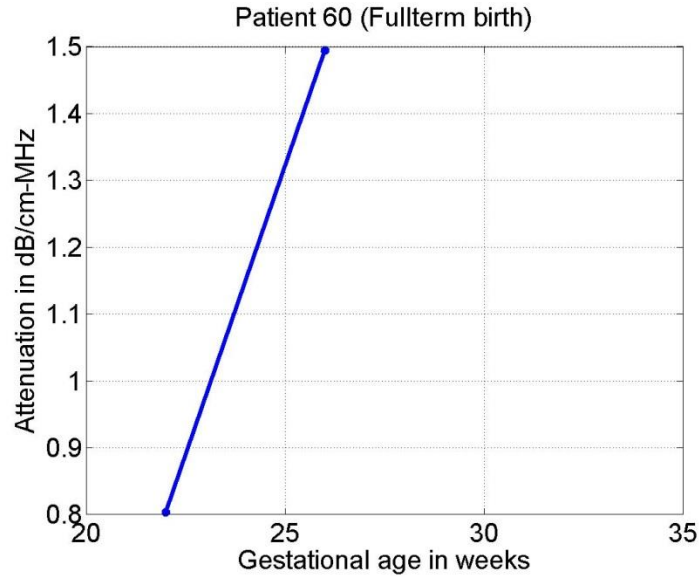


Figure 168: Attenuation vs gestation age for patient 60. Age of the patient is 22. Patient had a history of 1 full term, 0 preterm, 2 abortions.

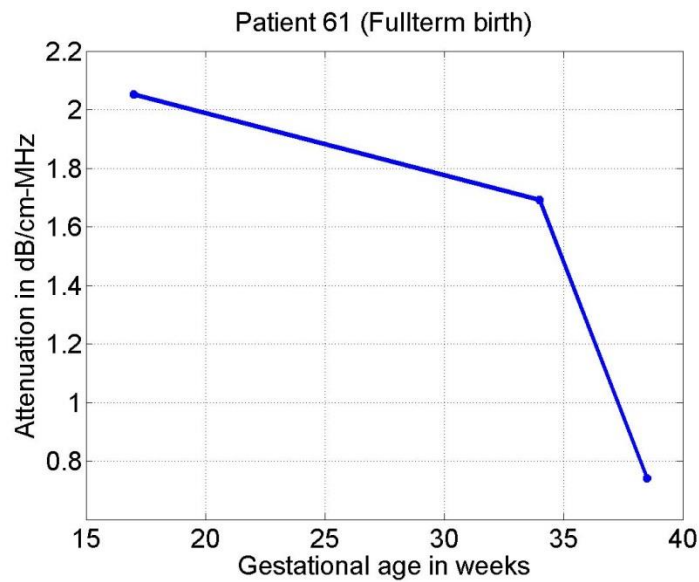


Figure 169: Attenuation vs gestation age for patient 61. Age of the patient is 20. Patient had a history of 0 full term, 0 preterm, and 0 abortion.

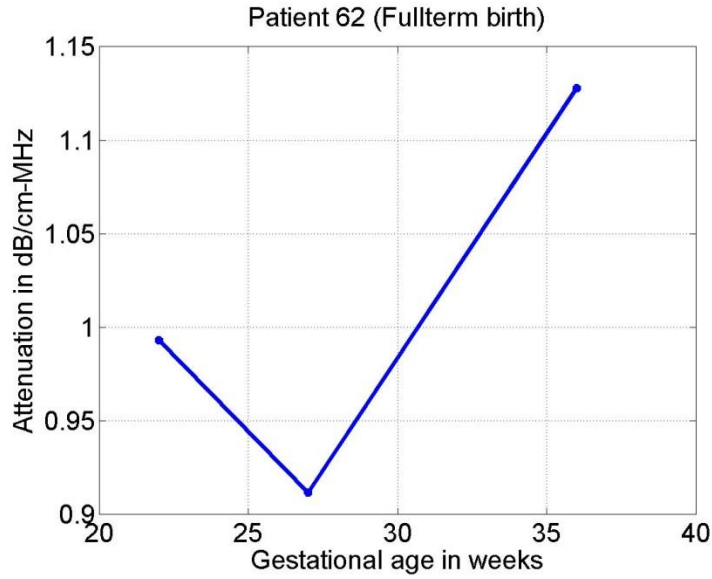


Figure 170: Attenuation vs gestation age for patient 62. Age of the patient is 28. Patient had a history of 2 full term, 0 preterm, and 0 abortion.

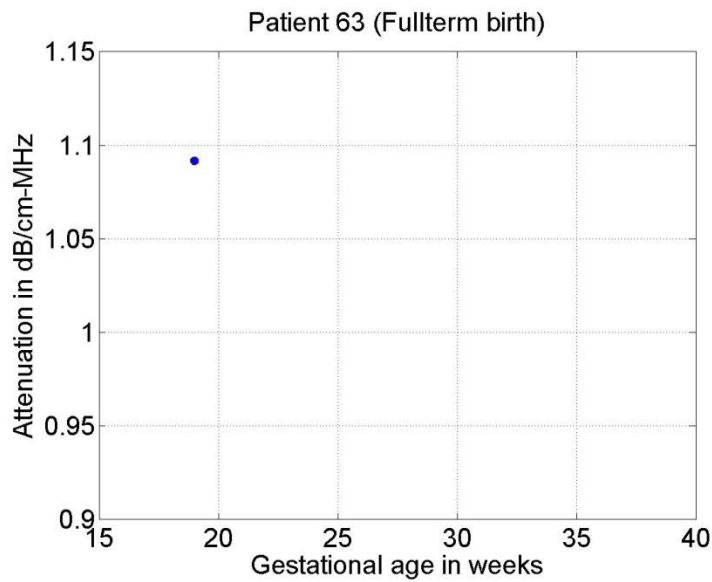


Figure 171: Attenuation vs gestation age for patient 63. Age of the patient is 21. Patient had a history of 1 full term, 0 preterm, and 1 abortion.

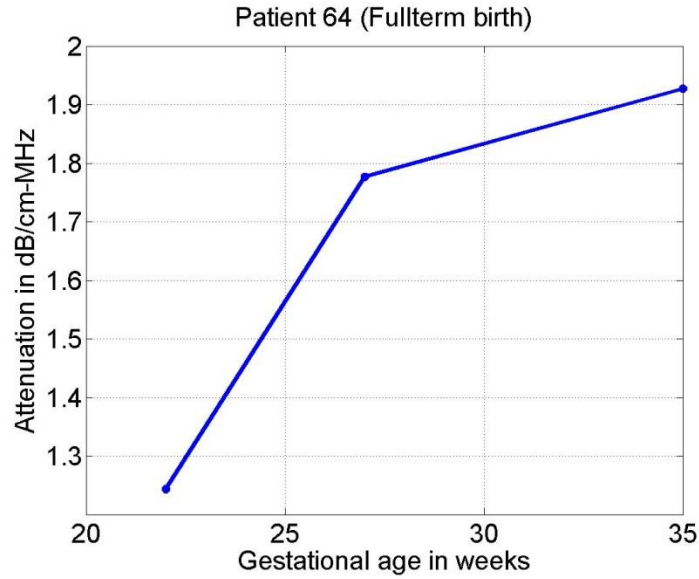


Figure 172: Attenuation vs gestation age for patient 64. Age of the patient is 28. Patient had a history of 0 full term, 0 preterm, and 0 abortion.

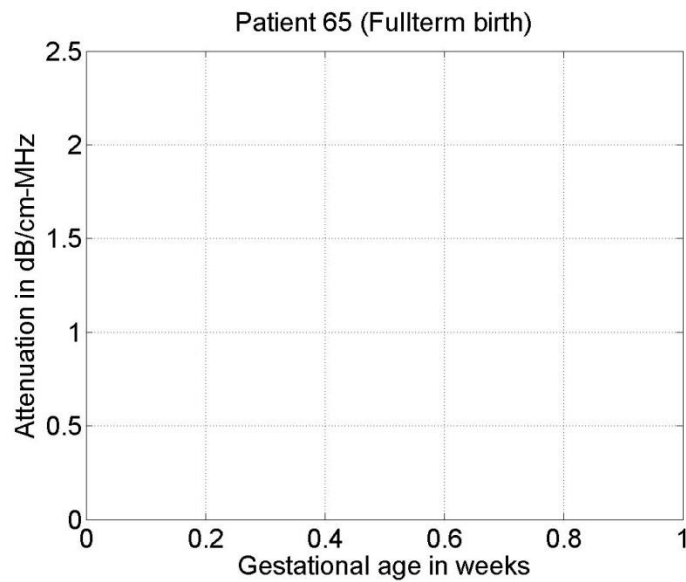


Figure 173: Attenuation vs gestation age for patient 65. Age of the patient is 19. Patient had a history of 0 full term, 0 preterm, and 1 abortion.

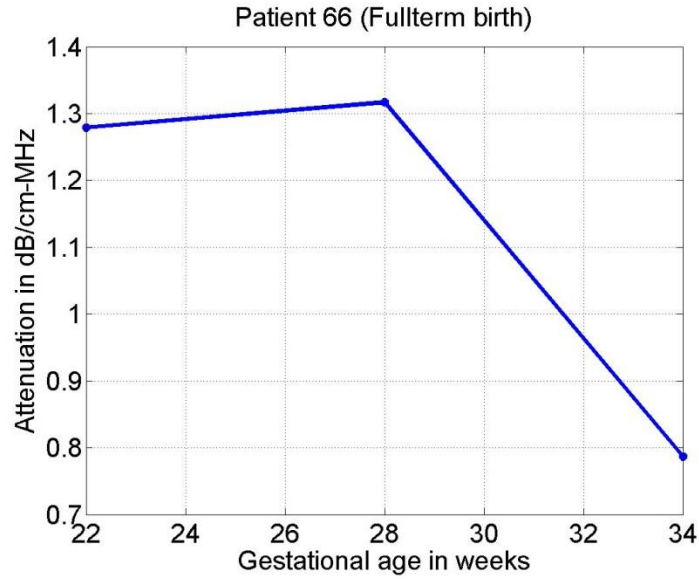


Figure 174: Attenuation vs gestation age for patient 66. Age of the patient is 18. Patient had a history of 0 full term, 0 preterm, and 0 abortion.

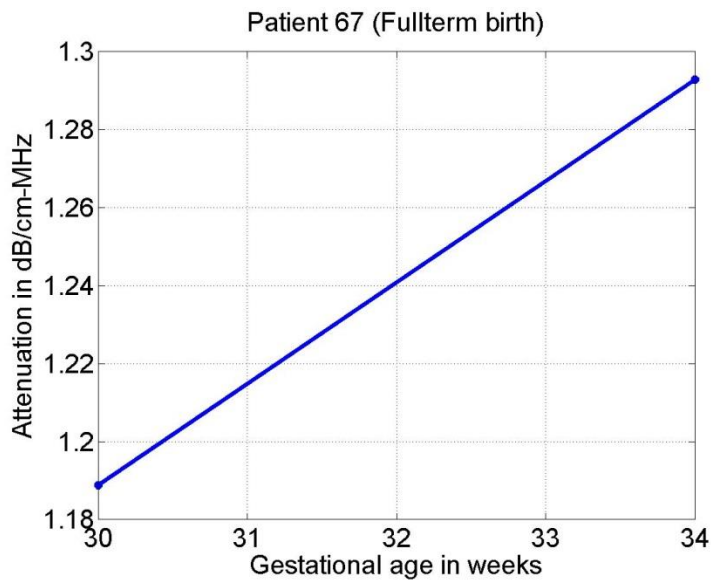


Figure 175: Attenuation vs gestation age for patient 67. Age of the patient is 18. Patient had a history of 0 full term, 0 preterm, and 0 abortion.

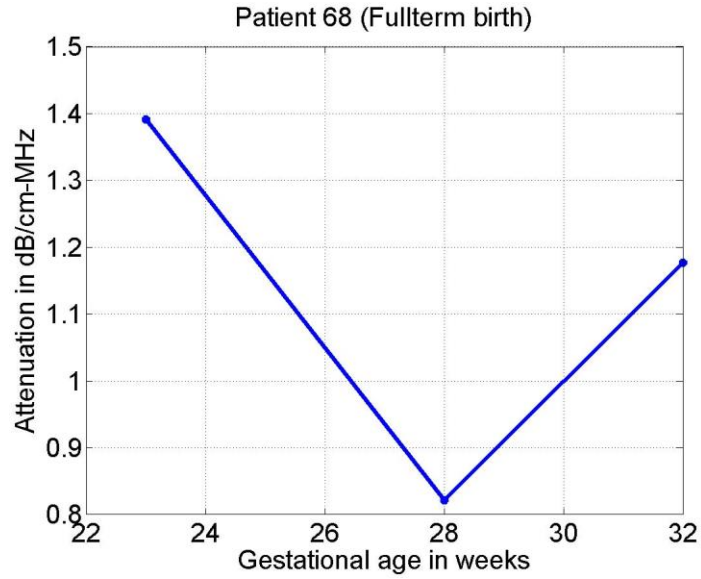


Figure 176: Attenuation vs gestation age for patient 68. Age of the patient is 24. Patient had a history of 0 full term, 0 preterm, and 0 abortion.

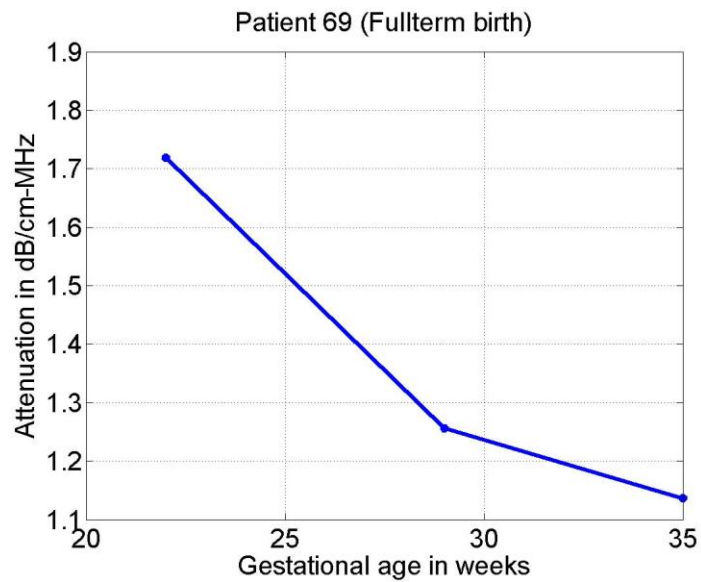


Figure 177: Attenuation vs gestation age for patient 69. Age of the patient is 28. Patient had a history of 1 full term, 0 preterm, and 0 abortion.

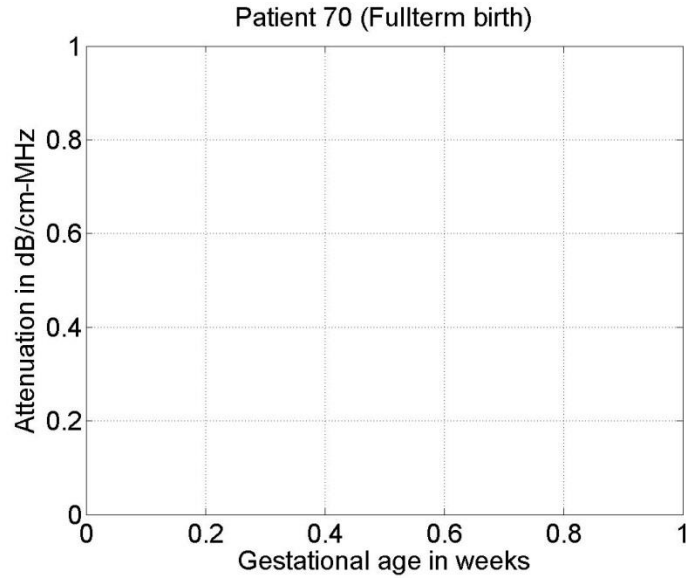


Figure 178: Attenuation vs gestation age for patient 70. Age of the patient is 31. Patient had a history of 2 full term, 0 preterm, 2 abortions.

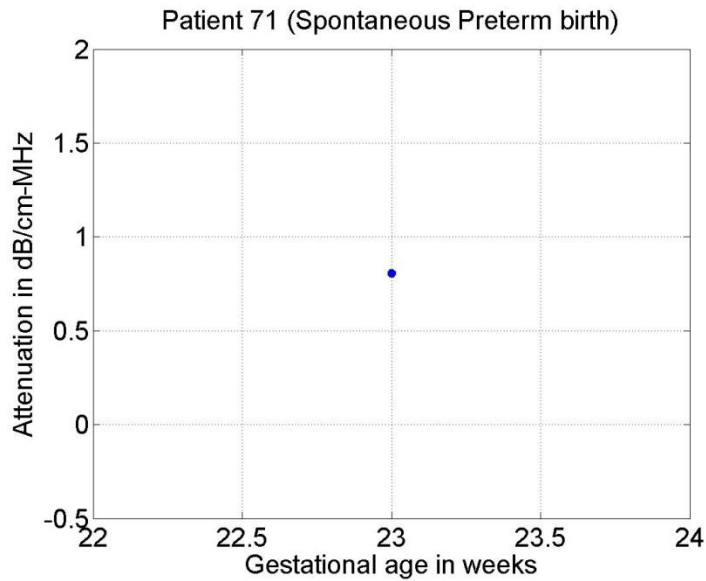


Figure 179: Attenuation vs gestation age for patient 71. Age of the patient is 23. Patient had a history of 2 full term, 0 preterm, and 0 abortion.

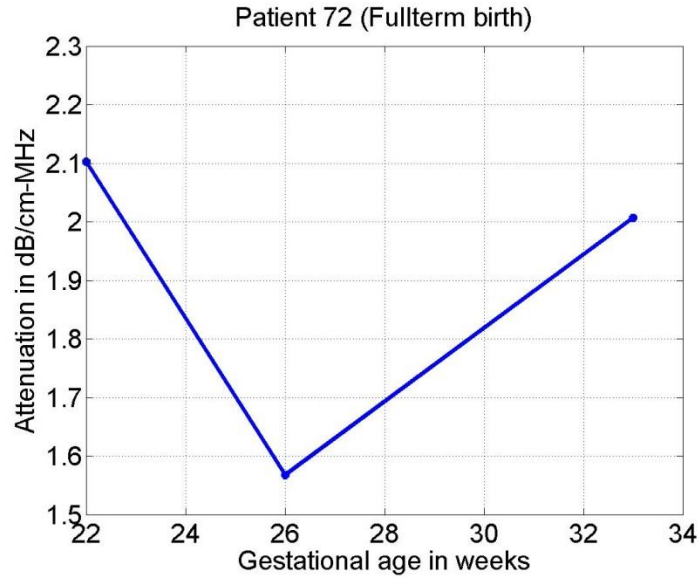


Figure 180: Attenuation vs gestation age for patient 72. Age of the patient is 19. Patient had a history of 0 full term, 0 preterm, and 0 abortion.

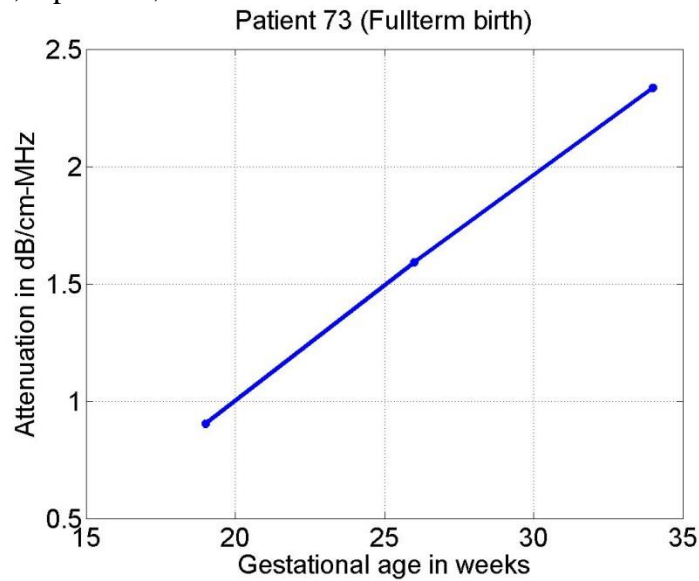


Figure 181: Attenuation vs gestation age for patient 73. Age of the patient is 18. Patient had a history of 0 full term, 0 preterm, and 0 abortion.

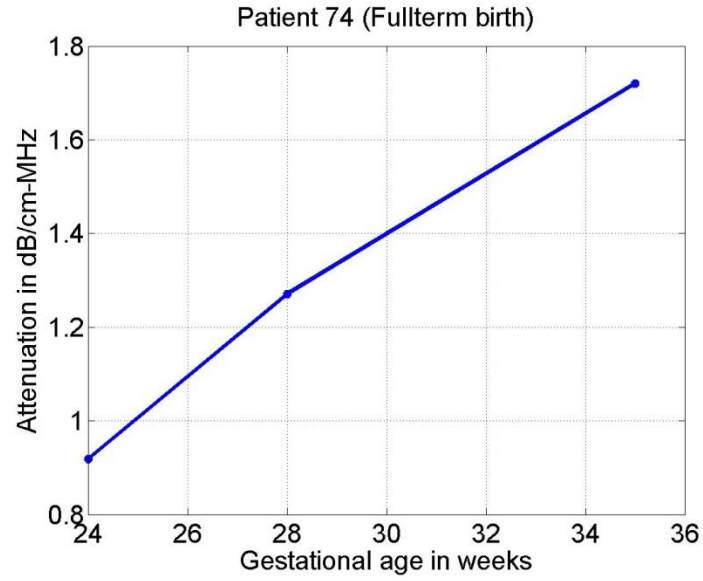


Figure 182: Attenuation vs gestation age for patient 74. Age of the patient is 19. Patient had a history of 1 full term, 0 preterm, and 0 abortion.